VYSOKÉ UČENÍ TECHNICKÉ V BRNĚ

BRNO UNIVERSITY OF TECHNOLOGY

FAKULTA STROJNÍHO INŽENÝRSTVÍ

FACULTY OF MECHANICAL ENGINEERING

ÚSTAV FYZIKÁLNÍHO INŽENÝRSTVÍ

INSTITUTE OF PHYSICAL ENGINEERING

NÁVRH A VÝVOJ UNIKÁTNÍCH ZAŘÍZENÍ PRO RŮST NANOSTRUKTURNÍCH MATERIÁLŮ V PODMÍNKÁCH VAKUA

DESIGN AND DEVELOPMENT OF UNIQUE EQUIPMENTS FOR THE GROWTH OF NANOSTRUCTURAL MATERIALS IN VACUUM CONDITIONS

HABILITAČNÍ PRÁCE

HABILITATION THESIS

AUTOR PRÁCE

AUTHOR

Ing. Jindřich Mach, Ph.D.

Brno 2021

Klíčová slova:

Atomární zdroj, iontově-atomární zdroj, iontový zdroj, depozice, ultratenké vrstvy, nanostruktury, epitaxe, CVD, MBE, vakuum, UHV.

Keywords:

Atomic source, ion-atomic source, ion source, deposition, ultrathin layers, nanostructures, epitaxy, CVD, MBE, vacuum, UHV.

ČESTNÉ PROHLÁŠENÍ

Prohlašuji, že předložená habilitační práce je původní a zpracoval jsem ji samostatně. Prohlašuji, že citace použitých pramenů je úplná a že jsem ve své práci neporušil autorská práva (ve smyslu zákona č. 121/2000 Sb., o právu autorském a o právech souvisejících s právem autorským).

V Brně dne 21.8. 2021

Ing. Jindřich Mach, Ph.D.

Autor práce

Poděkování

Tímto bych chtěl poděkovat všem kolegům a zejména prof. RNDr. Tomášovi Šikolovi CSc. za dlouhodobou profesní podporu. Také velké poděkovaní patří doc. Ing. Miroslavu Bartošíkovi Ph.D., za celou řadu podnětných připomínek a hodin strávených v rámci odborných diskusí. V neposlední řadě bych rád poděkoval rodičům za celoživotní podporu při studiu a děkuji manželce Anně za podporu a její velkorysou toleranci, která byla pro vypracování předložené habilitační práce tak nezbytná.

Obsah

1. Úvod 6

2. Chemická depozice z plynné fáze (CVD) 7

2.1 Aplikace navrženého a realizovaného CVD reaktoru – příprava grafenu metodou CVD 9

2.1.1 Článek č. 1 - Ultra-hladká kovová folie pro růst vysoce kvalitního grafenu metodou depozice s plynné fáze 12

2.1.2 Článek č. 2 - Mechanismus vzniku a potlačení hystereze v grafenovém FET senzoru způsobené fyzisorbovanou vodou 21

3. Depozice z pevné fáze 31

4. Zdroje atomů a molekul o termální energii 32

4.1 Nízkoteplotní zdroje atomů (do 400 °C) 36

4.2 Teplotní zdroje atomů (do 1 000 °C) 38

4.2.1 Aplikace – depozice atomů Ga na grafen 40

4.2.2 Článek č. 3 – Elektrické transportní vlastnosti grafenu dopovaného galiem 41

4.3 Vysokoteplotní zdroje atomů žáruvzdorných materiálů (do 2 500 °C) 52

4.3.1 Speciální zdroje atomů 54

5. Iontově-atomární svazkové zdroje 58

5.1.1 Článek č. 4 – Iontově-atomární svazkový zdroj s ultranízkou energií (30-200 eV) iontů pro depozici za asistence iontových svazků v ultravysokém vakuu 61

5.1.2 Článek č. 5 – Optimalizace iontově-atomárního zdroje pro depozici GaN ultratenkých vrstev…… 69

5.1.3 Článek č. 6 – Nízkoteplotní selektivní růst krystalů GaN na předem vzorovaný Si substrát …… 76

6. Iontové zdroje 84

7. Závěr 87

1. Úvod

V současné době je nanostrukturním materiálům věnována značná pozornost, protože se projevuje stále více jejich význam v různých oborech lidské činnosti. Nezastupitelné uplatnění nalézají tyto materiály například v polovodičovém průmyslu, strojírenském průmyslu, medicíně,a také i v environmetálních oborech. Předpona „nano“ je odvozena z řeckého slova „nanos“, což znamená „trpaslík“. Spojením slova „nano“ s jednotkou „metr“ přináší termín „nanometr“, který označuje jednotku měření délky 1×10^{-9} m.

Nanomateriály získávají nové unikátní vlastnosti právě díky limitnímu omezení jejich rozměrů a to jak v jednom rozměru (2D materiály), tak ve dvou (1D materiály), případně ve třech rozměrech (0D). Například vlivem omezení rozměrů lze docílit změny hustoty elektronových stavů $D(E)$ v materiálu. Mezi hlavního reprezentanta 2D materiálů lze uvést jednu monovrstvu atomů uhlíku, tzv. grafen [1], který rozpoutal intenzivní zájem o studium těchto typů materiálů. Za 1D materiály jsou též označovány nanodráty. Jejich průměry jsou zpravidla od 3 až do 100 nanometrů a jsou obvykle více než 1000 krát delší, než je jejich průměr. Tyto nanodráty jsou vyráběny z různých vodivých, polovodičových a izolujících materiálů nebo mohou být skládány z organických molekulárních jednotek, kdy hovoříme o molekulárních nanodrátech (například DNA). Vlivem omezených rozměrů se u nich projevují kvantově mechanické efekty. Dalším snižováním dimenze materiálu se dostaneme až k takzvaným nanotečkám (0D). Nanotečky jsou definovány jako malé částice o velikosti v rozsahu 1 až 100 nm chovající se jako jedna částice s ohledem na elektronovou strukturu. Zde se hustota elektronových stavů stává množinou delta funkcí a tyto struktury se chovají v podstatě jako umělé atomy. Uvedené kvantové tečky nalézají potenciální aplikace při výrobě jedno-elektronových tranzistorů [2], solárních článků, LED diod, laserů a využívají se při výzkumu biologie buněk [3].

Růst tenkých a ultratenkých vrstev a nanostruktur lze realizovat pomocí metod založených na chemických nebo fyzikálních principech. Mezi chemické depoziční metody se řadí metoda depozice z plynné fáze (CVD – *Chemical Vapour Deposition*), kdy k růstu ultratenkých, tenkých vrstev a nanostruktur dochází při chemické reakci na povrchu substrátu. Jako fyzikální lze označit metody depozice růstu ultratenkých vrstev a nanostruktur využívající elektrické, termodynamické nebo i jiné mechanismy. Často jsou využívány k formování svazků atomy či molekuly z nasycených par deponovaných materiálů, proto se fyzikální metody nazývají depozicí z plynné fáze (PVD – *Physical Vapour Deposition*).

Tato práce se zabývá konstrukcí a aplikací zařízení užívaných při tvorbě nanostrukturních materiálů v podmínkách vakua. Materiály připravené pomocí těchto nově vyvinutých zkonstruovaných moderních zařízení jsou perspektivními kandidáty pro výrobu a vylepšení například citlivých senzorů [4], elektronických obvodů [5], solárních článků [6] a baterií určených pro skladování energie [7, 8]. Všechna v této práci uváděná vyvinutá a zkonstruovaná zařízení pro depozici nanostrukturních materiálů jsou aktivně užívána studenty během výuky a při realizaci jejich závěrečných prací. Uvedená unikátní zařízení jsou rovněž intenzivně využívána k vědeckým účelům, což je dokumentováno přiloženými vědeckými články, které obsahují výsledky VaV, získané jejich pomocí.

2. Chemická depozice z plynné fáze (CVD)

CVD depozice je v současné době hojně využívaná zejména v polovodičovém průmyslu, například pro růst složitých multivrstevnatých struktur sloužících k přípravě polovodičových mikro-elektronických součástek jakými jsou například diody, transistory, senzory, mikroprocesory, solární články a další [9]. Při této metodě růstu se užívají nízké tlaky organických nebo anorganických reakčních plynů (prekurzorů), které jsou zředěné inertním plynem. Reakce se uskutečňuje na horkém povrchu substrátu, kde dochází k růstu tenké vrstvy nebo nanostruktur. Schéma základního principu metody CVD je zobrazeno na obrázku 1. Tímto způsobem lze deponovat amorfní, polykrystalické, monokrystalické a epitaxní vrstvy dosahující vysoké čistoty.

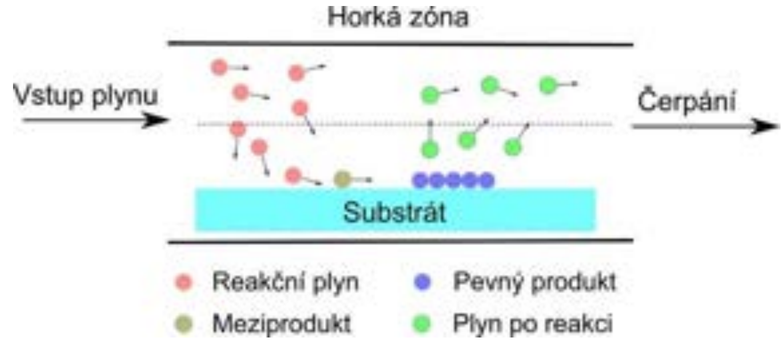

Obrázek 1: Schéma základního principu CVD procesu.

Výhodou CVD metody je zejména její jednoduchost, nízké nároky na vybavení a také možnost růstu širokého spektra materiálů. V současné době existuje mnoho CVD hybridních depoziční metod, které lze rozdělit dle základních principů depozice, jako je například pyrolýza, redukce, oxidace, nitridace a karbonizace. Pyrolýza patří mezi nejjednodušší procesy z rodiny CVD metod, kdy je prekurzor rozkládán na horkém povrchu, přičemž stabilní složky na povrchu vyváří depozici tenké vrstvy. Obvykle se používá teplota reakce v rozsahu 300 ºC až 1 200 ºC, kdy lze ohřívat přímo substrát nebo celou reakční komoru. Výsledná kvalita tenkých a ultratenkých vrstev závisí na tlaku plynu a teplotě substrátu. Je-li nastavena nízká teplota substrátu, je růst vrstvy limitován kinetikou povrchové reakce. Při střední teplotě je její růst omezen dodávaným množstvím reagujících plynů na substrát. Při vysoké teplotě substrátu se rychlost růstu vrstvy snižuje v důsledku desorpce prekurzorů z povrchu.

Jako příklad zařízení užívající pyrolýzu pro růst grafenu z metanu (CH_4) na měděném substrátu při teplotě cca 1000 ºC lze uvést námi navržený a realizovaný CVD reaktor. Ten je primárně určen pro růst grafenu a nalézá se na Ústavu fyzikálního inženýrství, FSI VUT v Brně. Grafenové vrstvy jsou dále využívané studenty při výuce a realizacích jejich bakalářských a diplomových prací [10–19].

Námi navržený systém se skládá z reakční vysokoteplotní části, části dávkující reakční plyny a čerpací části, viz obrázek 2. Vysokoteplotní reakční část pece je tvořena křemennou trubicí o průměru ϕ = 50 mm a délce l = 1 m. Vysoká teplota uvnitř reakční části je získávána radiačním ohřevem od žhaveného odporového drátu rozmístěném kolem trubice. Materiál odporového drátu je tvořen slitinou železa s obsahem chromu, hliníku a kobaltu, který je registrován pod obchodní značkou „Kanthal". Měření teploty lze provádět přímo uvnitř CVD pece užitím termočlánku typu R, nebo nepřímo termočlánkem nacházejícím se na vnější straně křemenné trubice. Z důvodů omezení kontaminace kovy připravovaných vrstev je preferována druhá varianta měření teploty. Uložení a napojení trubice

je realizováno pomocí dvou nerezových přírub stahujících vitonové těsnění vytvářející rozebíratelný těsnící třecí spoj. Tento spoj je přes příruby aktivně chlazen průtokem vody. Tímto uspořádáním lze dlouhodobě získat v reakční komoře teplotu až 1 100 °C.

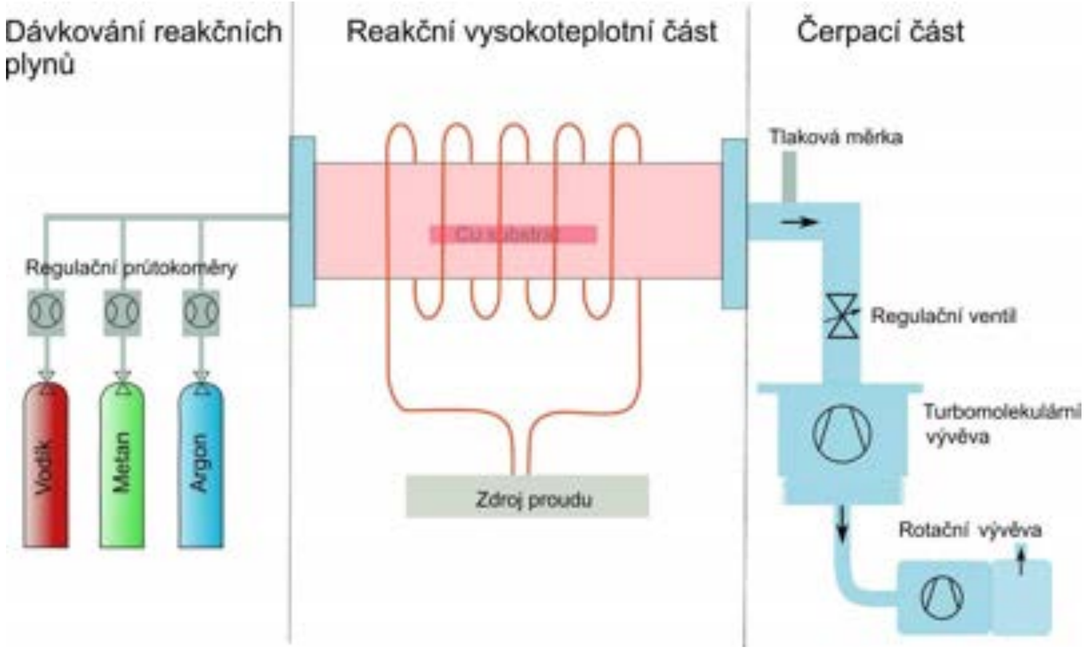

Obrázek 2: Schéma CVD aparatury pro růst grafenu vyvinuté na Ústavu fyzikálního inženýrství, FSI VUT v Brně.

Rozvod plynů do reakční části je vyhotoven z nerezového chemicky leštěného potrubí, které je napojeno na tlakové lahve. Materiál prekurzoru lze také získávat ohřevem pevnolátkových či kapalných materiálů umístěných do zásobníků. Takto byl například zplyňován prášek borazinu $B_3H_6N_3$ při růstu 2D nitridboritých (BN) vrstev. Přesné dávkování plynů do reakční komory je zajištěno digitálně ovládanými průtokoměry od firmy MKS dávkujícími plyn v rozsahu toků 0-10 sccm a 0-1000 sccm. Tyto nastavitelné průtokoměry jsou řízeny počítačovým programem, který umožňuje přesné nastavení a monitorování pracovních podmínek, jakými jsou průtok plynu, tlak v komoře a čerpací rychlost vývěv.

Čerpání CVD reaktoru je zajištěno turbomolekulární vývěvou, která je předčerpávána olejovou rotační vývěvou, čímž je dosahováno základního tlaku v komoře 1×10^{-1} Pa. Tlak v komoře lze ovlivnit digitálně ovládaným škrticím ventilem, který je umístěn mezi komorou a čerpací vývěvou.

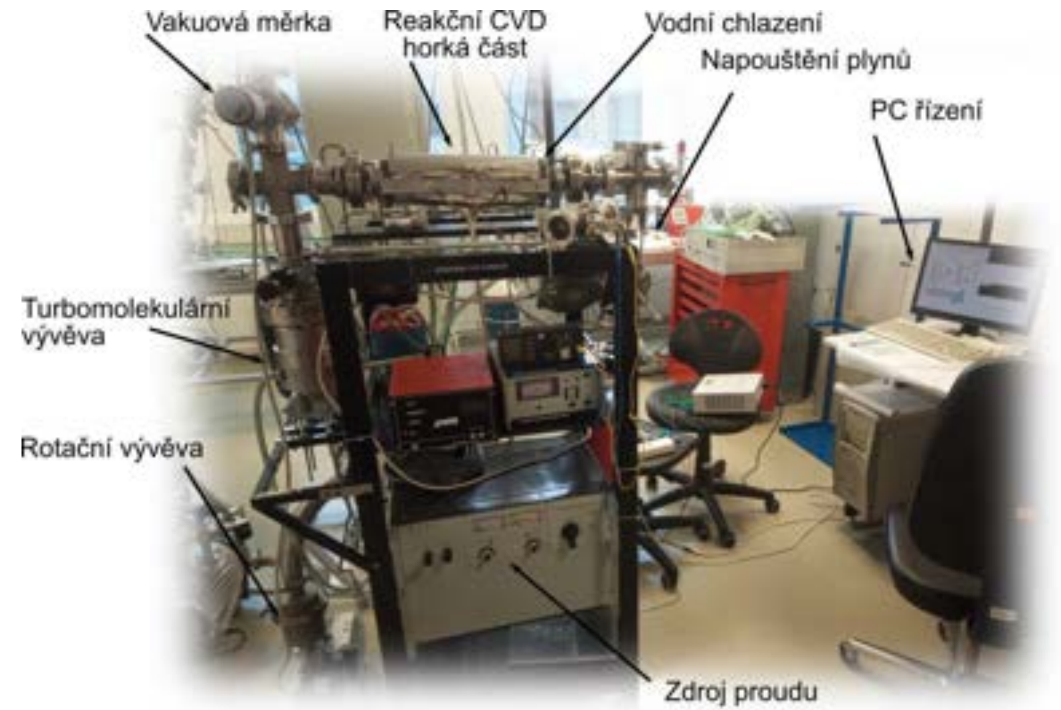

Obrázek 3: Fotografie CVD reaktoru určeného pro růst grafenových vrstev vyvinutého na Ústavu fyzikálního inženýrství, FSI VUT v Brně.

2.1 Aplikace navrženého a realizovaného CVD reaktoru – příprava grafenu metodou CVD

Námi navržený a realizovaný CVD reaktor (viz obrázek 3) je používán primárně pro růst grafenu, což představuje jednu monovrstvu atomů uhlíku s hexagonální mřížkou. Tato vrstva vykazuje unikátní elektrické a mechanické vlastnosti [20]. Růst grafenu v CVD reaktorech se převážně realizuje na substrátech z přechodových kovů, jako například mědi, niklu, železe a kobaltu [21–23], které současně slouží jako katalyzátor reakce. Měděný substrát se dosud jeví jako nejvhodnější materiál pro syntézu jednovrstevnatého grafenu, zejména z důvodu nízké rozpustnosti uhlíku v mědi. Vyšší míra rozpustnosti uhlíku v kovech podporuje během fáze chladnutí kovu zvýšenou precipitaci uhlíku na povrch substrátu vedoucí k nežádoucí tvorbě vícevrstevnatého grafenu. U měděného substrátu probíhá samoregulační růstový proces, kdy po celkovém pokrytí substrátu grafenem dojde k zastavení katalytického rozkladu prekursoru a tím i zastavení růstu dalších vrstev grafenu. Například niklové substráty mají vyšší míru rozpustnosti uhlíku, čehož lze v některých případech užít k výrobě a následnému studiu základních vlastností vícevrstevnatého grafenu [24].

Obecně se pro depozici grafenu užívá měděná folie připravovaná válcováním, která se následně žíhá v CVD reaktoru za vysoké teploty (1 000 °C) ve vodíkové atmosféře. Hrubý povrch vzniklý vlivem mechanické výroby lze upravit chemickým leptáním a následným žíháním. Nicméně po takové úpravě povrch měděného substrátu zůstává stále značně hrubý. Z těchto důvodů jsme navrhli unikátní postup přípravy Cu folie s ultra-hladkým povrchem. Při této metodě je na hladký povrch křemíkové desky s nativní vrstvou SiO_2 narostena 600 nm tlustá vrstva Cu[1]. Následně je tato vrstva zesílena elektrolytickou depozicí mědi. Po dosažení samonosné tloušťky je Cu vrstva sloupnuta z Si substrátu,

[1] Cu vrstva byla připravena naprašováním pomocí metody depozice za asistence iontových svazků (IBAD) na ÚFI.

viz obrázek 4a). „Sloupnutá“ Cu vrstva na rozhraní kopíruje hladký povrch Si/SiO_2. Folie v místě rozhraní Si/Cu dosahuje drsnosti Ra < 0,5 nm. Na obrázku 4b) je zobrazeno porovnání měření topografie povrchu pomocí AFM na superultra-hladké měděné folii a běžně užívané folii vyráběné válcováním. Obě folie byly žíhány při teplotě 1 000 °C ve vodíkovém prostředí a následně vystaveny působení metanu (CH_4), který se vlivem pyrolýzy rozkládal na vodík a uhlík. Během této reakce uhlíkové atomy na měděném substrátu formují grafenovou vrstvu. Pro většinu experimentů a aplikací je nutné tuto vrstvu přenést na jiný substrát, jako je například křemík. Přenos lze realizovat mnoha způsoby, mezi nejznámější patří tzv. mokrá metoda. Při ní se chemicky odleptá měděná folie a grafen se „nabere“ na požadovaný povrch. Podrobný popis výroby ultra-hladké folie s grafenem včetně jeho přenosu a měření jeho elektrických transportních vlastností nalezneme v článku přiloženém v části 2.1.1.

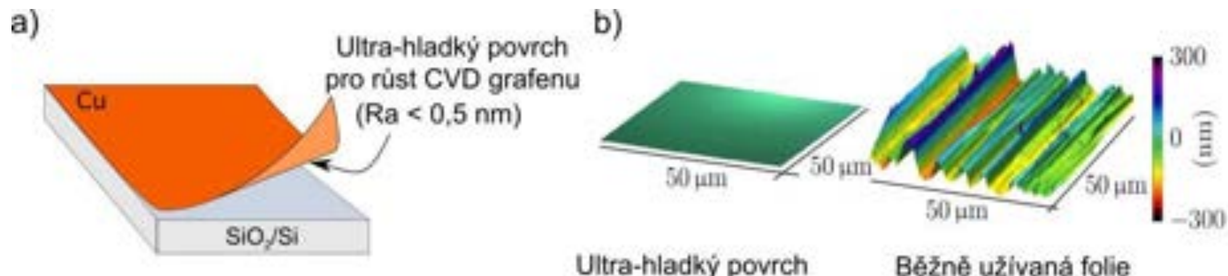

Obrázek 4: a) Schéma přípravy ultra-hladké měděné vrstvy sloupnutím měděné vrstvy z povrchu SiO_2 na Si. b) Porovnání topografie povrchů měřených metodou AFM pro ultra-hladkou a standardní měděnou folii pokrytou CVD grafenovou vrstvou.

Grafen nachází široké uplatnění v polovodičovém průmyslu a jeví se velmi perspektivní například k výrobě jednoelektronového tranzistoru [24], solárních článků [6] a různých senzorů [25]. Jako příklad aplikace grafenové vrstvy uvádím námi vyhotovený senzor vlhkosti (část 2.1.2). Tento senzor je uspořádán obdobně jako FET tranzistor, kdy mezi dvěma elektrodami (source - emitor, drain - kolektor) je umístěna grafenová vrstva jako vodivý kanálek. Toto uspořádání je vytvořeno na křemíkovém substrátu s izolující vrstvou SiO_2 (tloušťky 280 nm). Křemíkový substrát slouží k přivedení hradlového napětí a grafenová vrstva tvoří aktivní detekční plochu. Uspořádání senzoru je schematicky znázorněno na obrázku 5. Využitím takto připraveného senzoru byly studovány základní fyzikální mechanismy vlivu okolní vlhkosti na transportní vlastnosti grafenu. Diskuse námi odhaleného chování senzorů vlhkosti na bázi grafenu v závislosti na proměnném tlaku nasycených vodních par (v odpovídajícím rozsahu od atmosférického až po tlak 1×10^{-7}Pa) jsou podrobně popsány v přiloženém článku uvedeném v části 2.1.2.

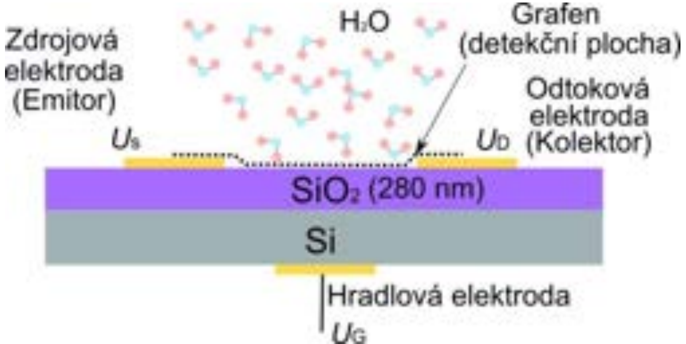

Obrázek 5: Schéma senzoru vlhkosti s grafenovou vrstvou (FET uspořádání).

Jinou alternativní aplikaci grafenové vrstvy představuje námi vyhotovený Schottkyho solární článek s grafenovou vrstvou, kdy na rozhraní grafenu s křemíkem dochází k vzniku ochuzené zóny. Účinnost zmíněných námi vyrobených solárních článků dosahovala 4,43 % [15, 16, 18].

2.1.1 Článek č. 1 - Ultra-hladká kovová folie pro růst vysoce kvalitního grafenu metodou depozice s plynné fáze

Autoři:

P. Procházka, **J. Mach**, D. Bischoff, Z. Lišková, P. Dvořák, M. Vaňatka, P. Simonet, A. Varlet, D. Hemzal, M. Petrenec, L. Kalina, M. Bartošík, K. Ensslin, P. Varga, J. Čechal a T. Šikola

Nanotechnology [online]. 2014, **25**(185601), 1–8. Dostupné z: doi:10.1088/0957-4484/25/18/185601

Abstrakt:

Příprava grafenu chemickou depozicí z plynné fáze je slibnou cestou pro výrobu vysoce kvalitního grafenu o velkých rozměrech pro elektronické aplikace. Kvalita užívaných substrátů hraje klíčovou roli, protože drsnost povrchu a defekty mění růst grafenu a způsobují potíže při následném přenosu grafenu. V článku pojednáváme o přípravě vysoce čisté ultra-hladké měděné folie připravené naprašováním z tenké vrstvy Cu na vrstvu SiO_2/Si, která slouží jako šablona, a následné odlepení kovové vrstvy od této šablony. Povrch vykazuje nízkou úroveň oxidace a znečištění. Drsnost povrchu folie je obecně definována povrchem šablony a byla pod hodnotou 0,6 nm i na velkých plochách povrchu folie. Drsnost a velikost zrn se zvyšuje jak při žíhání folie, tak při katalytickém růstu grafenu z metanu (≈ 1000 °C), ale ve velkém měřítku stále zůstává hluboko pod hodnotou drsnosti typickou pro běžně užívané folie. Mikro-Ramanova spektroskopie a měření transportních vlastností prokázaly vysokou kvalitu grafenu rosteného na takto připravovaných foliích. Pohyblivost nosičů náboje při pokojové teplotě grafenu rosteném ze šablony sloupnuté Cu folii byla třikrát vyšší ve srovnání s grafenem rosteném na komerčně vyráběné měděné fólii. Předpokládá se, že popsané vysoce kvalitní měděné fólie budou užity jako velkoplošné substráty pro výrobu grafenu vhodného pro elektronické aplikace.

IOP Publishing Nanotechnology
Nanotechnology 25 (2014) 185601 (8pp) doi:10.1088/0957-4484/25/18/185601

Ultrasmooth metallic foils for growth of high quality graphene by chemical vapor deposition

Pavel Procházka[1,2], Jindřich Mach[1,2], Dominik Bischoff[3], Zuzana Lišková[1,2], Petr Dvořák[1,2], Marek Vaňatka[2], Pauline Simonet[3], Anastasia Varlet[3], Dušan Hemzal[4], Martin Petrenec[5], Lukáš Kalina[6], Miroslav Bartošík[1,2], Klaus Ensslin[3], Peter Varga[1], Jan Čechal[1,2] and Tomáš Šikola[1,2]

[1] CEITEC—Central European Institute of Technology, Brno University of Technology, Technická 3058/10, 616 00 Brno, Czech Republic
[2] Institute of Physical Engineering, Brno University of Technology, Technická 2896/2, 616 69 Brno, Czech Republic
[3] Solid State Physics Laboratory, ETH Zurich, Schafmattstrasse 16, CH-8093 Zurich, Switzerland
[4] CEITEC—Central European Institute of Technology, Masaryk University, Kamenice 753/5, 625 00 BRNO, Czech Republic
[5] Tescan Orsay Holding, a.s., Libušina Třída 21, 623 00 Brno, Czech Republic
[6] Brno University of Technology, Faculty of Chemistry, Centre for Materials Research, Purkyňova 464/118, Brno, 612 00, Czech Republic

E-mail: cechal@fme.vutbr.cz

Received 27 January 2014, revised 7 March 2014
Accepted for publication 13 March 2014
Published 16 April 2014

Abstract

Synthesis of graphene by chemical vapor deposition is a promising route for manufacturing large-scale high-quality graphene for electronic applications. The quality of the employed substrates plays a crucial role, since the surface roughness and defects alter the graphene growth and cause difficulties in the subsequent graphene transfer. Here, we report on ultrasmooth high-purity copper foils prepared by sputter deposition of Cu thin film on a SiO_2/Si template, and the subsequent peeling off of the metallic layer from the template. The surface displays a low level of oxidation and contamination, and the roughness of the foil surface is generally defined by the template, and was below 0.6 nm even on a large scale. The roughness and grain size increase occurred during both the annealing of the foils, and catalytic growth of graphene from methane (≈1000 °C), but on the large scale still remained far below the roughness typical for commercial foils. The micro-Raman spectroscopy and transport measurements proved the high quality of graphene grown on such foils, and the room temperature mobility of the graphene grown on the template stripped foil was three times higher compared to that of one grown on the commercial copper foil. The presented high-quality copper foils are expected to provide large-area substrates for the production of graphene suitable for electronic applications.

S Online supplementary data available from stacks.iop.org/NANO/25/185601/mmedia

Keywords: graphene, CVD growth, metallic foils

(Some figures may appear in colour only in the online journal)

0957-4484/14/185601+08$33.00 1 © 2014 IOP Publishing Ltd Printed in the UK

Introduction

Graphene has attracted enormous attention for its unique mechanical, optical and electronic properties [1–3]. Synthesis by means of chemical vapor deposition (CVD) catalyzed by metallic substrates is a promising route for fabrication of high-quality large-area monolayer graphene sheets [4, 5]. Here, the copper foils are among the most promising substrates for the CVD growth of graphene thanks to low carbon solubility in Cu [4], and low concentration of defects formed in graphene compared to Co and Ni substrates [6–8]. Since domain boundaries have a deleterious effect on the electronic properties of graphene [9–11], intense research is being carried out on the CVD growth of large-area single-domain graphene [7, 12–15]. The single domain growth has been achieved by synthesis at high temperatures and the presence of hydrogen [13, 16, 17] when nucleation of carbon atoms on surface defect sites is restricted [13, 17–19], or by oxygen passivation of potential nucleation sites [14, 15]. The quality of the employed metallic foils, therefore, plays a crucial role in the growth process [17, 18, 20]. In addition, the surface morphology of the foils is critical for the formation of wrinkles on graphene during its transfer to insulating substrates [21, 22]. Commercially available foils generally possess high surface roughness, mainly due to the metal rolling process during their production [7]. Therefore, the metal foils are usually electropolished and annealed at high temperatures (>1000 °C) under vacuum or hydrogen atmosphere for several hours [12, 13, 18, 20, 23, 24], or the copper is melted and resolidified on a tungsten foil support [25] to clean and smoothen the surface before the graphene growth. However, after this process, the surface roughness over larger areas remains relatively high and has a significant influence on the growth and transfer processes. Another issue is the purity of the copper foil since the impurity atoms often segregate on the surface in the form of clusters [26], causing an increase in the nucleation center density.

Here, we introduce a template stripping method [27–29] for the fabrication of ultrasmooth copper metallic foils, whose surface roughness is defined by the employed templates, i.e. silicon substrates, which display one of the smoothest commercially available surfaces. The resulting large-area roughness of the prepared foils (typically over $50 \times 50\,\mu m^2$) is below 0.6 nm, i.e. almost two orders of magnitude lower than the one observed on commercial Cu foils.

The template-stripping method brings an additional advantage of very low surface contamination and oxidation because the surface of the foil is freshly exposed to ambient atmosphere after its stripping. Hence, the electropolishing and high temperature cleaning of the Cu foil before the graphene growth can be avoided. The size of the foils prepared by this method is practically limited only by the available template-size, which presents an advantage for the production of graphene on a large scale, and ensures the compatibility of the method with the semiconductor industry.

Methods

Graphene films were primarily grown on template stripped (TS) copper foils and, for comparison, also on 25 μm-thick polycrystalline copper foils from the MTI Corporation (purity > 99.99%). The commercial copper foils were cleaned in an ultrasonic bath for 15 min in acetone and 15 min in isopropanol, then inserted into the home-built CVD system and annealed at 1000 °C under a hydrogen flow of 4 sccm at 10 Pa before the graphene growth.

The TS copper foils were prepared by ion beam sputter deposition from a high purity copper target (Mateck, 99.999%) in a home-built high vacuum ($<10^{-5}$ Pa) setup based on Kaufman broad ion beam sources [30]. The energy of argon ions was 600 eV and the deposition rate of copper on the template formed by a P-doped Si (100) substrate (resistivity of 0.0010–0.0015 Ω cm) covered with a 280–285 nm-thick thermal SiO_2 layer was 2.3 Å s^{-1}. Next, the copper supporting layer was deposited by electrolysis in a mixture of 0.0012 M sulfuric acid (H_2SO_4) and 1.38 M solution of Copper Sulfate ($CuSO_4$, 33 g, 150 ml). The current and time of electrodeposition were controlled during the whole process in order to achieve the required thickness of the supporting layer (24 μm). The stripping of the foils was carried out just prior to their insertion into the reactor to reduce the contamination and oxidation from the ambient atmosphere.

Graphene synthesis was carried out in a home-built reactor (see supporting information for details, available at stacks.iop.org/NANO/25/185601/mmedia). Before the growth, hydrogen gas was introduced to the reactor (4 sccm, 10 Pa) and the system had been heated up to a graphene growth temperature. Graphene growth was performed under a methane atmosphere (flow of 40 sccm) for 30 min at a pressure of 70 Pa. Afterwards, the system was cooled down to room temperature in four hours. Graphene from the back-side of the copper foil was removed by oxygen plasma etching (25% O_2/75% Ar, two minutes).

To provide further analysis, the graphene layer from the front side of the foil was transferred to a SiO_2/Si substrate (the same type of substrate as that used for the template of the TS copper foils) by the PMMA-assisted wet transfer method.

Atomic force microscopy (AFM) was carried out by a commercial ambient scanning probe microscope (NT-MDT Ntegra Prima) in contact mode using commercial silicon cantilevers CSG-10 (NT-MDT). The image resolution was set to a standard of 256 × 256 points. A conventional confocal Raman microscope WITec CRM 200 with a green laser (532.2 nm, 0.8 mW) and spot diameter of 450 nm, and Renishaw inVia with a He-Ne excitation laser (632.8 nm, 50 mW) and a focused spot diameter of 2 μm were used for the room temperature measurement of the Raman spectra and spatial maps. X-ray photoelectron spectroscopy was performed in a Kratos Axis-Ultra DLD system using monochromatic Al-Kα radiation. Transport properties were measured at room temperature or at 4 K in a liquid He cooled cryostat. Electron backscatter diffraction (EBSD) measurements were carried out in a Tescan FERA 3 microscope equipped by NordlysMax [2] EBSD detector from Oxford

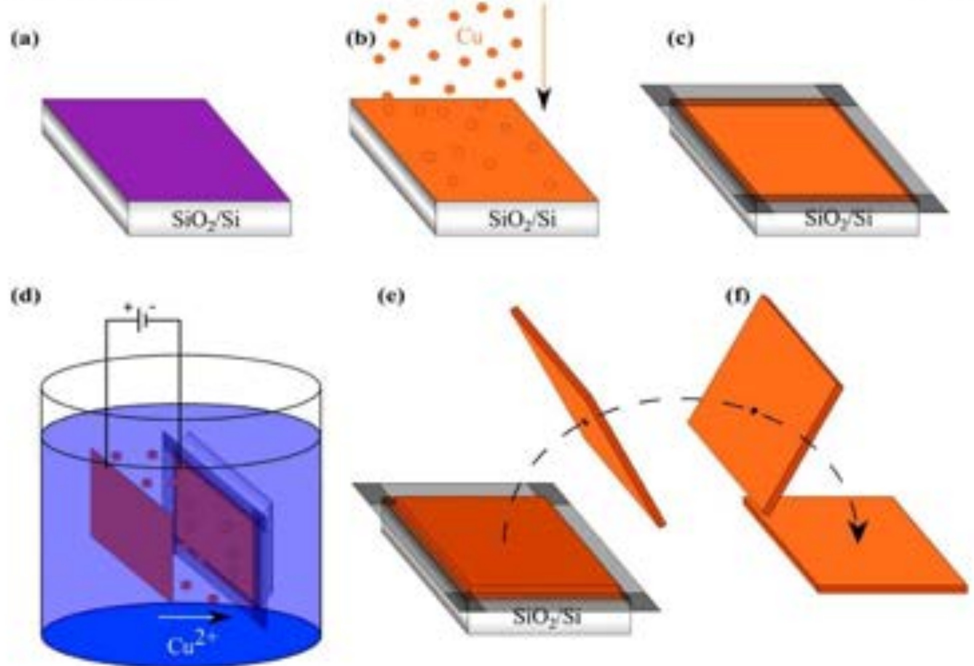

Figure 1. Preparation of a copper foil by template stripping. (a) SiO_2/Si substrate as a template. (b) Sputter-deposition of Cu. (c) Protection of edge areas of the substrate surface. (d) Electrodeposition of a thick Cu supporting layer. (e) Peeling-off the prepared foil. (f) The top layer of the foil is defined by the SiO_2/Si template surface.

Instruments, using 8 and 15 keV primary electron beams focused to the spot with a diameter of 15 nm at a sample inclined by 70 degrees relative to the incoming electron beam. The assignments of crystallographic directions were performed directly in the Aztec EBSD control software, and EBSD Post-processing was completed by HKL CHANNEL5.

Results and discussion

Figure 1 illustrates the preparation of the copper foils by template stripping using a silicon-based substrate as a template. In the first step, a 800 nm-Cu thin film is sputter deposited in a broad ion-beam setup [30] on the Si(100) substrate with a 280 nm-thick thermally grown SiO_2 layer on top of it. This is followed by the electrodeposition of a 24 μm-thick supporting Cu layer from the $CuSO_4$ solution. A key step here is to cover the edges of the sample by a resist layer (PMMA) or scotch tape to prevent penetration of the electrolyte to the Cu/Si interface from the side of the sample. After completing the electrodeposition, the sample is rinsed in demineralized water and dried out under ambient conditions for at least 24 h. The free-standing copper foil is then obtained by mechanically peeling-off the copper layer from the substrate. This step is enabled by the low adhesion of the Cu layer to the SiO_2 surface (see supporting information for a more detailed discussion, available at stacks.iop.org/NANO/25/185601/mmedia).

The surface of the foils prepared in this way has very low roughness and their material composition is primarily defined by the composition of a target used for sputter deposition. In our case we have used a Cu target with 99.999% purity, and x-ray photoelectron spectroscopy (XPS) revealed no traces of contamination, except for impurities from the ambient atmosphere (see supporting information, available at stacks.iop.org/NANO/25/185601/mmedia). Compared to standard Cu-foils, which are usually stored under ambient conditions, the freshly stripped TS foils show a very low level of contamination and oxidation because their surface is protected from ambient conditions while attached to the template.

Figure 2(a) shows the in-scale comparison of the large-area surface morphology of the TS foils and non-treated commercial polycrystalline copper foils (99.99%, MTI Corporation) which are frequently used for CVD graphene growth. The surface of the commercial foil presented in the bottom part of figure 2(a) displays large corrugation (arithmetic-averaged roughness $R_a = 70$ nm and root-mean-squared roughness (RMS) $R_{RMS} = 90$ nm) over a large area (50×50 μm^2), which is typical for the foils prepared by cold rolling. On the local scale (measured area of 1×1 μm^2), the roughness of the commercial foils is correspondingly lower (typically $R_a = 8.6$ nm and $R_{RMS} = 11$ nm). A detailed inspection of the surface of the foils prepared by template stripping, illustrated

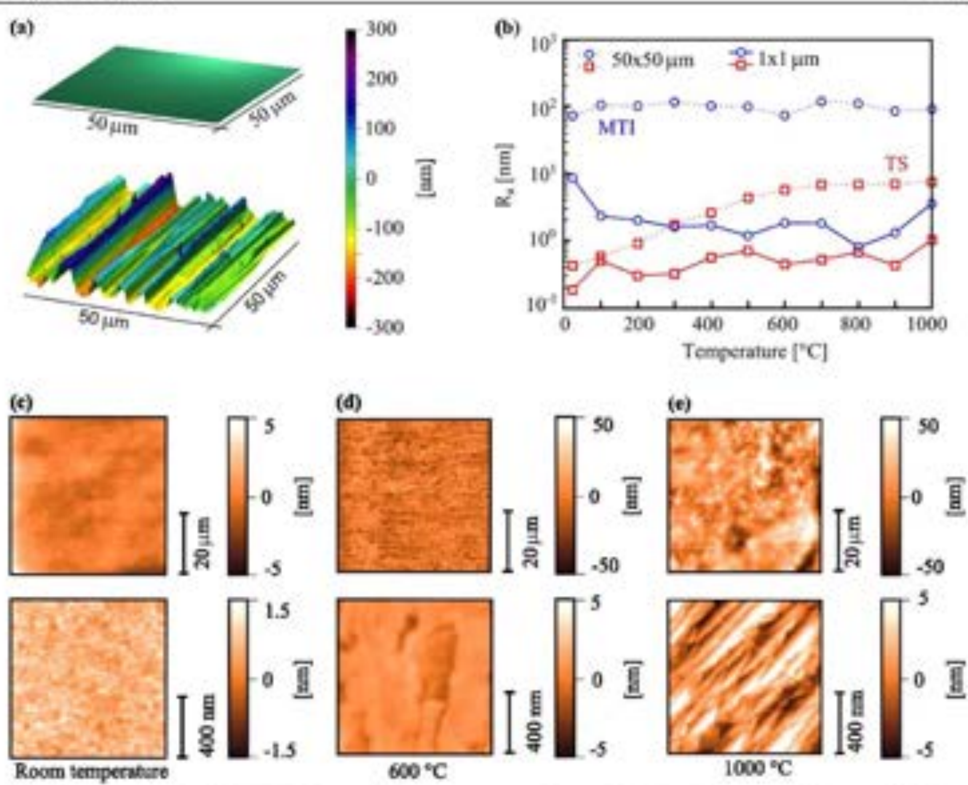

Figure 2. (a) AFM topography ($50 \times 50\,\mu m^2$) of copper foils prepared by template stripping (top) and commercial copper foils (bottom). (b) Surface roughness (in logarithmic scale) of the copper foils after 30 min annealing under a low-pressure hydrogen atmosphere at different temperatures and measured over $50 \times 50\,\mu m^2$ and $1 \times 1\,\mu m^2$ surface areas (red: TS copper foil, blue: commercial copper foil). AFM images of TS copper foils: (c) as prepared, (d) vacuum annealed at 600 °C, and (e) 1000 °C, (top row $50 \times 50\,\mu m^2$; bottom row $1 \times 1\,\mu m^2$).

in figure 2(c), reveals very small surface roughness on a large scale ($R_a = 0.42$ nm and $R_{RMS} = 0.53$ nm, top image) and appropriately lower on a local scale ($R_a = 0.18$ nm and $R_{RMS} = 0.23$ nm, bottom image); no morphological features were found at both size-scales. On both foils, the large area measurements are taken to cover a sufficient area to make statistical conclusions on surface roughness.

To reveal the changes in surface morphology of the foils with increasing process temperature, we have carried out two series of experiments in a CVD apparatus: (1) annealing of the foils at 100–1000 °C in a vacuum (10^{-3} Pa), and (2) annealing of the foils in the same way and their subsequent exposure to a methane at 300–1000 °C (CVD process).

The annealing in a vacuum/hydrogen atmosphere is a typical step used for cleaning commercial copper foils prior to graphene synthesis itself [12, 13, 18, 20, 23, 24]. The dependence of surface roughness for this type of annealing is depicted in figure 2(b). In each experiment, a freshly prepared TS copper foil was used and the annealing was carried out simultaneously with the commercial foil in order to provide a direct comparison. With an increasing annealing temperature, the morphology of the TS foils (figures 2(d) and (e)) changes. The most prominent change is the formation of depressions and pits on the substrate (600 °C) and micro-faceting observed after high temperature annealing (1000 °C). The original size of the grains after deposition is very small since the sputter deposition technique was used and no post-annealing treatment applied. This method generally results in the formation of small crystallites in an amorphous matrix [31]. To confirm this, we have performed EBSD analysis of the TS foils (see supporting information for a detailed description of results, available at stacks.iop.org/NANO/25/185601/mmedia). Indeed, the average grain size amounts to 60 nm, and a relatively large portion of the surface area could not be assigned and, hence, it is amorphous or contains clusters smaller than ~20 nm.

EBSD performed after annealing at 1000 °C reveals that the size of near surface grains increases: the average grain size increases to 320 nm. Further, there is a dramatic change in the grain orientation. Whereas on the pristine TS foil the majority of grains possesses the (111) surface orientation, the annealed foil displays multiple grain orientations with a minor preference for the (111) and (100) planes and orientations close to these two planes.

During annealing, the grains in the foil grow which leads to an increase of surface roughness. Since the surface of the

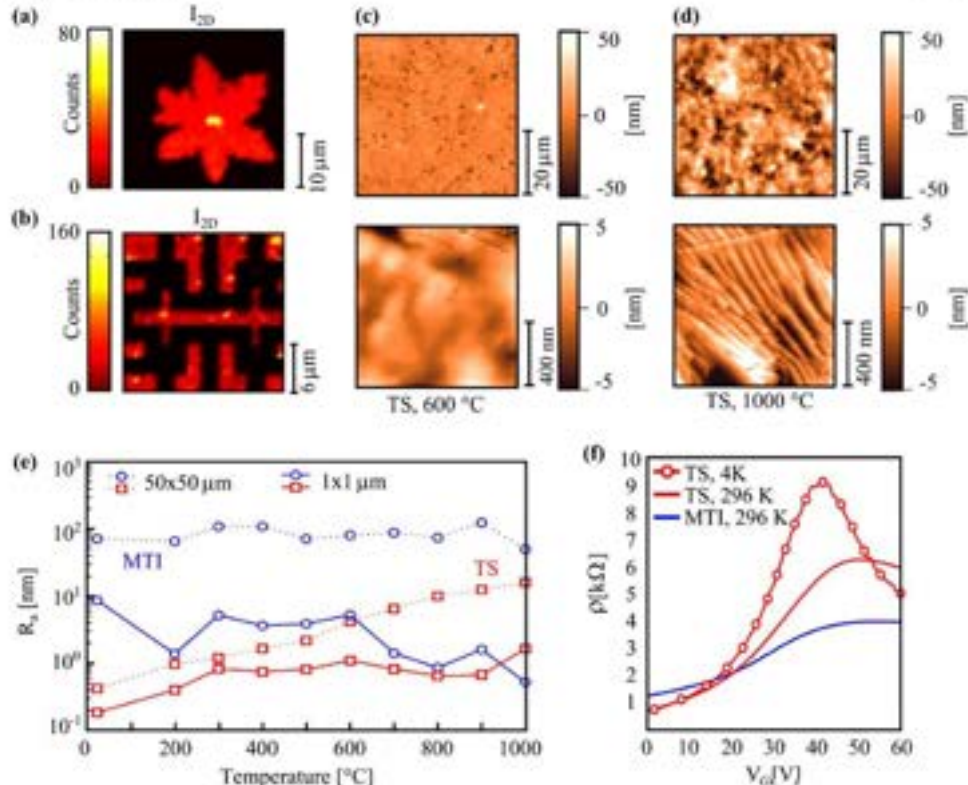

Figure 3. (a, b) Maps of the 2D-Raman peak intensity over (a) a single graphene domain grown on the TS foil and (b) polycrystalline graphene grown on the commercial copper foil with prepared contacts. Both graphene layers were grown at 1000 °C and transferred onto the SiO_2/Si substrate. (c, d) AFM images of the TS copper foils annealed in hydrogen atmosphere and then exposed to methane at 600 °C (c), and 1000 °C (d) (top row $50 \times 50\ \mu m^2$; bottom row $1 \times 1\ \mu m^2$). (e) Surface roughness (in logarithmic scale) of copper foils after their annealing in a hydrogen atmosphere and consequent exposure to methane at various process temperatures obtained from $50 \times 50\ \mu m^2$ and $1 \times 1\ \mu m^2$ scans (red: TS copper foil, blue: commercial copper foil). (f) Graphene resistivity as a function of applied back-gate voltage for graphene grown on the commercial copper foil (blue: room temperature) and TS foil (red: room temperature, black: 4 K).

foil is no longer covered by the Si template, and the freshly exposed areas are not necessarily of the lowest surface free energy, the grains tend to reach their equilibrium shapes and protrude out of the original surface. The material forming these grains is taken from the surrounding areas and grain boundary grooves (pits) are formed [18]. The other source of roughening is the evaporation and sublimation of copper atoms [32] which results in the overall increase of the surface roughness. Both these effects have no direct influence on the measured roughness of commercial copper foils, because their roughness is determined mainly by rolling stripes. Even though the roughness of the TS foils increases with temperature, it is still on a large scale—ten times lower than that one of the commercial foils.

In the second series of experiments, we have examined the morphology of copper foils after their annealing in a hydrogen atmosphere (10 Pa, 4 sccm) and subsequent exposure to a methane atmosphere (70 Pa, 40 sccm) at various process temperatures. The evolution of the surface roughness with process temperature is presented in figure 3(e). From the AFM images taken after the 600 °C (figure 3(c)) and 1000 °C (figure 3(d)) experiments, it is evident that the combination of annealing and CVD process leads to similar morphological changes, as observed during annealing in hydrogen (i.e. the formation of pits and microfaceting). However, the increase in roughness is higher (up to 2 times), especially at high temperatures (≈1000 °C) when graphene growth was obtained (see below). The low surface roughness can be maintained by low temperature graphene synthesis. This, however, did lead to graphene of medium quality (see supporting information for details, available at stacks.iop.org/NANO/25/185601/mmedia). So we will further focus on graphene growth from the methane precursor.

To evaluate the quality of the grown graphene layers, we performed transport measurements and micro-Raman spectroscopy. The minimum temperature for the graphene growth deduced from the appearance of the 2D-peak is 900 °C. However, the graphene quality further improves with increasing growth temperature. In figures 3(a) and (b), the areal distribution (map) of the 2D-Raman peak intensities of

the graphene grown at 1000 °C on both foils and transferred onto the SiO_2/Si substrate is shown. The maps of both individual peak (2D and G) intensities and associated Raman spectra are presented in the supporting information, available at stacks.iop.org/NANO/25/185601/mmedia. The intensity ratio of the 2D and G peaks in the graphene domains and absence of D-peak proves that the single-layer graphene has a very low amount of defects. The uniform distribution of the 2D-peak intensity over the domains indicates a high homogeneity of the graphene. The best quality graphene samples were grown at 1000 °C, which is in agreement with the recently published results on CVD graphene grown on commercial copper foils [4, 7, 11, 13]. However, the large scale roughness of our TS foils is lower compared to commercial ones and, consequently, that of the graphene as well.

The regularly used copper foils prepared by cold rolling display rolling stripes as a main morphological feature. These can be smoothed by high temperature annealing but cannot be removed completely [13, 18]. Moreover, the pre-annealing can result in the formation of a 'crust' layer which can easily peel off from the surface [33]. Another way to smooth the surface is by electropolishing and etching. Electropolishing can reduce the surface roughness to about 3 nm, but the observed pit formation can result in large defects in graphene [18]. In other studies on electropolishing of graphene, the reduction of RMS roughness from 219 nm to only 64 nm [24], or even less [13], was observed. The main advantage of electropolishing is thus the removal of surface oxides [24]. Moreover, the contamination of the foil surface by the electrolyte or segregation of impurities at the surface during high temperature annealing can take place. The etching (e.g. using $Fe(NO_3)_3$) also does not lead to satisfactory results, since etch quarries and residues are left on the surface, even after subsequent foil annealing [33].

In comparison, the TS foils possess no rolling stripes, their surface is inherently ultra-clean and oxide-free, and hence both cleaning steps can be omitted. The main drawback of the TS foils might be that of a small grain size, and hence a high number of substrate grain boundaries which generally cause an increase in roughness of the foils during annealing, and may also act as additional nucleation centers for graphene domains. Concerning the graphene growth, substrate grain boundaries do not present significant restriction since graphene domains easily extend their growth over several substrate grains [34]. Additionally, the higher density of atomic steps on microfacets formed after annealing could help with healing point defects in the graphene layer [35]. Further, the high purity of these foils implies that the amount of impurities segregating on the surface is very low. These impurities present significant issues since the nucleation on these cannot be easily suppressed by the increase of growth temperature [17]. Hence, by further optimization of the method, we expect that the TS foil will make it possible to grow graphene layers of superior quality compared to those recently prepared on standard copper foils.

Due to the distinct nature of the surfaces of TS- and commercial-Cu foils, the growth of graphene under the same conditions differs. In the case of commercial foils, the whole surface is covered by polycrystalline single layer graphene, whereas on the TS foil the graphene grows in separated larger crystals. This difference can be explained by the lower concentration of defects on the TS foil and, hence, a lower concentration of nucleation sites, so it takes longer to fill the entire surface.

To evaluate graphene transport properties, we transferred the graphene grown on both types of the copper foil on a highly doped silicon substrate acting as a back gate, covered with a 285 nm-thick oxide barrier. We then performed two-point measurements of charge carrier mobility. It should be noted that after the graphene transfer, no annealing steps to improve graphene quality have been carried out in order to accurately distinguish the quality of the samples. We contacted the polycrystalline graphene layer (commercial foil) with Au/Ti contacts in a Hall bar geometry (figure 3(b)) and the separate graphene areas grown on the TS foil (figure 3(a)) with two contacts. Resistivity ρ shown in figure 3(f) and measured resistance R are related via the structure length L and width W by the formula $\rho = RW/L$ (in case of the Hall bar structure $W = 19\,\mu m$ and $L = 2\,\mu m$, in case of the single crystal domain $W = 12\,\mu m$ and $L = 12\,\mu m$). Carrier mobility was deduced according to Drude's model of diffusive transport $\mu = (ne\rho)^{-1}$ for the electron surface concentration $n = 2 \cdot 10^{12}$ cm^{-2}. The measured room temperature mobility of the graphene grown on the commercial copper foil was around 1200 $cm^2\,V^{-1}\,s^{-1}$ with an extracted saturation density [36] of $n_{sat} \sim 9 \cdot 10^{11}\,cm^{-2}$, whereas the mobility of the graphene grown on the TS foil was, at the same conditions, 3 times higher, i.e. around 3600 $cm^2\,V^{-1}\,s^{-1}$ ($n_{sat} \sim 8 \cdot 10^{11}\,cm^{-2}$). The low temperature (4 K) transport measurements gave us the mobility around 4400 $cm^2\,V^{-1}\,s^{-1}$ ($n_{sat} \sim 8 \cdot 10^{11}\,cm^{-2}$) for TS-foil grown graphene; in this case the Dirac point is shifted to a lower value of about 42 V. This difference in mobility of graphene fabricated on two distinct types of copper foils can be explained by the higher concentration of domain boundaries present on the graphene prepared on the standard copper foil. The domain boundaries have been identified as the primary cause of the mobility decrease in CVD grown graphene [11]. It should be noted that the strong shift of the charge neutrality point to high back-gate voltages (>40 V) indicates strong p-doping. This is usually caused by the presence of water and organic residues from the transfer process. It was reduced by thermal annealing of the sample at 130 °C for 48 h in a vacuum, and led to the shift of the charge neutrality point to 18 V while the room temperature mobility retained the same level [11].

We would like to note that the obtained mobilities of 3600 $cm^2\,V^{-1}\,s^{-1}$ do not present the state-of-the-art values beyond the 10 000 reported for CVD graphene [13, 37]. This is caused mainly by the fact that we did not make any attempts for improving the graphene quality (e.g. by etching, annealing) in order to make a fair comparison of both types of graphene samples. We infer that by further optimization of the transfer process and cleaning, the higher mobility values will be obtained. However, the main advantages of the TS foils (e.g. absence of detrimental morphological features, high

purity of the near-surface layer and their clean surface) make them superior over the commercial ones.

Recently, other high quality substrates employed for the CVD graphene synthesis have been reported, e.g. metal single crystals [38] and thin epitaxial layers of transition metals prepared on sapphire substrates [39–43]. In principle, our method can also be applied to sapphire substrates which may lead to foils with a large grain size and single grain orientation (see supporting information S1 for details, available at stacks.iop.org/NANO/25/185601/mmedia).

Conclusions

In conclusion, we have introduced a template stripping method for the preparation of Cu foils using SiO_2/Si substrates as a template. The 'as prepared' TS foils display a roughness below 0.6 nm even on a large scale, and their purity is primarily determined by the Cu target (>99.999%). However, the annealing of these foils in a low-pressure hydrogen atmosphere and during the CVD graphene synthesis, especially at temperatures around 1000 °C, leads to an increase of foil surface roughness. It is caused, presumably, by copper recrystallization and evaporation and sublimation of copper atoms. Nevertheless, the large scale roughness still remains nearly in one order of magnitude below that of typical commercial foils.

The small amount of roughness and low concentration of defects and impurities result in a low number of nucleation sites, which is an important condition for the preparation of graphene with a large domain size and thus improved transport properties. Even without any extensive attempts to improve the preparation procedure, the foils remain very smooth over a large area, which is the necessary condition for a transfer of wrinkle-free graphene. The room temperature mobility of the graphene grown on the TS foil was 3 times higher (≈3600 $cm^2 V^{-1} s^{-1}$) compared to that one grown on the commercial copper foil, and should be further improved. We expect that by employing the presented well-defined substrates, it would be much easier to control all necessary processes required for obtaining the high quality graphene.

Acknowledgments

This work was supported by the project 'CEITEC—Central European Institute of Technology' (CZ.1.05/1.1.00/02.0068) from European Regional Development Fund, the Grant Agency of the Czech Republic (project No. P102/12/1881), the Technology Agency of the Czech Republic (project No. TE01020233), and the EU 7th Framework Programme (projects SYLICA, No. 286154, and UnivSEM, No. 280566). P P was supported by Sciex fellowship. L K acknowledges the support by the project 'Centre for Materials Research at FCH BUT' (CZ.1.05/2.1.00/01.0012) from ERDF Z L was supported by Brno PhD Talent Scholarship Holder—Funded by the Brno City Municipality. Authors thank FEI Company for providing access to plasma ripper.

References

[1] Geim A K 2009 Graphene: status and prospects *Science* **324** 1530–4
[2] Rao C N R, Sood A K, Subrahmanyam K S and Govindaraj A 2009 Graphene: the new two-dimensional nanomaterial *Angew. Chem. Int. Ed.* **48** 7752–7
[3] Novoselov K S, Falko V I, Colombo L, Gellert P R, Schwab M G and Kim K A 2012 Roadmap for graphene *Nature* **490** 192–200
[4] Li X *et al* 2009 Large-area synthesis of high-quality and uniform graphene films on copper foils *Science* **324** 1312–4
[5] Edwards R S and Coleman K S 2013 Graphene film growth on polycrystalline metals *Acc. Chem. Res.* **46** 23–30
[6] Iwasaki T, Park H J, Konuma M, Lee D S, Smet J H and Starke U 2011 Long-range ordered single-crystal graphene on high-quality heteroepitaxial ni thin films grown on MgO (111) *Nano. Lett.* **11** 79–84
[7] Ago H, Ogawa Y, Masaharu T, Tsuji M, Mizuno S and Hibino H 2012 Catalytic growth of graphene: toward large-area single-crystalline graphene *J. Phys. Chem. Lett.* **3** 2228–36
[8] Wang L, Zhang X, Chan H L W, Yan F and Ding F 2013 Formation and healing of vacancies in graphene chemical vapor deposition (CVD) growth *J. Am. Chem. Soc.* **135** 4476–82
[9] Yu Q *et al* 2011 Control and characterization of individual grains and grain boundaries in graphene grown by chemical vapour deposition *Nat. Mater.* **10** 443–9
[10] Koepke J C, Wood J D, Estrada D, Ong Z-Y, He K T, Pop E and Lyding J W 2013 Atomic-scale evidence for potential barriers and strong carrier scattering at graphene grain boundaries: a scanning tunneling microscopy study *ACS Nano.* **7** 75–86
[11] Song H S, Li S L, Miyazaki H, Sato S, Hayashi K, Yamada A, Yokoyama N and Tsukagoshi K 2012 Origin of the relatively low transport mobility of graphene grown through chemical vapor deposition *Sci. Rep.* **2** 337
[12] Li X *et al* 2010 Graphene films with large domain size by a two-step chemical vapor deposition process *Nano. Lett.* **10** 4328–34
[13] Yan Z, Lin J, Peng Z, Sun Z, Zhu Y, Li L, Xiang C, Samuel E L, Kittrell C and Tour J M 2012 Toward the synthesis of wafer-scale single-crystal graphene on copper foils *ACS Nano.* **6** 9110–7
[14] Zhou H, Yu W J, Liu L, Cheng R, Chen Y, Huang X, Liu Y, Wang Y, Huang Y and Duan X 2013 Chemical vapour deposition growth of large single crystals of monolayer and bilayer graphene *Nat. Commun.* **4** 2096
[15] Hao Y *et al* 2013 The role of surface oxygen in the growth of large single-crystal graphene on copper *Science* **342** 720–3
[16] Li X, Magnuson C W, Venugopal A, Tromp R M, Hannon J B, Vogel E M, Colombo L and Ruoff R S 2011 Large-area graphene single crystals grown by low-pressure chemical vapor deposition of methane on copper *J. Am. Chem. Soc.* **133** 2816–9
[17] Wang H, Wang G, Bao P, Yang S, Zhu W, Xie X and Zhang W-J 2012 Controllable synthesis of submillimeter single-crystal monolayer graphene domains on copper foils by suppressing nucleation *J. Am. Chem. Soc.* **134** 3627–30
[18] Kim H, Mattevi C, Reyes Calvo M, Oberg J C, Artiglia L, Agnoli S, Hirjibehedin C F, Chhowalla M and Saiz E 2012 Activation energy paths for graphene nucleation and growth on Cu *ACS Nano.* **6** 3614–23
[19] Mehdipour H and Ostrikov K 2012 Kinetics of low-pressure, low-temperature graphene growth: toward single-layer, single-crystalline structure *ACS Nano.* **6** 10276–86

[20] Wofford J M, Nie S, McCarty K F, Bartelt N C and Dubon O D 2010 Graphene islands on Cu foils: the interplay between shape, orientation, and defects *Nano. Lett.* **10** 4890–6

[21] Li X, Zhu Y, Cai W, Borysiak M, Han B, Chen D, Piner R D, Colombo L and Ruoff R S 2009 Transfer of large-area graphene films for high-performance transparent conductive electrodes *Nano. Lett.* **9** 4359–63

[22] Liu N, Pan Z, Fu L, Zhang C, Dai B and Liu Z 2011 The origin of wrinkles on transferred graphene *Nano. Res.* **4** 996–1004

[23] Murdock A T, Koos A, Britton T B, Houben L, Batten T, Zhang T, Wilkinson A J, Dunin-Borkowski R E, Lekka C E and Grobert N 2013 Controlling the orientation, edge geometry, and thickness of chemical vapor deposition graphene *ACS Nano.* **7** 1351–9

[24] Zhang B, Lee W H, Piner R, Kholmanov I, Wu Y, Li H, Ji H and Ruoff R S 2012 Low-temperature chemical vapor deposition growth of graphene from toluene on electroplished copper foils *ACS Nano.* **6** 2471–6

[25] Mohsin A *et al* 2013 Synthesis of millimeter-size hexagon-shaped graphene single crystals on resolidified copper *ACS Nano.* **7** 8924–31

[26] Kim S M, Hsu A, Lee Y-H, Dresselhaus M, Palacios T, Kim K K and Kong J 2013 The effect of copper pre-cleaning on graphene synthesis *Nanotechnology* **24** 365602

[27] Diebel J, Hove H and Rabe J P 2001 Fabrication of large-scale ultra-smooth metal surfaces by replica technique *Appl. Phys.* A **73** 273–9

[28] Ragan R, Ohlberg D, Blackstock J J, Kim S and Williams R S 2004 Atomic surface structure of UHV-prepared template-stripped platinum and single-crystal platinum(111) *J. Phys. Chem.* B **108** 20187–92

[29] Weiss E A, Kaufman G K, Kriebel J K, Li Z, Schalek R and Whitesides G M 2007 Si/SiO_2-templated formation of ultraflat metal surfaces on glass, polymer and solder supports: their use as substrates for self-assembled monolayers *Langmuir* **23** 9686–94

[30] Šikola T *et al* 1999 Deposition of magnetic thin films by IBAD *Nucl. Instrum. Methods Phys. Res. Sect.* B **148** 907–11

[31] Rafaja D, Valvoda V, Šikola T and Spousta J 1998 *Ab initio* study of thin metallic and ceramic films *Thin Solid Films* **324** 198–208

[32] Celebi K, Cole M T, Choi J W, Wyczisk F, Legagneux P, Rupesinghe N, Robertson J, Teo K B K and Park H G 2013 Evolutionary kinetics of graphene formation on copper *Nano. Lett.* **13** 967–74

[33] Sarajlic O I and Mani R G 2013 Mesoscale scanning electron and tunneling microscopy study of the surface morphology of thermally annealed copper foils for graphene growth *Chem. Mater.* **25** 1643–8

[34] Zhang X, Xu Z, Hui L, Xin J and Ding F 2013 How the orientation of graphene is determined during chemical vapor deposition growth *J. Phys. Chem. Lett.* **3** 2822–2827

[35] Meng L, Wang Z, Jiang J, Yang Y and Wang J 2013 Defect healing of chemical vapor deposition graphene growth by metal substrate step *J. Phys. Chem.* C **117** 15260

[36] Du X, Skachko I, Barker A and Andrei E Y 2008 Approaching ballistic transport in suspended graphene *Nature Nanotechnol.* **3** 491–5

[37] Piner R *et al* 2013 Graphene synthesis via magnetic inductive heating of copper substrates *ACS Nano.* **7** 7495–9

[38] Batzill M 2012 The surface science of graphene: metal interfaces, CVD synthesis, nanoribbons, chemical modifications, and defects *Surf. Sci. Rep.* **67** 83–115

[39] Ago H, Ito Y, Mizuta N, Yoshida K, Hu B, Orofeo C M, Tsuji M, Ikeda K and Mizuno S 2010 Epitaxial chemical vapor deposition growth of single layer graphene over cobalt film crystallized on sapphire *ACS Nano.* **4** 7407–14

[40] Sutter P W, Albrecht P M and Sutter E A 2010 Graphene growth on epitaxial Ru thin films on sapphire *Appl. Phys. Lett.* **97** 213101

[41] Vo-Van C, Kimouche A, Reserbat-Plantey A, Fruchart O, Bayle-Guillemaud P, Bendiab N and Coraux J 2011 Epitaxial graphene prepared by chemical vapor deposition on single crystal thin iridium films on sapphire *Appl. Phys. Lett.* **98** 181903

[42] Hu B, Ago H, Ito Y, Kawahara K, Tsuji M, Magome E, Sumitani K, Mizuta N, Ikeda K and Mizuno S 2012 Epitaxial growth of large-area single-layer graphene over Cu (111)/sapphire by atmospheric pressure CVD *Carbon* **50** 57–65

[43] Jacobberger R M and Arnold M S 2013 Graphene growth dynamics on epitaxial copper thin films *Chem. Mater.* **25** 871–7

2.1.2 Článek č. 2 - Mechanismus vzniku a potlačení hystereze v grafenovém FET senzoru způsobené fyzisorbovanou vodou

Autoři:

M. Bartošík, **J. Mach**, J. Piastek, D. Nezval, M. Konečný, V. Švarc, K. Ensslin a T. Šikola

ACS Sensors [online]. 2020, **5,** 2940-2949. Dostupné z: doi: 10.1021/acssensors.0c01441.

Abstrakt:

V tranzistorech řízených elektrickým polem (FET) představuje hystereze odporu grafenu problém, který je často způsoben defekty a zachytáváním náboje uvnitř izolační hradlové vrstvy (např. SiO_2). Tato práce ukazuje, že FET na bázi grafenu také vykazuje hysterezi kvůli fyzisorbované vodě na povrchu grafenu řízenou relativní vlhkostí, což přirozeně nastává v biosenzorech a senzorech pracujících v běžných atmosférických podmínkách. Vznik hystereze je v předloženém článku přisuzován záchytu elektronů fyzisorbovanou vodou. Ukazuje se, že tuto hysterezi lze potlačit pomocí krátkých střídavých napěťových pulzů přiváděných na hradlového napětí.

pubs.acs.org/acssensors Article

Mechanism and Suppression of Physisorbed-Water-Caused Hysteresis in Graphene FET Sensors

Miroslav Bartošík,* Jindřich Mach, Jakub Piastek, David Nezval, Martin Konečný, Vojtěch Švarc, Klaus Ensslin, and Tomáš Šikola

Cite This: ACS Sens. 2020, 5, 2940−2949

Read Online

ACCESS | Metrics & More | Article Recommendations

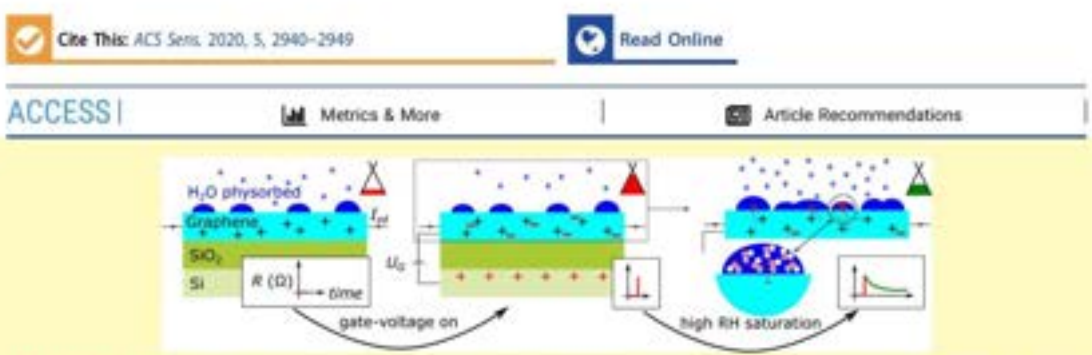

ABSTRACT: Hysteresis is a problem in field-effect transistors (FETs) often caused by defects and charge traps inside a gate isolating (e.g., SiO_2) layer. This work shows that graphene-based FETs also exhibit hysteresis due to water physisorbed on top of graphene determined by the relative humidity level, which naturally happens in biosensors and ambient operating sensors. The hysteresis effect is explained by trapping of electrons by physisorbed water, and it is shown that this hysteresis can be suppressed using short pulses of alternating gate voltages.

KEYWORDS: *graphene, sensor, relative humidity, water, hysteresis, gate voltage, physisorption*

Downloaded via BRNO UNIV OF TECHNOLOGY on March 26, 2021 at 08:25:56 (UTC).
See https://pubs.acs.org/sharingguidelines for options on how to legitimately share published articles.

Graphene, a single layer of carbon atoms arranged into a hexagonal structure, is a suitable material for electronic sensors working on the principle of resistivity changes caused by adsorbed molecules acting as acceptors or donors. It has been shown that in vacuum a graphene-based sensor can detect even single gas molecules.[1] This extremely high sensitivity results from the fact that every graphene atom is a surface atom itself and can directly interact with adsorbed particles. Moreover, due to graphene's biocompatibility and ability to be easily functionalized, it can be advantageously used in biosensors operating in air or even in a water solution. Here, in addition to detected molecules, graphene is exposed to water molecules influencing real sensor behavior.[2]

The specific species are usually sensed by graphene sensors (biosensors) having a field-effect transistor (FET) arrangement. The main characteristic for the detection of these species is the dependence of resistivity on back gate voltage (back gate trace) exhibiting a peak corresponding to the charge neutrality point (CNP peak). This point is defined by the Fermi level crossing the Dirac point, where the total charge in graphene should be zero. Ideally, in the case of sensors, the shift of the CNP peak is determined by doping caused by adsorbed molecules being detected. However, the real graphene sensors of a FET's design generally exhibit hysteresis in atmospheric and water solution conditions, consisting in different positions of the CNP peak during upward and downward back gate voltage sweeping. Such a behavior is often attributed to charge trapping and diffusion inside a gate isolating layer (e.g., ion diffusion, negative/positive bias temperature instability).[3−14] This behavior causes ambiguity in the determination of the graphene doping level and the corresponding amount of detected molecules.

In this work, we show that hysteresis in a graphene FET sensor is also caused by water molecules adhered by physisorption. The water origin of this hysteresis is proved by measurements at different relative humidities, under atmospheric conditions and in a vacuum environment caused by water molecules only. Furthermore, it is shown that the hysteresis can be suppressed by the utilization of alternating short gate voltage pulses. Finally, a fundamental mechanism of electron trapping by physisorbed water explaining the hysteresis behavior is proposed.

Received: July 13, 2020
Accepted: September 2, 2020
Published: September 2, 2020

© 2020 American Chemical Society

https://dx.doi.org/10.1021/acssensors.0c01441
ACS Sens. 2020, 5, 2940−2949

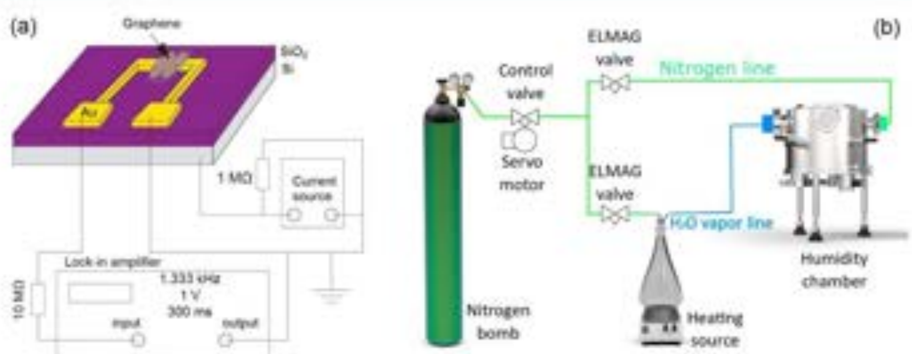

Figure 1. (a) Schematic of the sensor electronic setup for transport measurements. (b) Environmental chamber for controlling the relative humidity.

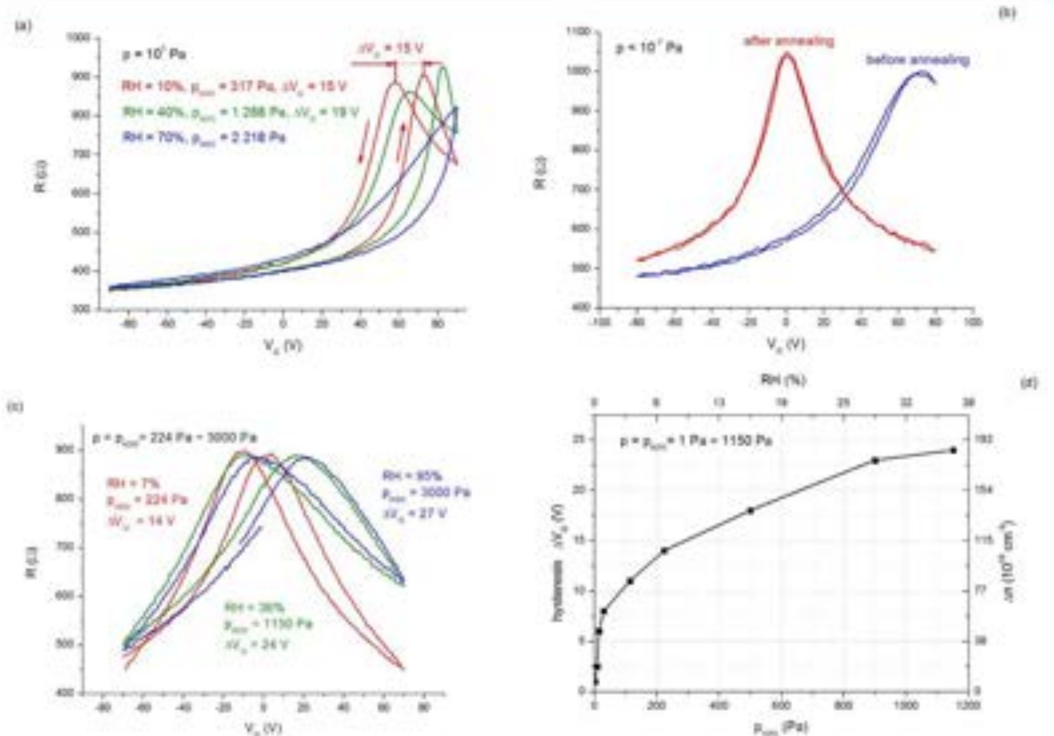

Figure 2. Evolution of hysteresis during the measurement of graphene resistance as a function of back gate voltage: (a) in atmospheric conditions at three different RH values, (b) in UHV before and after annealing (no hysteresis), and (c) in low vacuum at three different water vapor pressures (after introducing water vapors into a UHV chamber). (d) Hysteresis as a function of the pressure of water vapor introduced into a vacuum chamber.

■ METHODS

A large-area polycrystalline graphene layer was grown by a standard low-pressure chemical vapor deposition (CVD) method.[15] To get a high-quality graphene layer, an ultrasmooth copper foil was used for graphene growth.[16−18] The growth procedure consisted of three technology steps: (1) copper annealing at a hydrogen flow (4 sccm, 10 Pa, 1000 °C, 30 min) to remove air adsorbates, (2) methane introduction (40 sccm, 70 Pa, 1000 °C, 30 min) to grow graphene in a H_2/CH_4 mixture, and (3) bottom-side copper cleaning in oxygen−argon plasma (20% O_2, 80% Ar, 2 min) to remove graphene from this side, while that one from the top side was protected from plasma etching by a spin-coated poly(methyl methacrylate) (PMMA) layer.

The transfer process was performed by a PMMA-assisted wet transfer method. Graphene was transferred on a p-doped silicon substrate (resistivity 1.0×10^{-3}–1.5×10^{-3} Ω·cm) covered by thermal 280 nm SiO_2 and two lithographically prefabricated Au(45 nm)/Ti (3 nm) electrodes. The active part of graphene between these

https://dx.doi.org/10.1021/acssensors.0c01441
ACS Sens. 2020, 5, 2940−2949

electrodes then determines the geometry of the measured graphene channel with length $L = 50$ μm and width $W = 400$ μm.

The sample is arranged in the form of a field-effect transistor (FET) with a bottom gate electrode to provide back gate voltage sweeping (Figure 1a). The application of back gate voltage (V_G) controls the charge carrier density according to the formula $n = (\varepsilon_0\varepsilon_r/ed)V_G$, where ε_0 is the vacuum permittivity, ε_r is the SiO_2 relative permittivity (3.9), e is the elementary charge, and d is the thickness of the SiO_2 layer. The graphene resistivity is then defined as $\rho = RW/L$, and its dependence on V_G determines the doping type and charge carrier mobility. The resistance (R) of the graphene layer was measured using a lock-in amplifier SR830 (Stanford Research Systems) with a frequency of 1333 Hz, a fixed current of 100 nA, and a back gate voltage in the range of ±90 V.

All transport experiments were measured in situ at the controlled relative humidity (RH) and room temperature of 25 °C (RT). The experiments were carried out either in a home-built stainless steel environmental chamber (Figure 2b) under ambient conditions at atmospheric pressure (10^5 Pa) or in another home-built ultrahigh vacuum (UHV) chamber providing low base pressure (4×10^{-7} Pa) that was increased only by introducing water vapors up to 3000 Pa (corresponding to 95% RH). Nitrogen gas or a water vapor−nitrogen mixture can be flowed through the environmental chamber to reduce or increase the RH in the chamber, respectively.[19] In the UHV chamber, the total pressure is controlled by the evaporation of water from a flask in vacuum.

EXPERIMENTAL RESULTS

Back Gate Trace in Vacuum and Atmosphere at Different RH Values. A typical back gate trace experiment in atmospheric conditions is depicted in Figure 2a. Here, the gate voltage was continuously swept from 0 to 90 V, from 90 to −90 V, and finally from −90 to 0 V. The voltage incremental change during one step was 1 V, and its duration was 0.6 V/s. The measurement was performed at three values of relative humidity: 10, 40, and 70%. Obviously, there are two distinct ways of behavior. First, the curves move toward positive voltages with the relative humidity that corresponds to a stronger p-doping of graphene. Second, the individual curves for each RH do not overlap and exhibit strong hysteresis. For lower RH values of 10 and 40%, the hysteresis can be quantified by a voltage shift (ΔV_G) of the CNP peak, which was 15 and 19 V, respectively. For a higher RH of 70%, the voltage shift parameter cannot be determined due to a strong p-doping, moving the CNP peak out of the measured range. However, even here, a strong hysteresis is present. Generally, the hysteresis causes that the CNP peak is moved to higher gate voltages for increasing gate voltage and to lower gate voltages for decreasing gate voltage during one cycle of back gate trace.

The hysteresis in the measurement leads to ambiguity in the determination of the CNP peak position and consequently influences the calculation of the charge carrier concentration. This ambiguity is possible to quantify. For example, in the case of a back gate trace for 10% RH (red curve in Figure 2a), the right CNP peak occurs at a gate voltage of 74 V and the left peak at 59 V, which corresponds to the mentioned 15 V voltage shift. It results in a charge carrier concentration of 5.7×10^{12} cm^{-2} for the right CNP peak position and 4.54×10^{12} cm^{-2} for the left CNP peak. Therefore, the absolute ambiguity (error) in the determination of the charge carrier concentration is 1.16×10^{12} cm^{-2} and the corresponding relative error in finding this concentration with respect to the mean value is almost 23% (1.16/(5.70 + 4.54)/2). This is quite high value as the changes in the CNP peak position caused by the detected substance in a typical sensor or biosensor are often much smaller.[20−26]

The hysteresis disappeared when the sample was put into the UHV chamber and the pressure was pumped down to 10^{-7} Pa, as can be seen in Figure 2b (blue curve). Furthermore, after annealing at a temperature of 300 °C for 1 h, the CNP peak was shifted from 72 to 1 V (red curve), and the sample again revealed no hysteresis. It leads to the following conclusions. First, the removal of atmospheric molecules in space surrounding the sample eliminated the hysteresis. Second, annealing, which generally removes surface contaminants, adsorbed water molecules, and even water captured under graphene (at the silica−graphene interface),[27] changed the strongly p-doped graphene to intrinsic graphene.

To distinguish between the influences of water and other atmospheric molecules (oxygen, nitrogen, etc.), the annealed sample was exposed in the UHV vacuum chamber to water molecules only, as shown in Figure 2c. Introducing water vapors into the chamber up to the pressure of 3000 Pa (the partial pressure of water molecules is here also an absolute pressure) resulted in the restoration of hysteresis behavior. The voltage shift (ΔV_G) parameters characterizing the hysteresis rate were 14, 24, and 27 for water vapor pressures of 224, 1150, and 3000 Pa, respectively. It corresponds to relative humidity values of 7, 36, and 95%. It means that the hysteresis increased with the amount of water vapor. A more detailed measurement in the relative humidity range from 0 to 36% RH (Figure 2d) showed a gradual exponential saturation of hysteresis development with water vapor pressure ($\approx 23.72 - 20.22 \cdot e^{-0.003p}$).

Comparing hysteresis using the back gate voltage shift (ΔV_G) for experiments performed in atmospheric (Figure 2a) and vacuum conditions (Figure 2c), it is obvious that the hysteresis has very similar values for comparable RH values. On the other hand, the average p-doping shift of CNP (calculated from the corresponding left and right peaks in Figure 2c) was close to zero in vacuum (less than 9 V) even after introducing water vapors. From this point of view, the rate of hysteresis in the experiment is related to the level of water vapors present in the sensor's surroundings. However, the overall graphene p-doping relates to ambient conditions since the average p-doping of graphene is recovered after a day of ambient atmosphere exposure. Furthermore (see below discussion), these experimental results will be explained as a consequence of different behaviors of water above and under graphene with RH.

Although the presented experiments performed in vacuum conditions introduced the behavior of the graphene FET sensor exposed to water molecules only, most of the recent biosensors operate in real atmospheric conditions in the presence of all other atmospheric molecules and at the standard pressure. Below, we will focus on sensor behavior in an atmosphere in more detail.

Sensor Response to an Individual Back Gate Voltage Step. Since a typical back gate trace measurement consists of continual gradual changes in back gate voltage, it is fundamental to understand the sensor response on an individual back gate voltage step applied under atmospheric conditions at different RH values. Such a measurement is shown in Figure 3. Here, a single 70 V back gate voltage step was applied at the 100 s time after the beginning of the transport measurement and then the resistance response was observed for the next 160 min. According to practice in sensing experiments,[1,28−31] the relative change of resistance is depicted in Figure 3 instead of the absolute change of resistance. The relative change of

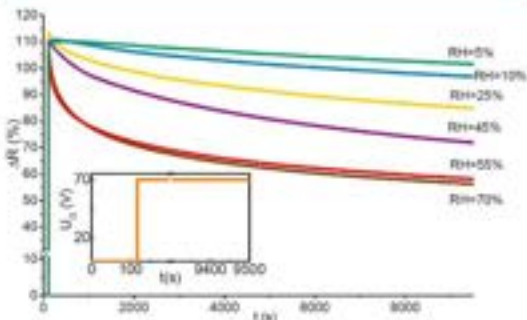

Figure 3. Relative change of sensor resistivity caused by the application of a gate voltage step at the 100 s time from the start of the experiment (see the inset) and its time evolution in the next 160 min under atmospheric conditions for different RH values.

https://dx.doi.org/10.1021/acssensors.0c01441
ACS Sens. 2020, 5, 2940−2949

resistance is defined as $\Delta R = (R(t) - R_0)/R_0$, where $R(t)$ is the resistance measured in time t and R_0 is the initial resistance.

The back gate voltage step results in a big and sudden change in the relative resistance (Figure 3, initial part). This change approaches a value of 110% independent of the relative humidity and is caused by a compensation of the originally p-doped graphene (Figure 2b, blue curve) by the influx of electrons. After the application of gate voltage, a gradual exponential decrease of relative resistance was observed with time (Figure 3, following part). The decay was faster for higher RH values. While for 5% RH (green curve), the resistance remained almost the same (from $\Delta R = 110\%$ to $\Delta R = 102\%$), for 70% RH (brown curve), the relative resistance change decreases to 55% (from $\Delta R = 110\%$ to $\Delta R = 55\%$). Although this exponential decrease occurs within a relatively long time (160 min), it represents one of the main reasons for hysteresis in atmospheric back gate trace measurements (Figure 2a). This is supported by the fact that all of the time during the back gate trace measurements (Figure 2a,c), the resistance also exponentially decreases (Figure 3), while the gate voltage is continually changed.

Sensor Response to a Back Gate Voltage of Different Sizes in UHV and Atmospheric Conditions. The necessity of water vapor presence for the existence of hysteresis in the ambient atmosphere was indirectly confirmed by measurements in UHV (Figure 4), where two gate voltage steps of 28 and 70 V were applied.

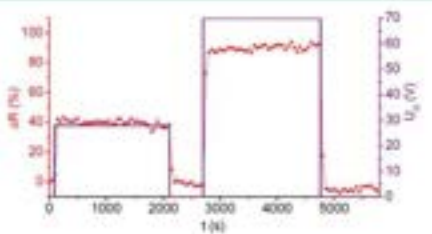

Figure 4. Relative change of sensor resistivity after the application of two gate voltage steps of 28 V (electric field intensity in SiO_2, 1 MV/cm) and 70 V (2.5 MV/cm) and its time evolution in UHV conditions before annealing.

Here, no exponential decrease after switching on the gate voltage was observed, which corresponded to the fact that the back gate trace experiment did not exhibit any hysteresis in UHV (Figure 2b).

The applied back gate voltages of 28 and 70 V resulted in two different electric fields in the SiO_2 layer equal to 1 and 2.5 MV/cm, respectively. Consequently, the lower 28 V gate voltage step caused the lower resistance change $\Delta R = 40\%$ than the bigger 70 V gate voltage step, which led to $\Delta R = 90\%$ (Figure 4). The exponential decay is not present in UHV (Figure 4). If these voltages are applied in atmospheric conditions, an exponential decay appears, which is for the lower gate voltage slower in time than for the higher gate voltage (Figure 5a). Here, the relative change of resistance related to the initial maximum R_{max} obtained after the application of the corresponding gate voltage is defined as $\Delta R_{max} = (R(t) - R_{max})/R_{max}$.

The exponential decays depicted in Figures 3 and 5 asymptotically approach a certain saturation value of resistance response. The higher the applied gate voltage and relative humidity, the faster and larger the saturation process. The hypothesis explaining this behavior will be presented in more detail in the Discussion section.

Sensor Response to an Individual Relative Humidity Step. To better understand the resistivity saturation process, the sensor resistance response to a change of relative humidity at the zero gate voltage application was studied. As can be seen in Figure 6, the

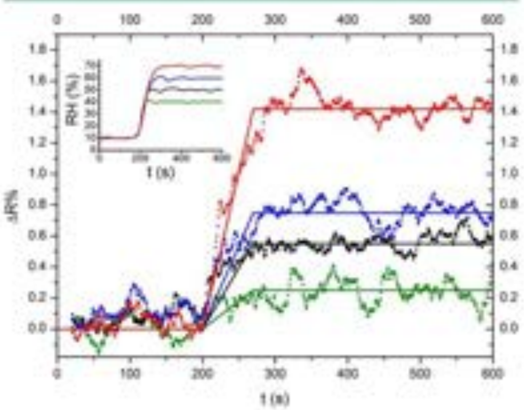

Figure 6. Time development of the relative change of sensor resistivity after the application of four different steplike upturns (inset) of relative humidity at time 200 s: 10 → 40% (green), 10 → 50% (black), 10 → 60% (blue), and 10 → 70% (red).

response is relatively small (<1.6% relative resistance change) and has a relatively long duration (~50 s). Such a small response can be explained by the CNP peak-offset position of the nonannealed graphene utilized in this study, which was higher than 40 V (Figure

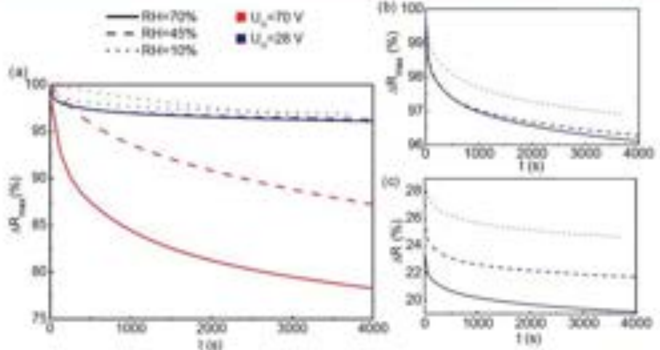

Figure 5. (a) Relative change of sensor resistivity after the application of two gate voltage steps of 28 and 70 V and its time evolution in atmospheric conditions at relative humidities of 10, 45, and 70%. Details of the resistivity relative change for the gate voltage of 28 V related to (b) an initial resistance maximum and (c) initial resistance.

https://dx.doi.org/10.1021/acssensors.0c01441
ACS Sens. 2020, 5, 2940−2949

2a,b, blue curve). Then, at the zero gate voltage application ($V_G = 0$ V), the resistance can change only slightly since the CNP peak is far away. This problem of small resistance response is usually resolved by setting a proper gate voltage, so that the slope of the resistance course in the back gate voltage trace reaches its highest value—the point of maximum transconductance.[21,31] Nevertheless, in our case, such a setting was not possible due to the mentioned process of saturation, while a gate voltage is applied for a longer time. Therefore, in this article, we suggest a different solution presented in the Experimental Solution of the Hysteresis Problem section.

Common Influence of Back Gate Voltage and Relative Humidity. In this section, the response of a graphene FET sensor to steplike relative humidity changes for different gate voltages will be discussed. Such a testing regime is often similar to a working regime of graphene sensors in real operation conditions.[33−36] In Figure 7, the response of the graphene sensor to two relative humidity steps (RH = 10 → 70 → 10 → 70 → 10%) for three different gate voltages of −70, 0, and +70 V is shown. In the case of zero gate voltage, a small resistance response to humidity steps is seen, which is in agreement with our previous measurements (Figure 6, red curve). On the other hand, the reaction to humidity steps is much stronger for the gate voltages of −70 and +70 V (Figure 7, green and red). The charts show the following behavior. First, after the application of these initial gate voltages, the resistance change was swiftly increased and then a long exponential course followed by a saturation occurs. This typical time development was interrupted when a high relative humidity (70%) was applied. In the case of the positive gate voltage application (+70 V, Figure 7, red curve), there is a significant initial positive increase of resistance followed by a lengthy exponential decay, which considerably speeds up during the first humidity step; meanwhile, during the application of the second humidity step, the response is already weak and similar to the zero gate one (black curve). In the case of a negative gate voltage application (−70 V), there is a low initial decrease of resistance followed again by an exponential time development which is increasing in this case. Moreover, the increase is enhanced and accelerated in time of higher humidity steps. The response to the positive gate voltage is in agreement with the previous experiments (Figure 3); however, the response to the negative gate voltage is quite opposite—an initial decrease followed by exponential growth. The lower absolute initial change of resistance and its opposite character can be explained by the asymmetry of the back gate trace curves (Figure 2b, blue curve) since at the application of a negative voltage the resistance decreases and its absolute change is much smaller than that for the positive gate voltage. Both evolutions for positive and negative gates prove the exponential tendency of returning to certain saturated values. Simultaneously, an increase of relative humidity accelerates the process of aiming toward a saturation state. This time evolution process turned on by the gate voltage application is in competition with a small step change of resistivity caused by a change of relative humidity. During the first humidity step (Figure 7), the domination of the returning process is evident; however, in the second step, the real response on humidity prevails. The chart in Figure 7 illustrates how the behavior of sensors can appear complex in a real experiment held in the atmosphere, although it is relatively easy to explain as the interplay of the previously described three partial effects: (1) response to RH, (2) response to gate steps, and (3) motion toward saturation.

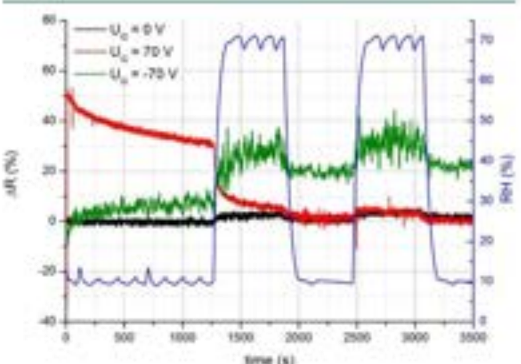

Figure 7. Complex sensor behavior. Relative change of sensor resistivity after the application of two relative humidity steps (10% for 1250 s → 70% for 750 s → 10% for 500 s → 70% for 750 s) at three different gate voltages of 0, +70, and −70 V.

EXPERIMENTAL SOLUTION OF THE HYSTERESIS PROBLEM

The previous experiments have led to the following important results: The response of the sensor to an application of gate voltage in a typical range −90 to +90 V is much stronger than that one to the relative humidity change ranging from 10 to 70%. Moreover, after the gate voltage application, the lengthy process of saturation occurs. However, in common continual back gate trace measurements, an almost immediate change of resistance caused by an applied voltage is required, as the process of the long-lasting saturation (exponential course) brings a side effect of hysteresis into the measurement. With respect to that, it is reasonable to ask how to experimentally resolve the problem of hysteresis and corresponding ambiguity for sensors operating in the atmosphere. This implies a specific question, what is the shortest necessary time to get a full response of a sensor to an application of gate voltage, which would not be significantly distorted by the later saturation process?

To answer this question, an experiment recording the resistance response to gate voltage pulses in small time steps was performed (Figure 8a,c). The resistance response to a gate voltage pulse depicted in Figure 8b is shown in Figure 8d. Here, the resistance was measured in 0.2 s steps after gate voltage switching. The resistance response achieved its full value approximately 2.4 s after the gate voltage application (Figure 8b) and was not affected by the exponential decay within the time interval between 2.4 and 5 s, as depicted in Figure 3.

The problem of the classical back gate trace hysteresis lies in the long time period for which nonzero voltage is applied without interruption and for which the sensor tends to saturate. For example, the positive part of the classical back gate trace from 0 to 90 V and backward takes almost 2 min (180 steps × 0.6 s/step = 1 min 48 s). In comparison with that, the measurement applying the alternating gate voltage eliminates the active time of measurement to 5 s.

To resolve the problem of hysteresis during sensing via back gate voltage tracing, a series of short gate voltage pulses and corresponding resistance responses can be utilized (Figure 8). Such a measurement is free from hysteresis; however, it includes fewer data points than a classical continual back gate trace measurement at the same time due to switching between time-separated discrete back gate voltage pulses. Figure 8a represents the individual measurement cycle composed of 18 gate voltage pulses delayed by one minute.

The experiment comparing a classical continual back gate trace measurement and the modified methodology utilizing alternating gate voltage pulses at three different levels of relative humidity, 40, 70, and 10%, is shown in Figure 9.

Figure 9a,b shows the measurement performed by a standard continual back gate voltage trace. Here, by increasing the back gate voltage, the CNP shifts to the right (more positive gate voltages), and by decreasing the back gate voltage, it shifts to the left. On can see this hysteresis behavior in Figure 9b as an oscillation of the maximum resistance (CNP) point in time depending on the direction of back gate voltage changes.

The results achieved by the application of alternating gate voltage pulses are depicted in Figure 9c,d. Here, the sequence of gate voltages 0 → 10 → 0 → −10 → ... → 80 → 0 → −80 → 0 → 90 → 0 → −90 V was applied (see the inset of Figure 9c). The nonzero value of the back gate voltage was kept for 5 s, while the zero back gate voltage was applied for the rest 55 s to recover the sample from the previously

https://dx.doi.org/10.1021/acssensors.0c01441
ACS Sens. 2020, 5, 2940−2948

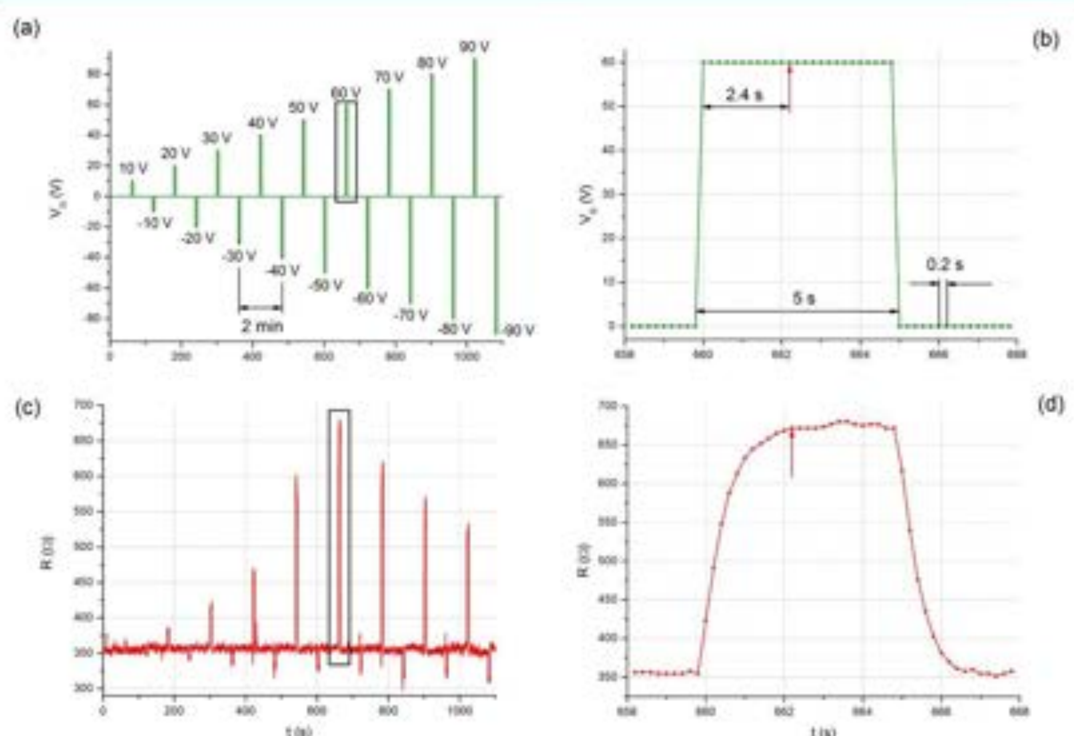

Figure 8. Procedure of a modified back gate trace measurement. (a) Applying a series of alternating gate voltage pulses (each of them lasting for the short time of 5 s) to eliminate the hysteresis effects caused by the exponential saturation time development, (b) details of a positive back gate voltage pulse in one measurement cycle marked in (a) by the black rectangle, (c) resistance response to the series of pulses shown in (a), and (d) details of the resistance response marked in (c) by the black rectangle to the individual gate voltage pulse depicted in (b).

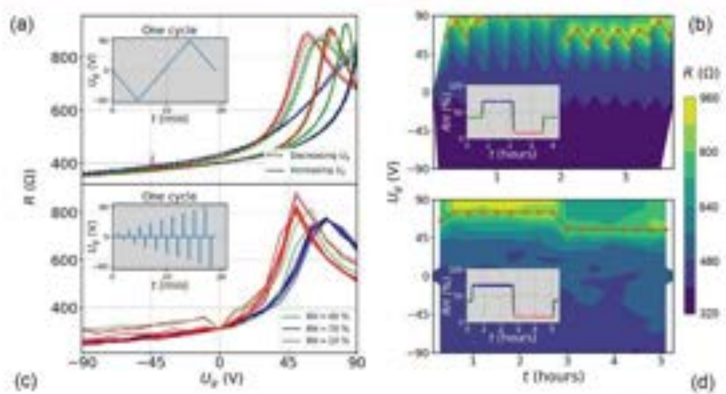

Figure 9. Back gate voltage trace experiment using (a, b) the standard continual procedure (see the inset in (a)) and (c, d) improved method based on alternating back gate voltage pulses (see the inset in (c)) at three relative humidity values of 40, 70, and 10% (see the insets in (b, d)). The positions of maximum resistance (mostly equal to CNP) highlighted by red dots indicate the presence of hysteresis in the case of the standard continual procedure (b) and the absence of hysteresis in the case of the improved method (d).

gate voltage application. The value of resistance was read 2.4 s after the application of the nonzero gate voltage. In measurements done in this way, the hysteresis behavior (the difference between CNP peak positions for increasing and decreasing gate voltages) did not occur (Figure 9c,d), while in the continual back gate trace, the hysteresis was present (Figure 9a,b). At the high relative humidity of 70%, the CNP peak was 80 V (Figure 9c, blue curve), for the low RH = 10%, the CNP peak was 60 V (red curve), and for the middle-level RH = 40%, it was 70 V. Contrary to the standard back gate voltage trace, there is no CNP oscillation and the sensor reacted on the level of RH only. Hence, the utilization of the alternating back gate trace solves the problem of hysteresis by minimization of the time of gate voltage

$$E_F = sgn(n_{Gr})\hbar v_F\sqrt{\pi|n_{Gr}|} \quad (2)$$

Here, $\hbar$ is the reduced Planck constant and v_F is the Fermi velocity of electrons in graphene. The total concentration (n) of electrons, given by the concentration of mobile electrons in graphene (n_{Gr}) and concentration of immobile electrons trapped in physisorbed water on graphene (n_{H_2O}), is proportional to the back gate voltage

$$n = n_{Gr} + n_{H_2O} = \alpha \cdot V_G \quad (3)$$

The current is determined only by electrons remaining in graphene—see eqs 1 and 2. The resultant concentration of these electrons (n_{Gr}) depends on the effectivity of the trapping and diffusion of electrons inside the physisorbed water, which is a lengthy process and takes much time than fast electronic gate switching.

In the proposed model, three different processes can be distinguished according to their speed. First, the fast delivery of electrons into graphene after the application of back gate voltage, taking up to 5 s (Figure 8). Second, the medium-fast process of changing physisorbed water coverage after changing the relative humidity, taking up to 1 min, which was observed by Hong et al.[37] Finally, the slow process of gradual charging of physisorbed water by electrons from graphene and their diffusion into the physisorbed water, taking several minutes and more (Figures 3 and 5).

In the presented explanation, the main responsibility for the hysteresis is carried out by the physisorbed water above graphene whose amount can be easily changed by the relative humidity. On the other hand, part of the physisorbed water is also present under graphene at the silica–graphene interface. However, this water is firmly captured by graphene, which is water-impermeable.[39] The only way through which water can penetrate under graphene is through the edges. This process is however extremely slow and takes days (from 26 h to 70 days) even in the case of a few-micrometer graphene flake on silica completely submerged in water, as proved by Lee et al.[27] However, the onset of hysteresis, when the relative humidity is increased, is almost immediate (Figure 2c). Therefore, we assume that the water under graphene is responsible for overall original p-doping (Figure 2c, blue curve), and after its removal by annealing in vacuum,[27] the sample is almost undoped (Figure 2c, red curve), while the physisorbed water on graphene easily controlled by the RH level is responsible for the occurrence of hysteresis (Figure 2d).

■ CONCLUSIONS

The ambient transport experiments showed the hysteresis behavior of graphene sensors in a FET configuration increasing with relative humidity and its complete elimination in UHV conditions. The origin of this hysteresis was attributed to the slow trapping of graphene electrons by water physisorbed on graphene, the amount of which is controlled by the relative humidity. It is demonstrated that this problem can be resolved by the application of short alternating gate voltage pulses during back gate trace measurements, allowing the fast electronic processes in graphene and suppressing the slow processes as electron trapping and their diffusion in water. In FET transistors, protection cover layers of graphene can effectively eliminate the problem of hysteresis. However, in the case of FET-based sensors and biosensors, where graphene has to be exposed to ambient and water conditions, the principle and method proposed in this article should be of assistance in understanding and suppression of the hysteresis effect.

■ AUTHOR INFORMATION

Corresponding Author

Miroslav Bartošík – *Central European Institute of Technology - Brno University of Technology (CEITEC BUT), 612 00 Brno, Czech Republic; Institute of Physical Engineering, Brno University of Technology, 616 69 Brno, Czech Republic; Department of Physics and Materials Engineering, Faculty of Technology, Tomas Bata University in Zlín, 760 01, Czech Republic;* orcid.org/0000-0003-4706-9112; Email: bartosik@fme.vutbr.cz

Authors

Jindřich Mach – *Central European Institute of Technology - Brno University of Technology (CEITEC BUT), 612 00 Brno, Czech Republic; Institute of Physical Engineering, Brno University of Technology, 616 69 Brno, Czech Republic;* orcid.org/0000-0003-1896-0715

Jakub Piastek – *Central European Institute of Technology - Brno University of Technology (CEITEC BUT), 612 00 Brno, Czech Republic; Institute of Physical Engineering, Brno University of Technology, 616 69 Brno, Czech Republic*

David Nezval – *Institute of Physical Engineering, Brno University of Technology, 616 69 Brno, Czech Republic*

Martin Konečný – *Institute of Physical Engineering, Brno University of Technology, 616 69 Brno, Czech Republic*

Vojtěch Švarc – *Central European Institute of Technology - Brno University of Technology (CEITEC BUT), 612 00 Brno, Czech Republic; Institute of Physical Engineering, Brno University of Technology, 616 69 Brno, Czech Republic*

Klaus Ensslin – *Solid State Physics Laboratory, ETH Zürich, CH 8093 Zürich, Switzerland*

Tomáš Šikola – *Central European Institute of Technology - Brno University of Technology (CEITEC BUT), 612 00 Brno, Czech Republic; Institute of Physical Engineering, Brno University of Technology, 616 69 Brno, Czech Republic*

Complete contact information is available at:
https://pubs.acs.org/10.1021/acssensors.0c01441

Notes

The authors declare no competing financial interest.

■ ACKNOWLEDGMENTS

The authors acknowledge the support by the Grant Agency of the Czech Republic (Grant No. 17-21413S), the H2020 Twinning Programme (Project SINNCE, 810626), and MEYS CR (Project No. LQ1601—CEITEC 2020). We also acknowledge the CEITEC Nano Research Infrastructure supported by MEYS CR within the Project LM2015041 for providing us with access to their facilities and Miroslav Kolíbal for reading this manuscript.

■ REFERENCES

(1) Schedin, F.; Geim, A. K.; Morozov, S. V.; Hill, E. W.; Blake, P.; Katsnelson, M. I.; Novoselov, K. S. Detection of Individual Gas Molecules Adsorbed on Graphene. *Nat. Mater.* **2007**, *6*, 652–655.

(2) Peña-Bahamonde, J.; Nguyen, H. N.; Fanourakis, S. K.; Rodrigues, D. F. Recent Advances in Graphene-Based Biosensor Technology with Applications in Life Sciences. *J. Nanobiotechnol.* **2018**, *16*, No. 95.

(3) Cazalas, E.; Childres, I.; Majcher, A.; Chung, T.-F.; Chen, Y. P.; Jovanovic, I. Hysteretic Response of Chemical Vapor Deposition Graphene Field Effect Transistors on SiC Substrates. *Appl. Phys. Lett.* **2013**, *103*, No. 053123.

(4) Kalon, G.; Shin, Y. J.; Truong, V. G.; Kalitsov, A.; Yang, H. The Role of Charge Traps in Inducing Hysteresis: Capacitance−Voltage Measurements on Top Gated Bilayer Graphene. *Appl. Phys. Lett.* **2011**, *99*, No. 083109.

(5) Liao, Z.-M.; Yan, B.-H.; Zhou, Y.-B.; Yu, D.-P. Hysteresis Reversion in Graphene Field-Effect Transistors. *J. Chem. Phys.* **2010**, *133*, No. 044703.

(6) Joshi, P.; Romero, H. E.; Neal, A. T.; Toutam, V. K.; Tadigadapa, S. A. Intrinsic Doping and Gate Hysteresis in Graphene Field Effect Devices Fabricated On. *J. Phys.: Condens. Matter* **2010**, *22*, No. 335214.

(7) Kuhn, M.; Silversmith, D. J. Ionic Contamination and Transport of Mobile Ions in MOS Structures. *J. Electrochem. Soc.* **1971**, *118*, 966−970.

(8) Lafkioti, M.; Krauss, B.; Lohmann, T.; Zschieschang, U.; Klauk, H.; Klitzing, K.; Smet, J. H. Graphene on a Hydrophobic Substrate: Doping Reduction and Hysteresis Suppression under Ambient Conditions. *Nano Lett.* **2010**, *10*, 1149−1153.

(9) Levesque, P. L.; Sabri, S. S.; Aguirre, C. M.; Guillemette, J.; Siaj, M.; Desjardins, P.; Szkopek, T.; Martel, R. Probing Charge Transfer at Surface Using Graphene Transistors. *Nano Lett.* **2011**, *11*, 132−137.

(10) Shi, Y.; Fang, W.; Zhang, K.; Zhang, W.; Li, L. Photoelectrical Response in Single-Layer Graphene Transistors. *Small* **2009**, *5*, 2005−2011.

(11) Wang, H.; Wu, Y.; Cong, C.; Shang, J.; Yu, T. Hysteresis of Electronic Transport in Graphene Transistors. *ACS Nano* **2010**, *4*, 7221−7228.

(12) Xu, H.; Chen, Y.; Zhang, J.; Zhang, H. Investigating the Mechanism of Hysteresis Effect in Graphene Electrical Field Device Fabricated on SiO_2 Substrates Using Raman Spectroscopy. *Small* **2012**, *8*, 2833−2840.

(13) Krishnan, A. T.; et al. Negative Bias Temperature Instability Mechanism: The Role of Molecular Hydrogen. *Appl. Phys. Lett.* **2006**, *88*, No. 153518.

(14) Konečný, M.; Bartošík, M.; Mach, J.; Švarc, V.; Nezval, D.; Piastek, J.; Procházka, P.; Cahlík, A.; Šikola, T. Kelvin Probe Force Microscopy and Calculation of Charge Transport in a Graphene/Silicon Dioxide System at Different Relative Humidity. *ACS Appl. Mater. Interfaces* **2018**, *10*, 11987−11994.

(15) Li, X.; Cai, W.; An, J.; Kim, S.; Nah, J.; Yang, D.; Piner, R.; Velamakanni, A.; Jung, I.; Tutuc, E.; et al. Large Area Synthesis of High Quality and Uniform Graphene Films on Copper Foils. *Science* **2009**, *324*, 1312−1314.

(16) Procházka, P.; Mach, J.; Bischoff, D.; Lišková, Z.; Dvořák, P.; Vaňatka, M.; Simonet, P.; Varlet, A.; Hemzal, D.; Petrenec, M.; et al. Ultrasmooth Metallic Foils for Growth of High Quality Graphene by Chemical Vapor Deposition. *Nanotechnology* **2014**, *25*, No. 185601.

(17) Mach, J.; Procházka, P.; Bartošík, M.; Nezval, D.; Piastek, J.; Hulva, J.; Švarc, V.; Konečný, M.; Kormoš, L.; Šikola, T. Electronic Transport Properties of Graphene Doped by Gallium. *Nanotechnology* **2017**, *28*, No. 415203.

(18) Mach, J.; Šamořil, T.; Kolíbal, M.; Zlámal, J.; Voborny, S.; Bartošík, M.; Šikola, T. Optimization of Ion-Atomic Beam Source for Deposition of GaN Ultrathin Films. *Rev. Sci. Instrum.* **2014**, *85*, No. 083302.

(19) Bartošík, M.; Kormoš, L.; Flajšman, L.; Kalousek, R.; Mach, J.; Lišková, Z.; Nezval, D.; Švarc, V.; Šamořil, T.; Šikola, T. Nanometer-Sized Water Bridge and Pull-off Force in AFM at Different Relative Humidities: Reproducibility Measurement and Model Based on Surface Tension Change. *J. Phys. Chem. B* **2017**, *121*, 610−619.

(20) Ohno, Y.; Maehashi, K.; Yamashiro, Y.; Matsumoto, K. Electrolyte-Gated Graphene Field-Effect Transistors for Detecting PH and Protein Adsorption. *Nano Lett.* **2009**, *9*, 3318−3322.

(21) Fu, W.; Feng, L.; Panaitov, G.; Kireev, D.; Mayer, D.; Offenhäusser, A.; Krause, H. Biosensing near the Neutrality Point of Graphene. *Sci. Adv.* **2017**, *3*, No. e1701247.

(22) Vieira, N. C. S.; Borme, J.; Machado, G.; Cerqueira, F.; Freitas, P. P.; Zucolotto, V.; Peres, N. M. R.; Alpuim, P. Graphene Field-Effect Transistor Array with Integrated Electrolytic Gates Scaled To. *J. Phys.: Condens. Matter* **2016**, *28*, No. 085302.

(23) Fu, W.; Jiang, L.; van Geest, E. P.; Lima, L. M. C.; Schneider, G. F. Sensing at the Surface of Graphene Field-Effect Transistors. *Adv. Mater.* **2017**, *29*, No. 1603610.

(24) Cheng, Z.; Li, Q.; Li, Z.; Zhou, Q.; Fang, Y. Suspended Graphene Sensors with Improved Signal and Reduced Noise. *Nano Lett.* **2010**, *10*, 1864−1868.

(25) Ang, P. K.; Chen, W.; Wee, A. T. S.; Loh, K. P. Solution-Gated Epitaxial Graphene as PH Sensor. *J. Am. Chem. Soc.* **2008**, *130*, 14392−14393.

(26) Ohno, Y.; Maehashi, K.; Matsumoto, K. Label-Free Biosensors Based on Aptamer-Modified Graphene Field-Effect. *J. Am. Chem. Soc.* **2010**, *132*, 18012−18013.

(27) Lee, D.; Ahn, G.; Ryu, S. Two-Dimensional Water Diffusion at a Graphene−Silica Interface. *J. Am. Chem. Soc.* **2014**, *136*, 6634−6642.

(28) Hwang, S.; Lim, J.; Goo, H.; Kyun, W.; Kim, D.; Sang, I.; Hun, J.; Lee, S.; Ha, D.; Chan, S. Chemical Vapor Sensing Properties of Graphene Based on Geometrical Evaluation. *Curr. Appl. Phys.* **2012**, *12*, 1017−1022.

(29) Popov, V. I.; Nikolaev, D. V.; Timofeev, V. B.; Smagulova, S. A.; Antonova, I. V. Graphene-Based Humidity Sensors: The Origin of Alternating Resistance Change. *Nanotechnology* **2017**, *28*, No. 355501.

(30) Salehi-khojin, A.; Estrada, D.; Lin, K. Y.; Bae, M.; Xiong, F.; Pop, E.; Masel, R. I. Polycrystalline Graphene Ribbons as Chemiresistors. *Adv. Mater.* **2012**, *24*, 53−57.

(31) Dan, Y.; Lu, Y.; Kybert, N. J.; Luo, Z.; Johnson, A. T. C. Intrinsic Response of Graphene Vapor Sensors. *Nano Lett.* **2009**, *9*, 1472−1475.

(32) Dan, Y.; Lu, Y.; Kybert, N. J.; Luo, Z.; Johnson, A. T. C. Intrinsic Response of Graphene Vapor Sensors. *Nano Lett.* **2009**, *9*, 1472−1475.

(33) Choi, S.; Kim, S.; Kim, I. Ultrafast Optical Reduction of Graphene Oxide Sheets on Colorless Polyimide Film for Wearable Chemical Sensors. *NPG Asia Mater.* **2016**, *8*, No. e315.

(34) Zhang, J.; Liu, X.; Neri, G.; Pinna, N. Nanostructured Materials for Room-Temperature Gas Sensors. *Adv. Mater.* **2016**, *28*, 795−831.

(35) Huang, Y.; Huang, C.; Chen, Y.; Su, C.; Tsai, Y. Effect of Substrate Topography for Graphene-Based Humidity Sensors. *Jpn. J. Appl. Phys.* **2019**, *58*, No. SDDD04.

(36) Phan, D.; Park, I.; Park, A.; Park, C.; Jeon, K. Black P/Graphene Hybrid: A Fast Response Humidity Sensor with Good Reversibility and Stability. *Sci. Rep.* **2017**, *7*, No. 10561.

(37) Hong, G.; Han, Y.; Schutzius, T. M.; Wang, Y.; Pan, Y.; Hu, M.; Jie, J.; Sharma, C. S.; Mu, U.; Poulikakos, D. On the Mechanism of Hydrophilicity of Graphene. *Nano Lett.* **2016**, *16*, 4447−4453.

(38) Gaiduk, A. P.; Pham, T. A.; Govoni, M.; Paesani, F.; Galli, G. Electron Affinity of Liquid Water. *Nat. Commun.* **2018**, *9*, No. 247.

(39) Xu, K.; Cao, P.; Heath, J. R. Graphene Visualizes the First Water Adlayers on Mica at Ambient Conditions. *Science* **2010**, *329*, 1188−1191.

(40) Ma, T. P.; Dressendorfer, P. V. *Ionizing Radiation Effects in MOS Devices and Circuits*; Wiley: New York, 1989.

(41) Aitken, J. M.; Young, D. R.; Pan, K. Electron Trapping in Electron-Beam Irradiated SiO_2. *J. Appl. Phys.* **1978**, *49*, 3386−3391.

(42) Sethi, R. B.; Young, D. R.; Zook, J. D. Charge Trapping In Ion-Sputtered Silicon Dioxide Films On Silicon. *J. Electron. Mater.* **1990**, *19*, 231−234.

(43) DiMaria, D. J.; Cartier, E.; Arnold, D. Impact Ionization, Trap Creation, Degradation, and Breakdown in Silicon Dioxide Films on Silicon. *J. Appl. Phys.* **1993**, *73*, 3367−3384.

(44) Cho, B. J.; Chong, P. F.; Chor, E. F.; Joo, M. S.; Yeo, I. S.; Cho, B. J.; Chong, F.; Chor, E. F. Electron-Beam Irradiation-Induced Gate

Oxide Degradation Electron-Beam Irradiation-Induced Gate Oxide Degradation. *J. Appl. Phys.* **2000**, *88*, No. 6731.

(45) Tarrach, F.; Ch'hayder, A.; Guermazi, S. Charge Trapping and AC Conductivity in Amorphous Silicon Oxide. *Phys. Procedia* **2009**, *2*, 941−945.

(46) Li, H.; Liu, C.; Zhang, Y.; Qi, C.; Wei, Y.; et al. Electron Radiation Effects on the Structural and Electrical Properties of MoS_2 Field Effect Transistors. *Nanotechnology* **2019**, *30*, No. 485201.

https://dx.doi.org/10.1021/acssensors.0c01441
ACS Sens. 2020, 5, 2940−2949

3. Depozice z pevné fáze

Ultratenké vrstvy a nanostruktury lze také připravovat pomocí metod založených na fyzikálních principech označovaných jako depozice z pevné fáze (PVD - *Physical Vapour Deposition*). Mezi tyto procesy patří napařování a naprašování.

Tlak par z pevné (sublimace) nebo kapalné (vypařování) látky je funkcí teploty. V okamžiku, kdy se v komoře nachází látka v pevné nebo kapalné fázi v termodynamické rovnováze současně se svou plynnou fází, hovoříme o tlaku nasycených par. Stav rovnováhy je ustálen v okamžiku, kdy množství atomů přecházejících z pevné (kapalné) látky do plynného stavu se rovná stejnému množství kondenzujících atomů. To znamená, že rychlost vypařování a rychlost kondenzace látky je stejná. Takový stav může být realizován v Knudsenových napařovacích zdrojích. Napařování je prováděno ve vysokém (HV $p < 1\times10^{-5}$ Pa) a ultravysokém vakuu (UHV $p < 1\times10^{-7}$ Pa), čímž je do značné míry omezena negativní kontaminace připravovaných struktur vlivem dopadu částic zbytkových plynů. K tomuto účelu jsou navrhovány ultravakuové komory, které jsou vybavovány zdroji atomů, iontů, přístroji pro analýzu povrchů (například *Reflection High Energy Electron Diffraction*- RHEED) a systémy zajišťujícími jejich čerpání. Schéma typické UHV aparatury je zobrazeno na obrázku 6.

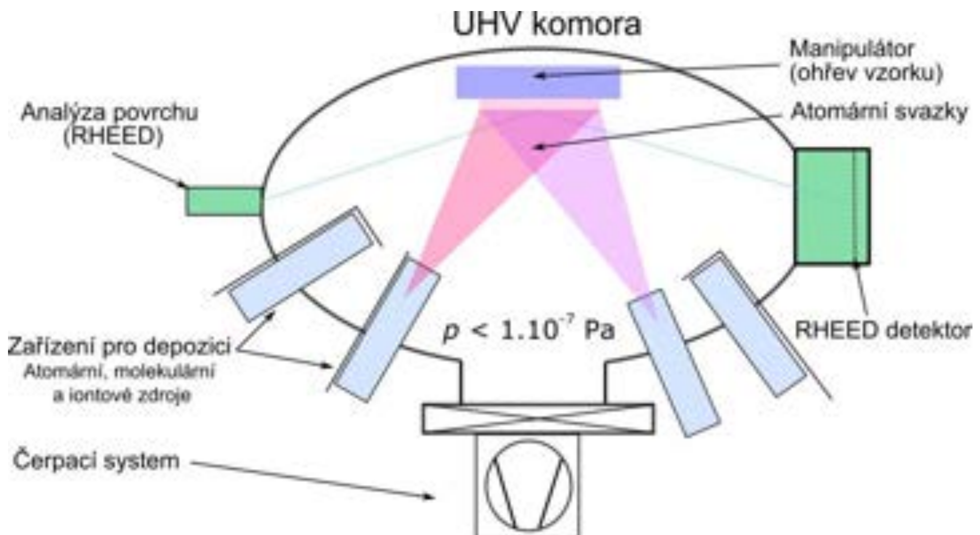

Obrázek 6: Schéma UHV aparatury pro přípravu ultratenkých vrstev a nanostrukturních materiálů.

Při návrhu zařízení určených do UHV prostředí je nutno dodržovat základní pravidla volby materiálů a konstrukčních řešení vycházející ze striktních požadavků na UHV prostředí. Proto se při volbě materiálů preferují ty, které mají nízký tlak nasycených par. Také povrchy součástí nesmí být výrazně pórovité a drsné, protože velký vnitřní povrch takové součásti by byl zdrojem nežádoucího plynění, které vede ke zhoršování vakua nad takovouto součástí. Při návrhu konstrukcí se musíme rovněž vyvarovat vzniku obtížně čerpatelných prostorů, jakým je například slepý závitový otvor se závitem a podobně. Samozřejmostí je dodržování čistoty při montáži a manipulaci se zařízením.

4. Zdroje atomů a molekul o termální energii

Pro přípravu ultratenkých vrstev a nanostruktur se často užívají v prostředí ultravysokého vakua (UHV – *Ultra-High Vacuum*) Knudsenovy cely, čili efuzní zdroje. Tyto zdroje atomů (molekul) využívají k formování atomárních či molekulárních svazků molekulárního toku. Základním charakteristickým prvkem zmíněných zařízení je zásobník obsahující materiál určený k depozici, který je pomocí zvýšené teploty převeden do plynného stavu (vypařování, sublimace). Z prováděných Hertzových-Knudsenových experimentů pro vakuové prostředí plyne pro tok odpařovaných částic na jednotku plochy za čas ($cm^{-2}\,s^{-1}$) vztah

$$\Phi_e = 3{,}513 \cdot 10^{22} \frac{p_e}{\sqrt{MT}}, \tag{1}$$

kde p_e je rovnovážný parciální tlak neboli tlak nasycených par (v torech), M molární hmotnost atomů (molekul) a T absolutní teplota. Více praktická je rovnice pro rychlost vypařování hmoty Γ_e (v jednotkách $g{\cdot}cm^{-2}\,s^{-1}$):

$$\Gamma_e = 5{,}834 \cdot 10^{-2} \sqrt{M/T}\, p_e\,, \tag{2}$$

převzato z [26].
Tlak nasycených par p jednotlivých prvků lze získat z Clausiovy-Clapeyronovy rovnice

$$\frac{dp}{dT} = \frac{\Delta H(T)}{T\,\Delta V}\,, \tag{3}$$

kde změna entalpie $\Delta H(T)$ (objemu ΔV) odpovídá rozdílům hodnot pro plynnou a kondenzovanou fází. Objem plynné fáze (g) je mnohem větší než objem kapalné (l), respektive pevné (s) fáze. Proto objem kapaliny (pevné látky) může být oproti objemu plynné fáze zanedbán a v rovnici (3) lze pro objemový rozdíl psát $\Delta V = V_g - V_l \approx V_g$. Za předpokladu platnosti podmínek pro ideální plyn (nízká hustota reálného plynu apod.) lze ze stavové rovnice ideálního plynu změnu objemu vyjádřit jako:

$$\Delta V \approx V_G = R_0 T/p\,, \tag{4}$$

kde R_0 je univerzální plynová konstanta (R_0 = 8,3143 J K^{-1} mol^{-1}). Dosazením (4) do (3) získáme diferenciální rovnici

$$\frac{dp}{p} = \frac{\Delta H}{R_0} \frac{dT}{T^2}, \tag{5}$$

kde p je tlak nasycených par, T je teplota vypařování a ΔH je změna entalpie, tj. zde skupenské teplo, které dále předpokládáme teplotně nezávislé . Řešením rovnice (5) dostaneme

$$\ln p = \ln D' - \frac{\Delta H}{R_0 T}\,, \text{nebo}\ \ p = D' e^{-\frac{\Delta H}{R_0 T}} = D' e^{-\frac{B}{T}}. \tag{6}$$

Jestliže označíme $A = \ln(const) = \ln(D')$ a $B = \frac{\Delta H}{R_0}$, pak přirozený logaritmus tlaku nasycených par je

$$\ln p = A - \frac{B}{T} \ \Rightarrow\ p = e^{(A - \frac{B}{T})}\,, \tag{7}$$

kde A a B jsou konstanty charakterizující vypařovaný materiál. Uvedené závěry lze užít pro látky v definovaném teplotní rozsahu, ve kterém je změna entalpie (tj. skupenské teplo) konstantní. Nicméně v mnoha případech je skupenské teplo na závislé teplotě. Nejjednodušší případ nastává tehdy, je-li skupenské teplo lineární funkcí teploty, tj. $\Delta H = \Delta H_0 + cT$, kde ΔH_0 je skupenské teplo při $T = 0$ °C a c je konstantní charakteristikou odpařovaného materiálu. Poté se rovnice (5) doplní o substituci této lineární teplotní funkce

$$\frac{\boldsymbol{dp}}{\boldsymbol{p}} = \frac{\boldsymbol{\Delta H + cT}}{\boldsymbol{R_0\,T^2}}\,\boldsymbol{dT}\,, \tag{8}$$

převzato z [27]. Závislosti nasycených par na teplotě pro vybrané materiály jsou zobrazeny na obrázku 7. Podrobnější diskuse problematiky nasycených par lze najít v článcích [28, 29].
U atomárních (molekulárních) zdrojů je zpravidla zásobník vypařovaného materiálu opatřen malým otvorem, což může být tzv. „ideální“ otvor[2], kanálek nebo vícekanálové pole. Tvar a množství otvorů je dán požadavky experimentu na vlastnosti atomárních (molekulárních) svazků, jakými jsou intenzita, rozměry, divergence,… Nicméně pro zaručení molekulárního proudění otvorem (nazývaného efuzní tok), musí být rozměry otvoru podřízeny Knudsenově podmínce

$$\lambda_\mathrm{A} \gg d\,, \tag{9}$$

kde d je střední průměr průchozího otvoru a λ_A je střední volná dráha procházejících atomů (molekul) plynů. Jinými slovy během proudění v systému lze zanedbat srážky vystupujících atomů (molekul) v blízkosti výstupního otvoru. Tepelná rovnováha a absence kolizí znamenaná, že efuzní svazek atomů (molekul) obsahuje dobře definované rovnovážné rozdělení vnitřních stavů. Množství atomů (molekul) dN opouštějících zdroj přes ideální otvor o ploše A_S do prostorového úhlu dω pod úhlem Θ, viz obrázek 8a), lze popsat kosinovou distribuční funkcí

$$\mathrm{d}N = n\,\bar{v}\,A_\mathrm{S}\cos\Theta\,\frac{\mathrm{d}\omega}{4\pi}\,, \tag{10}$$

kde $\bar{v}$ je střední rychlost částic a n jejich koncentrace. Tu lze získal ze stavové rovnice ideálního plynu z tlaku p a teploty T ve zdroji

$$n = \frac{p}{k\,T}\,, \tag{11}$$

kde k je Boltzmannova konstanta. Integrováním rovnice (10) přes prostorový úhel 2π (vypařování pouze do poloviny prostoru) dostáváme celkový počet atomů opouštějících zdroj

$$N = \frac{n\,\bar{v}\,A_\mathrm{S}}{4}\,. \tag{12}$$

[2] „Ideální“ otvor (clona) se rozumí otvor s velmi malou tloušťkou stěny ve srovnání s lineárními rozměry otvoru (např. průměrem).

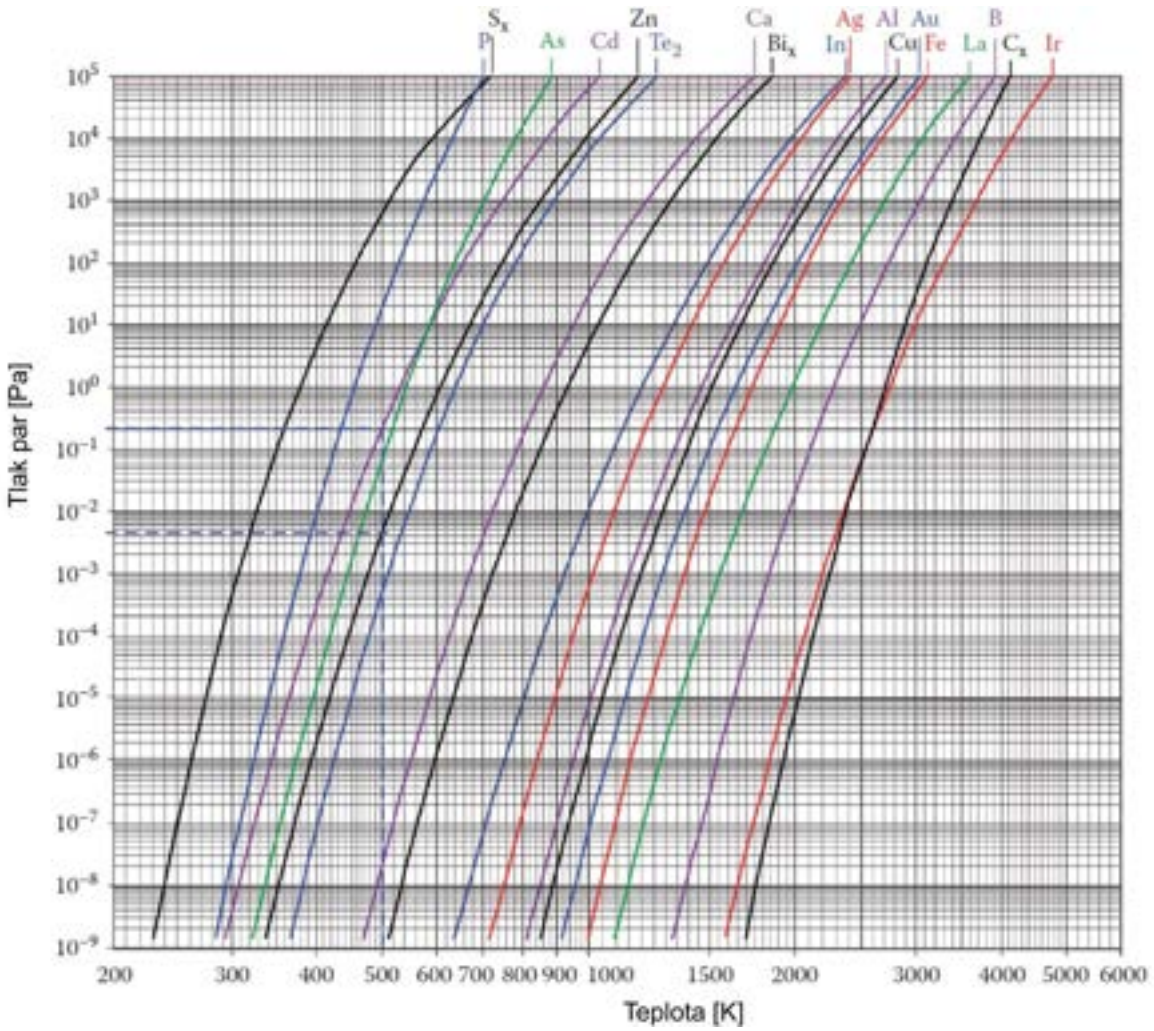

Obrázek 7: Závislosti tlaku nasycených par na teplotě pro vybrané materiály [27]. (popisky os docela velké… možná trochu zmírnit mřížku… jednotky obvykle ())

Velikost výstupního otvoru je svázána s tlakem podmínkou efuzního toku (9). Se zvyšujícím se tlakem dochází k poklesu střední volné dráhy λ_A, a proto se musí omezit velikost výstupního otvoru. Z těchto důvodů se pro reálné konstrukce uvádí ne tak striktní tvarová podmínka [30]

$$d \leq \lambda_A \ . \tag{13}$$

Při konstrukcí reálných atomárních zdrojů je nutno uvažovat také nenulovou délku l výstupního otvoru. Tvar a rozměry těchto otvorů ovlivňují úhlovou distribuci vystupujícího atomárního svazku, čímž lze ovlivnit jeho šířku. Proto se výstupní otvor z atomárního zdroje také nazývá kolimátor a pro jeho délku musí platit podmínka

$$\lambda_A \geq l \ . \tag{14}$$

Při narůstající délce výstupního otvoru dochází k nárůstu srážek mezi atomy, čímž dojde ke snížení množství atomů vystupujících z atomárního zdroje. K tomuto účelu se do rovnice (10) dodává redukční koeficient ζ

$$\mathrm{d}N = n\,\bar{v}\,A_S \zeta \cos\Theta\,\frac{\mathrm{d}\omega}{4\pi}, \tag{15}$$

který závisí na geometrii otvoru. Například pro kruhový otvor je dán vztahem [30]

$$\zeta = \frac{4}{3}\frac{d}{l}. \tag{16}$$

Pří charakterizaci svazku atomů se stanovuje úhel poloviční intenzity svazku $\Theta_{0,5}$, ve kterém dochází k snížení maximální intenzity na polovinu. Tento úhel se dá pro kruhový otvor přibližně určit ze vztahu

$$\Theta_{0,5} = 0{,}84\,\frac{d}{l}. \tag{17}$$

Změnou poměru *d/l* lze dosáhnout různé šířky atomárního svazku a zamezit tak nežádoucímu napařování stěn vakuových zařízení.

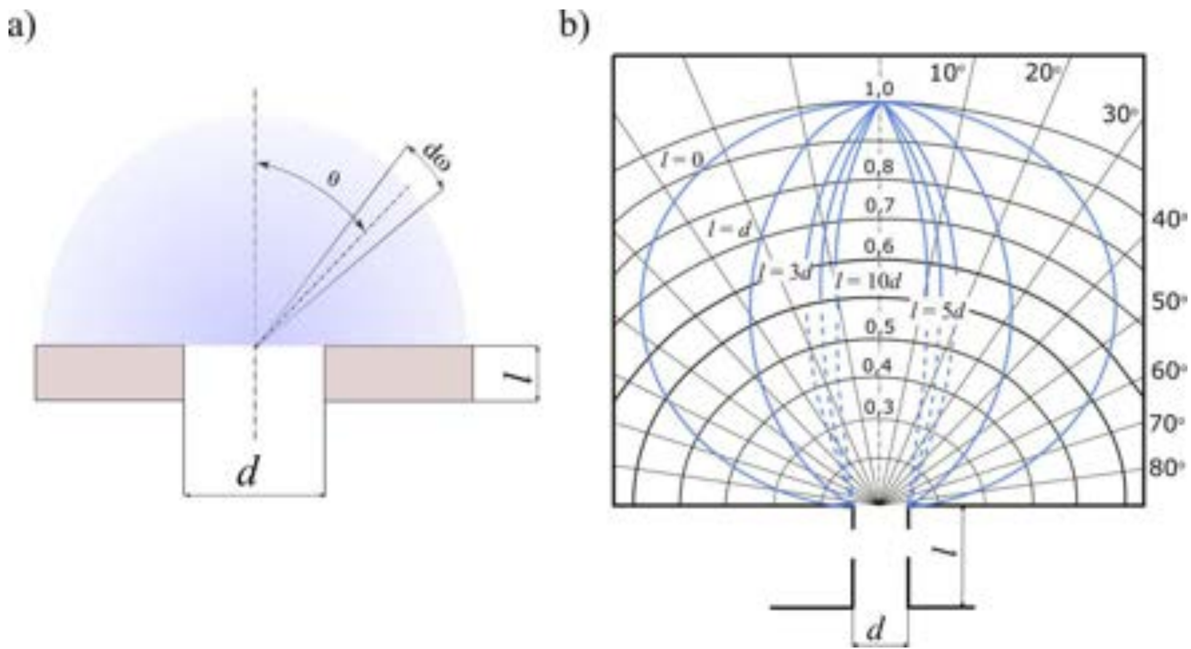

Obrázek 8: a) Geometrické vypařování přes výstupní otvor atomárního zdroje, b) úhlová kosinová distribuční funkce intenzity atomárního svazku pro různé poměry délek *l* a průměrů *d* kruhového výstupního otvoru [30].

Množství atomů (molekul) d*N* opouštějící prostor pod daným úhlem *Θ* atomárního zdroje je úhlově závislá veličina, která je popsána kosinovou distribuční funkcí. V případě ideálního výstupního otvoru atomy (molekuly) mají širokou úhlovou distribuci, kterou ale lze omezit vhodnou volbou průměru *d* a délky *l* výstupního otvoru, který nazýváme kolimační trubicí. Na obrázku 8b) je úhlová distribuční funkce pro různé poměry *d/l,* pomocí které lze získat základní představu o rozložení intenzity toku atomů (molekul) ve svazku. Vhodně zvolený tvar kolimační trubice nám umožní omezit atomární svazek tak, aby nedocházelo k nadměrnému napařování zařízení uvnitř experimentální komory. Omezit nežádoucí napařování materiálu (tedy zvýšit jeho směrovost) je důležité v případě provádění *in-situ* experimentů v komoře rastrovacího elektronového mikroskopu, kde by deponovaný materiál mohl ulpět na jeho objektivu, což by mohlo vést k výraznému zhoršení jeho zobrazovacích parametrů. Průměr otvoru kolimátoru je obvykle v rozmezí hodnot od 0,01 mm až po 10 mm. Mechanickým obráběním lze vyrábět obvykle otvory s průměrem větším než 0,1 mm. Menší otvory lze připravit pomocí elektrojiskrové eroze, leptáním nebo užitím laseru. Omezením rozměrů výstupního otvoru ale rovněž dochází ke snížení množství atomů (molekul) vystupujících z prostorů zdroje. Tuto skutečnost lze do značné míry eliminovat vytvořením větší skupiny malých otvorů, které tak vytvářejí

multikolimátor. Takový multikolimátor byl námi využit při realizaci vysokofrekvenčního (VF) disociačního zdroje atomů dusíku, kdy molekuly dusíku N_2 jsou ve (VF) plazmatu disociovány na atomární dusík (viz část 4.3.1). Plazmatická výbojová komora vyrobená z keramického materiálu pyrolitického nitridu boru (PBN) je opatřena 21 otvory o průměru 0,1 mm. Tato konstrukce zajišťuje dostatečné usměrnění atomárního svazku a potřebný spád tlaku. Fotografie zařízení je zobrazena na obrázku 9. Ve speciálních případech lze užít komerčně vyráběných skleněných dutých vláken, kdy výstupní otvory dosahují průměru jednotek mikrometrů [31].

Obrázek 9: Multikolimátor z PBN vyrobený na ÚFI tvoří zaslepená trubička o průměru 10 mm, jejíž čelo je opatřeno 21 otvory o průměrech 0,1 mm.

K nesporným výhodám užití atomárních (molekulárních) svazků patří zejména jejich univerzálnost, nízká spotřeba deponovaného materiálu, přesné určení distribuce rychlostí svazku (pro daný tlak a teplotu) a nízké nároky na čerpací rychlosti vývěv.

Jinou možností, jak získat atomární svazky, spočívá ve využití dynamiky expanze plynu do vakuového prostředí přes speciálně tvarované výstupní trysky, čímž lze získat svazky atomů (molekul) o vysoké intenzitě a úzkém rozptylu rychlostí. Tyto svazky jsou nazývány dynamické svazky plynů neboli „Nozzlovy svazky“. Jejich výhodou je vysoká intenzita svazků a velmi úzké rozdělení rychlostí.

Varianta efuzních svazků je užívána zejména pro materiály svazku s nízkým tlakem nasycených par nebo požadavkem dlouhou vydrž materiálu v zásobníku (například z důvodu neotvírání UHV systémů).

4.1 Nízkoteplotní zdroje atomů (do 400 °C)

Při konstrukci atomárních (molekulárních) zdrojů určených pro napařování materiálů s nízkou teplotou nasycených par je nutno dodržet některé zásady vyplývající z jejich fyzikálních vlastností. V odůvodněných případech je nutno zásobník s materiálem chladit pomocí tekutého dusíku nebo helia. Konstrukce pak vyžaduje zahrnutí tepelných štítu a omezení nadbytečného ohřevu chladicího média. Chladicí médium je obvykle přiváděno k zásobníku případně k výstupnímu otvoru zdroje nejčastěji tenkostěnnou nerezovou trubičkou.

Materiály deponované v rozsahu nízkých teplot (od cca 30 °C po cca 400 °C) vyžadují přesné nastavení napařovací teploty zásobníku materiálů ($\Delta T = \pm$ 1 °C). Ohřev materiálu (např. organické sloučeniny, molekuly DNA) v zásobníku efuzní cely je umožněn kontaktem s tekutým zahřátým médium (například olej). To umožňuje provádět ohřev a přesné měření teploty vně vakuové aparatury.

Jinou možností je užití odporového topného elementu v blízkosti zásobníku a změnu teploty provádět změnou velikosti elektrického proudu procházejícího elementem. Jako ukázka takového zdroje slouží námi navržený a na ÚFI FSI realizovaný zdroj atomů, který je určen pro napařování organických polovodičů (v našem případě organický polovodič PTCDI-C8) [32]. Tento nízkoteplotní zdroj atomů je složen ze tří nezávislých segmentů umožňujících depozici tří druhů materiálů. Deponovaný materiál je uložen v kalíšku z pyrolyticky nitrid boru (PBN), který je ke konstrukci zásobníku deponovaného materiálu často užíván zejména kvůli jeho chemické inertnosti a vysoké teplotní odolnosti tání (cca 1 200 °C). V prostředí vakua (které ze své podstaty vykazuje nízkou teplotní vodivost) je přenos tepla převážně realizován pomocí záření. Pro nízké teploty (do 400 °C) je ale i tento způsob přenosu tepla zanedbatelně malý. V uvedeném návrhu je pomocí žhaveného wolframového vlákna ohříván měděný držák PBN kalíšku, přes který je PBN kalíšek ohříván. Měděný materiál tohoto segmentu zajišťuje rovnoměrnou distribuci tepla po celé oblasti obklopující PBN kalíšek. Pro rychlejší a rovnoměrnější přenos tepla je prostor mezi měděným segmentem a PBN kalíškem vyplněn tekutým kovem (galium), viz schéma na obrázku 10a). Teplotní oddělení jednotlivých segmentů je zajištěno aktivním vodním chlazením měděného těla zdroje. 3D model a detail napařovacího segmentu popisovaného atomárního zdroje je ukázán na obrázku 10b). Výše popsaný nízkoteplotní zdroj atomů, zkonstruovaný a využívaný na ÚFI FSI, je veden jako funkční vzorek VaV ID 112182.

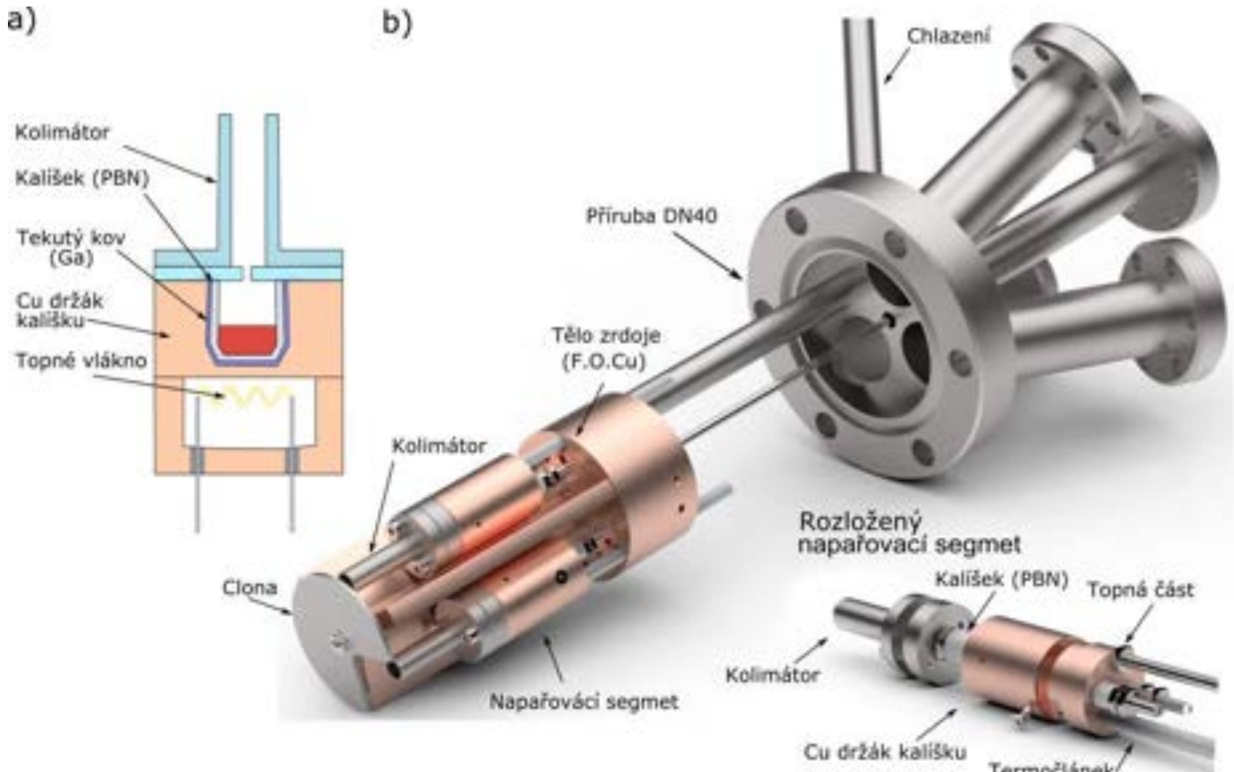

Obrázek 10: a) Schematické uspořádání napařovacího segmentu a b) 3D model atomárního zdroje usazeného na přírubě DN40, vyvinutého a používaného na ÚFI FSI pro napařování organických polovodičů (funkční vzorek VaV ID 112182).

Jiným příkladem zdroje atomárních svazků pracujícího za nízkých teplot je námi navržený a realizovaný zdroj atomů zinku. Zinek je kov s nízkou teplotou nasycených par: při teplotě 170 °C dosahuje tlak nasycených par hodnoty 1×10^{-4} Pa. Z těchto důvodů nesmí být tento materiál použit při konstrukci vakuových součástí, jelikož by během času docházelo ke kontaminaci (jak vzorků, tak i samotného zařízení) parami tohoto materiálu. Pro experimenty s tímto kovem bylo nutné vybudovat

samostatné vakuové zařízení s vlastním odděleným zakládáním a čerpáním. Pro práci se vzorky obsahující zinek je nutno užívat zvláště označené nosiče vzorku i nástroje. Při návrhu zdroje svazků atomů zinku byla brána v úvahu také skutečnost, že zinek silně kondenzuje na studených částech zdroje. Z těchto důvodů byl navržen zdroj s dvěma topnými vlákny (topná tělesa), zajištujícími ohřev PBN kalíšku s deponovaným materiálem i výstupní otvor zdroje. Konstrukce topných těles byla realizována netradičně za použití SiC. Tímto unikátním způsobem ohřevu lze docílit teploty v kalíšku až 900 °C. Oproti běžně užívanému tantalovému drátu je námi použitý SiC materiál inertní vůči vodíkové a kyslíkové atmosféře a vykazuje tvarovou stabilitu během ohřevu. Ohřev vláken je realizován pomocí průchodu proudu, kdy je kalíšek ohříván radiačním zářením vycházejícím z topných těles. 3D model uložení SiC vláken je zobrazen na obrázku 11. Užitím tohoto zdroje atomů zinku byly na ÚFI FSI připraveny Zn a ZnO ultratenké vrstvy a nanostruktury sloužící k dalšímu intenzivnímu studiu jejich fyzikálních vlastností [33].

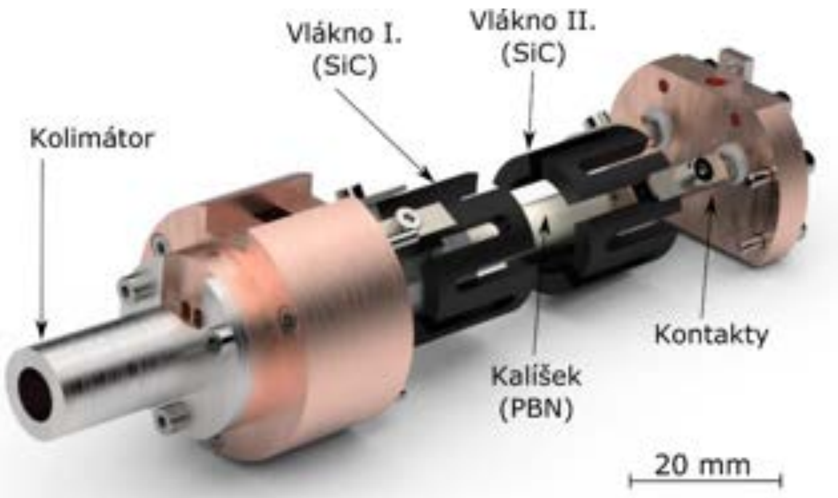

Obrázek 11: 3D model vnitřní části zdroje atomů zinku pracujícího při teplotě do 400 °C.

4.2 Teplotní zdroje atomů (do 1 000 °C)

Základem námi navržených konstrukcí teplotních zdrojů svazků atomů (molekul) je válcové tělo zdroje vyrobeného z bezkyslíkaté mědi (F.O.Cu), které je aktivně chlazeno vodou. Uvnitř měděného těla se nachází zásobník materiálu určeného pro depozici. Tento zásobník je vyroben z molybdenu, ve kterém je umístěna PBN vložka. Měděné tělo zdroje je napájeno niklovou pájkou na přírubu DN40, přes kterou je do prostředí UHV přiváděno elektrické napětí, chlazení a mechanický pohyb. Ohřev kalíšku uvnitř měděného těla lze realizovat pomocí emise záření vycházejícího ze žhaveného tantalového drátu obklopujícího kalíšek. Tento drát je žhaven přímým průchodem elektrického proudu. Systém žhavení je obklopen radiačními štíty vyrobenými z vysoce reflexních plechů (nikl, nerezová ocel nebo tantal). Snižují se tak tepelné ztráty zářením, což snižuje nároky na chlazení a spotřebu energie. Na obrázku 12a) je zobrazen zdroj atomů využívající popsaný princip ohřevu deponovaného materiálu spolu s námi navrženou elektronickou jednotkou. Tato jednotka pracuje v manuálním nebo automatickém režimu, což zajišťuje definované nastavení pracovních podmínek. Zmíněný typ zdroje atomů je vhodný pro depozici Au, Ag, Ge, CaF, Fe a byl v laboratořích ÚFI FSI užit v následujících pracích [34–36] a teplotní závislost ohřevu kalíšku zahřívaného emisí záření z proudem žhaveného odporového tantalového vlákna obklopujícího kalíšek s depozitem je zobrazena na obrázku 12b).

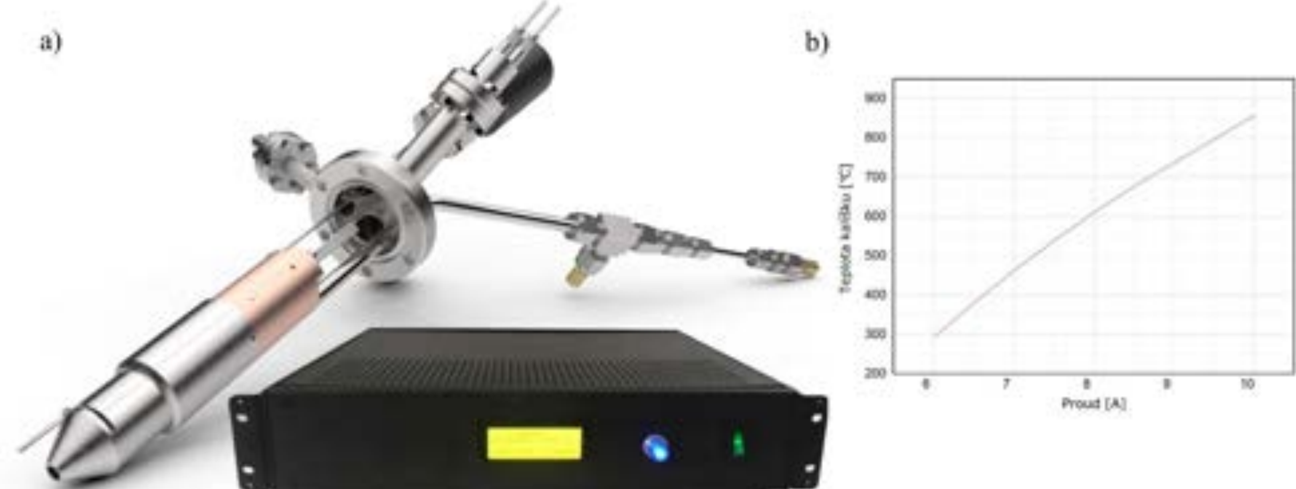

Obrázek 12: a) 3D model a ovládací elektronická jednotka námi navrženého zdroje atomů operujícího v rozsahu teplot od 300 °C až do 950 °C. b) Teplotní závislost ohřevu kalíšku zahřívaného emisí záření z proudem žhaveného odporového tantalového vlákna obklopujícího kalíšek s depozitem.

Jinou alternativu ohřevu deponovaného materiálu představuje námi navržený zdroj atomárních svazků využívající energie dopadu urychlených termoemisních elektronů. Při této konstrukci je na kalíšek z vodivého či nevodivého (keramického) materiálu umístěného v kovovém vodivém pouzdře přivedeno napětí 1 kV. V blízkosti kalíšku je umístěno wolframové vlákno, které je žhaveno průchodem proudu. Z tohoto vlákna jsou vlivem vysokého napětí extrahovány termoemisní elektrony a jejich dopad na kalíšek způsobuje jeho ohřev. Schéma zapojení je zobrazeno na obrázku 13a). Vlivem vysoké teploty vypařované atomy proudí efuzním tokem směrem na vzorek. Část vypařovaných atomů se sráží s elektrony proudícími na kalíšek, vlivem čehož vznikají parazitní ionty. Tento parazitní iontový proud může ovlivnit výsledky experimentů (například změnit výslednou morfologii rostené vrstvy). Na druhou stanu je ale možné z poměru počtu detekovaných iontů k počtu neutrálních částic odhadovat intenzitu toku atomárního (molekulárního) svazku.

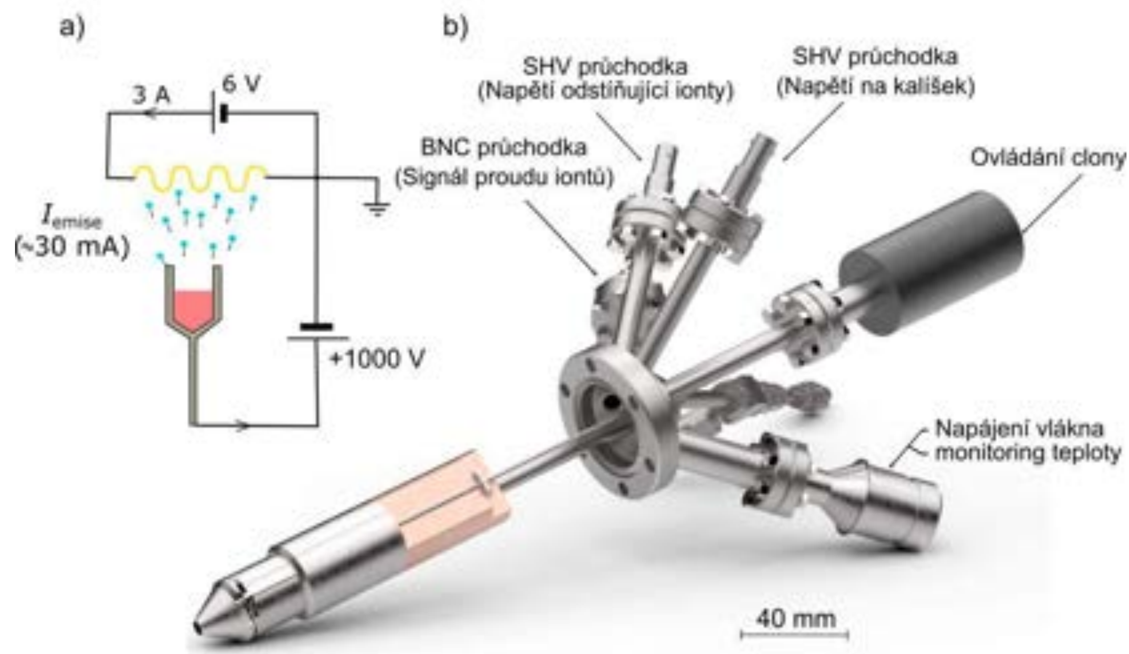

Obrázek 13: Zdroj atomů s realizovaným ohřevem kalíšku pomocí dopadu urychlených elektronů a) schéma jeho elektrického zapojení a b) 3D model umístěný na přírubě DN40.

Na obrázku 13b) je zobrazen 3D model námi navrženého a realizovaného zdroje atomů galia užívající k ohřevu kalíšku dopadu urychlených elektronů. Tento zdroj atomů je uzpůsoben pro depozice v rastrovacím elektronovém mikroskopu (SEM), takže nedochází k nežádoucí depozici materiálu na povrch objektivu mikroskopu. Z atomárního svazku je rovněž možné decelerační elektrodou odfiltrovat parazitní ionty, které způsobují rušivý signál během měření SEM. Navíc navržená unikátní konstrukce kalíšku umožňuje depozici kapalných materiálu ve směru shora dolů, což umožňuje provádět depozici přímo pod objektiv elektronového mikroskopu během jeho měření. Studium růstu nanostrukturálních materiálů v reálném čase je v současné době velmi žádané. Uvedený typ zdroje atomů je intenzivně využíván jak při vědecké, tak i pedagogické činnosti [37, 38].

4.2.1 Aplikace – depozice atomů Ga na grafen

Uvedené teplotní atomární zdroje jsou užívány v laboratořích Ústavu fyzikálního inženýrství FSI VUT v Brně ke studiu růstu ultratenkých vrstev. Jako příklad takového užití zdroje zde uvádím studium vlivu Ga atomů na transportní vlastnosti CVD grafenu. K tomuto účelu byly připraveny vzorky Si s 280 nm tlustou izolační vrstvou SiO_2, které byly pokryty CVD grafenem, tvořící FET uspořádání (viz část 2.1). Na takovéto povrchy byly deponovány atomy Ga v UHV podmínkách. K provedení tohoto studia bylo navrženo a vyhotoveno UHV zařízení umožňující současnou depozici Ga a *in-situ* měření elektrických transportních vlastností grafenového FET tranzistoru. Podrobnější popis konstrukce měřicí aparatury je popsána v diplomových pracích [19, 39]. Toto studium prokázalo rozdíl mezi dopováním samostatných Ga atomů na povrchu grafenu oproti dopování Ga ostrůvky obsahujícími 2 a více atomů. Toto pozorování bylo rovněž doplněno DFT výpočty. Podrobnější popis nalezneme v přiloženém článku v části 4.2.2.

4.2.2 Článek č. 3 – Elektrické transportní vlastnosti grafenu dopovaného galiem

Autoři:

J. Mach, P. Procházka, M. Bartošík, D. Nezval, J. Piastek, J. Hulva, V. Švarc, M. Konečný, L. Kormoš a T Šikola

Nanotechnology [online]. 2017, **28**(41), 415203. Dostupné z: doi:10.1088/1361-6528/aa86a4.

Abstrakt:

V této práci prezentujeme účinek nízkého pokrytí (méně než čtyři monovrstvy) galia v podmínkách UHV (10^{-7} Pa) na dopování grafenu elektrony a rozptyl nosičů náboje v grafenu rosteném metodou chemické depozice z plynné fáze. Měření transportních vlastností grafenu prováděná *in situ* na grafenových polem řízených tranzistorových strukturách ukazuje, že při nízkém pokrytí Ga má grafenová vrstva tendenci silného n-dopování s účinností 0,64 elektronu na jeden atom Ga, zatímco další depozice a tvorba shluků Ga vedou k odstranění elektronů z grafenu (nižšímu n-dopování). Výsledky experimentu jsou podpořeny výpočty pomocí teorie funkcionálu hustoty elektronů (DFT) a vysvětleny jako důsledek odlišné interakce mezi grafenem a atomy Ga v případě jednotlivého atomu, vrstvy anebo jejich shluků.

IOP Publishing Nanotechnology
Nanotechnology 28 (2017) 415203 (10pp) https://doi.org/10.1088/1361-6528/aa86a4

Electronic transport properties of graphene doped by gallium

J Mach[1,2], P Procházka[1,2], M Bartošík[1,2], D Nezval[2], J Piastek[2], J Hulva[2], V Švarc[2], M Konečný[2], L Kormoš[1] and T Šikola[1,2]

[1] Central European Institute of Technology—Brno University of Technology (CEITEC BUT) Purkyňova 123, 612 00 Brno, Czechia
[2] Institute of Physical Engineering, Brno University of Technology, Technická 2, 616 69 Brno, Czechia

E-mail: bartosik@fme.vutbr.cz

Received 26 June 2017, revised 1 August 2017
Accepted for publication 16 August 2017
Published 14 September 2017

Abstract

In this work we present the effect of low dose gallium (Ga) deposition (<4 ML) performed in UHV (10^{-7} Pa) on the electronic doping and charge carrier scattering in graphene grown by chemical vapor deposition. *In situ* graphene transport measurements performed with a graphene field-effect transistor structure show that at low Ga coverages a graphene layer tends to be strongly n-doped with an efficiency of 0.64 electrons per one Ga atom, while the further deposition and Ga cluster formation results in removing electrons from graphene (less n-doping). The experimental results are supported by the density functional theory calculations and explained as a consequence of distinct interaction between graphene and Ga atoms in case of individual atoms, layers, or clusters.

Keywords: graphene, gallium, CVD, DFT, transport, doping

(Some figures may appear in colour only in the online journal)

1. Introduction

Graphene, a single atomic layer of carbon atoms arranged in a hexagonal lattice, with its excellent electrical [1–4] mechanical [5, 6], and optical properties [7, 8], surface to volume ratio, and chemical reactivity [9], has been considered as a promising candidate for the future devices. Its unique electronic structure results from the zero band gap and the conical dispersion close to the K points in the Brillouin zone where the conduction and valence bands touch each other in the charge neutrality point (CNP). In the real devices, however, the interaction of graphene layer with surrounding atoms can strongly affect delocalized electrons, change the CNP, Fermi level position, and the corresponding doping type [10–14].

One of the most common factors influencing transport properties of graphene is related to the bonds between the substrates which are often used as a supporting layer for graphene e.g. SiO_2 [15, 16], BN [17], MoS_2 [18], SiC [19] and metals for graphene grown by chemical vapor deposition (CVD) [20–23]. Other important sources of electronic disruption in graphene are its structural defects [24, 25] i.e. disclinations, dislocations and grain boundaries [26]. These imperfections are determined mainly by a graphene fabrication process. In addition, graphene transport properties can be also strongly affected by atoms and molecules adsorbed on the graphene surface.

Since the investigation of graphene transport properties necessarily involves the conductive interface between graphene and metal electrodes, a considerable effort has been also devoted to the experimental [27–32] and theoretical [33–40] studies of a graphene–metal (G–M) junction. Using the density functional theory (DFT) Giovannetti *et al* [33] have shown that G–M interfaces can be divided into two classes of interfacial bonding, the first one with weaker bonds and a larger equilibrium separation between graphene and metal atoms (Ag, Al, Cu, Cd, Ir, Pt, Au) and the second one with stronger bonds and a smaller equilibrium separation (Ni, Co, Ru, Pd, Ti) which are characteristic for the physisorption and chemisorption, respectively.

In the case of physisorption, the influence of Ga and Al atoms differs from the other atoms because of the interaction of their valence p-electrons with π-electrons of graphene [41, 42]. However, all metals in this group do not form chemical bonds with graphene and, hence, the doping type

 © 2017 IOP Publishing Ltd Printed in the UK

and shift of CNP can be deduced from the G–M work function (WF) difference. Another important factor which has to be considered, is a potential step, which is related to the presence of an interfacial dipole [33]. For metals bonded to a graphene layer by chemisorption the band structure becomes more complicated because of a strong hybridization between the graphene pz orbitals and the valence electrons of metals.

As Wu *et al* [43] experimentally and theoretically showed for the G–Au interface, the chemical bonds and related interfacial WF difference can be tuned by the amount of deposited Au, and also by morphology: isolated Au nanoparticles n-dopes the graphene, while continuous Au film results in graphene p-doping. A similar behavior was observed also for the G–Pt interface [27].

A thorough study and understanding of changes in graphene electric properties caused by the interaction between graphene and adsorbed Ga atoms is very important, especially for development of electric devices using Ga semiconductors (GaAs, GaN, …). However, such a thorough study probing the influence of different coverages of Ga atoms has not been performed so far, except that one for a fixed coverage of 200 ML Ga atoms [41]. Nevertheless, this study was provided under atmospheric conditions and thus the influence of molecules from the surrounding atmosphere could not be limited and controlled.

In this article, we study the graphene–gallium interface in detail with regard to its experimentally measured transport properties, and corresponding changes of electronic properties calculated by *ab initio* DFT.

2. Methods

In order to achieve a large area coverage, a polycrystalline graphene layer was prepared by the standard low pressure CVD method [20]. As a substrate an ultrasmooth copper foil with no additional mechanical or chemical pretreatment was used for graphene growth [44]. First, the copper foil was annealed in a flow of hydrogen (4 sccm, 10 Pa, 1000 °C, 30 min) to remove air adsorbates. Subsequently, methane was introduced (40 sccm, 70 Pa, 1000 °C, 30 min) and graphene grown in a H_2/CH_4 mixture. Finally, the graphene from the bottom side of the copper substrate was removed in an oxygen–argon plasma (20% O_2, 80% Ar, 2 min), while that one from the top side was protected from etching by a spin-coated PMMA layer.

Using a PMMA-assisted wet transfer method, graphene was transferred on a p-doped silicon substrate (resistivity of $(0.1–1.5) \times 10^{-3}$ Ω cm) with 280 nm SiO_2 and prefabricated Au (45 nm)/Ti (3 nm) electrodes. The area between these electrodes, covered with graphene, then define a geometry of the measured graphene channel with the length $L = 50\ \mu m$ and width $W = 400\ \mu m$.

By applying a back-gate voltage (V_{BG}) to a silicon substrate, one is able to locally control a charge carrier density $n = (\varepsilon_0\varepsilon_r/ed)V_{BG}$, where ε_0 is the vacuum permittivity, ε_r is the relative permittivity of SiO_2 (3.9), e is the elementary charge and d is the thickness of the SiO_2 layer. Then, the graphene resistivity $\rho = RW/L$ as a function of V_{BG} defines a doping type and charge carrier mobility.

Resistance R of the graphene layer between the Au electrodes was measured using a lock-in amplifier SR830 (Stanford Research Systems) with a frequency of 1333 Hz, fixed current of 100 nA, and back-gate voltage being changed with a sweeping rate 0.6 V s^{-1} in a range of ±80 V.

Ga atoms with thermal energy were evaporated by an e-beam effusion cell (Omicron EMF 3) from a PBN crucible inserted into a Mo cover. *In situ* transport measurements were carried out without breaking ultrahigh vacuum ($p_{base} = 4 \times 10^{-7}$ Pa).

The DFT study was performed by the Vienna *ab initio* Simulation Package (VASP) [45–47]. All our DFT calculations were carried out using the projected augmented wave method [48, 49] and an energy cut-off of 600 eV. The generalized gradient approximation proposed by Perdew *et al* [50] was adapted to treat the electronic exchange and correlation. A vacuum spacer of 17 Å was used to eliminate the interaction between the layers in the neighboring supercells. A Γ-centered 3 × 3 × 1 Monkhorst–Pack mesh [51] was used for structure optimizations. For the calculation of the density of states (DOS) a 9 × 9 × 1 mesh was used. All structures were relaxed with a tolerance of residual forces of 0.01 eV Å^{-1}.

3. Experimental results

The influence of Ga deposition on graphene transport properties is shown in figure 1(a). The CNP of as-prepared graphene is positioned at positive values of the back-gate voltage, indicating an effect of pre-existing adsorbates which positively dope a graphene layer [52–54]. The sample annealing under vacuum at $T = 120$ °C promoted their desorption, and in 24 h resulted in shifting the graphene CNP to only $V_{BG} = 3$ V, which was a starting point for Ga deposition. During the first seconds of the deposition, when the Ga coverage is much less than one monolayer, Ga atoms strongly n-dope the graphene layer (indicated by arrow 1). The CNP was shifted outside the measured range of $V_{BG} < -80$ V at a Ga surface concentration of about 9.7×10^{12} cm^{-2} (∼0.01 ML coverage).

During the subsequent deposition the CNP was removed left outside the measurement back-gate voltage range and then only the decrease or increase of the resistivity curve was observed. It can be assumed, that the resistivity decrease or increase corresponds to the shift of CNP into the left or right, respectively. The decrease of resistivity indicating the n-doping of graphene continued up to a Ga surface concentration of ∼40×10^{12} cm^2 (∼coverage 0.04 ML), and then the reversal increase of the resistivity was observed (indicated by arrow 2). After this return point, graphene starts to be less n-doped (removing electrons from graphene).

The charge carrier density n_c and related experimental CNP position for low Ga surface concentrations of up to ∼9.1×10^{12} cm^2 is plotted in figure 1(b) as a function of this Ga surface concentration. The red line in the graph represents

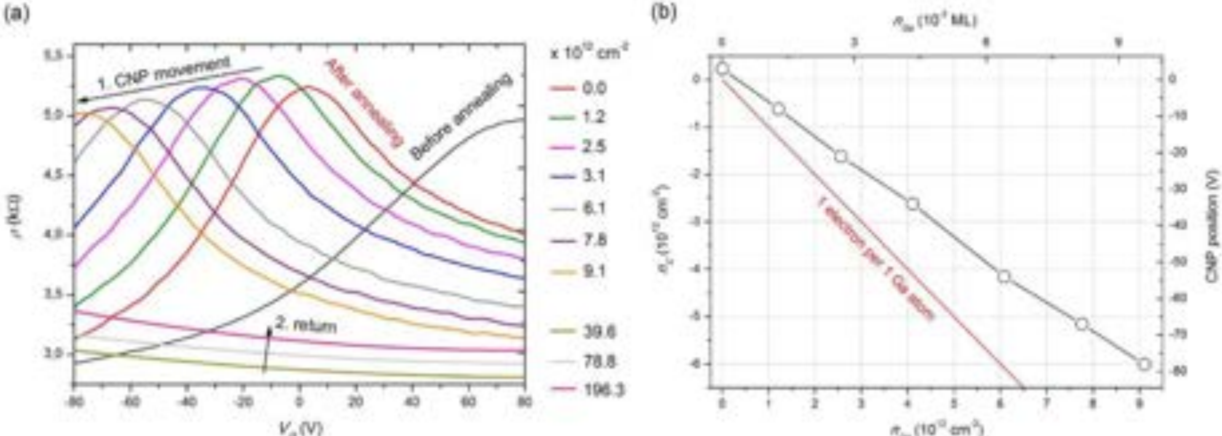

Figure 1. (a) Resistivity as a function of back-gate voltage of a graphene sample and its development with the growing surface concentration of deposited Ga atoms. Before annealing (black), and after 24 h of vacuum annealing at 120 °C (red). The arrow 1 indicates an evolution of CNP position during the Ga deposition corresponding to n-doping. The arrow 2 indicates a reversal resistivity evolution for CNP shifts less than $V_{BG} < -80$ V related to a decrease of n-doping. (b) Charge carrier density and relevant CNP position during the Ga deposition (negative values corresponds to electrons). The n-doping is caused by an electron transfer from Ga to graphene. The theoretical red line depicts charge carrier densities related to a transfer of one electron from one Ga atom.

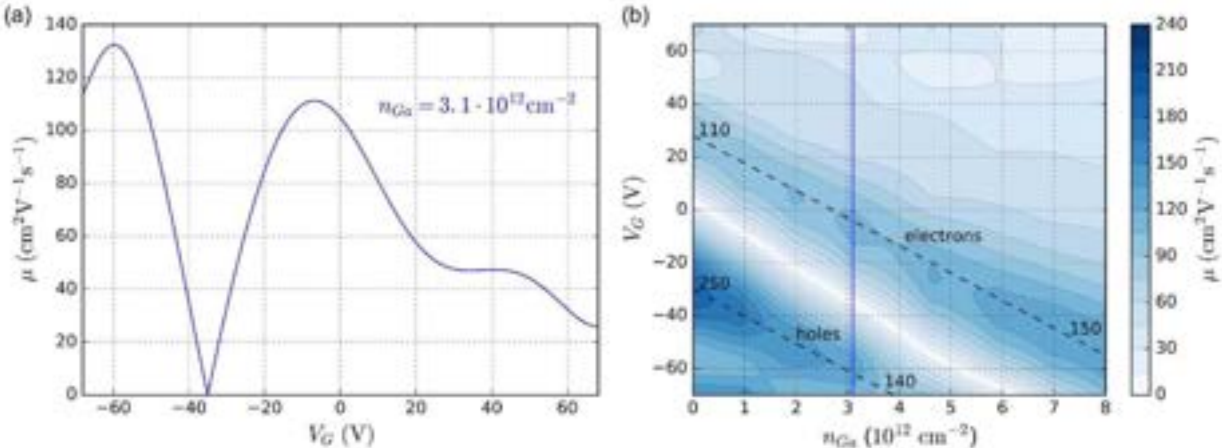

Figure 2. (a) Charge carrier mobility as a function of back gate voltage calculated according to Drude's model using the curve in figure 1(a) for a Ga concentration of 3.1×10^{12} cm^{-2}. (b) Evolution of charge carrier mobility as a function of back gate voltage during deposition of the Ga atoms on graphene.

the theoretical charge carrier density related to the case when one Ga atom supplies one electron into the graphene layer. The experimentally measured positions of CNP and related charge carrier density decrease more slowly, the calculated doping efficiency is only about 0.64 electrons per Ga atom.

The data of charge carrier mobility plotted in figure 2(a) were calculated from the curve corresponding to the Ga surface concentration 3.1×10^{12} cm^{-2} (figure 1(a)—blue curve) as a function of back gate voltage according to Drude's model of diffusive transport $\mu = (ne\rho)^{-1}$. Decreasing graphene mobility with the increasing charge carrier density results from a nonlinear dependence of graphene resistivity on carrier concentration due to the long and short range scatterers [17, 55–57]. A minimum value of graphene mobility at $V_{BG} = -37$ V then define a CNP position and therefore a number of dopant carriers.

Figure 2(b) shows an evolution of charge carrier mobility during the Ga deposition calculated from the curves in figure 1(a) valid for Ga concentrations $(0\text{–}1) \times 10^{13}$ atoms cm^{-2}. The electron–hole asymmetry of the annealed sample with respect to CNP (zero mobility) is often caused by Au/Ti contacts [58, 59], charged impurities and strained grapheme [60]. The CNP shift to negative values of back gate voltage during the Ga deposition indicates an electron transfer from Ga to graphene. The electron transfer is accompanied by a remarkable decrease of the hole-mobility due to creation of new scattering centers. A slight increase of electron mobility can be explained by neutralization of charged defects, which scatter electrons more strongly than holes [60].

The electron and hole mobilities achieve their maxima at voltages distant in both directions from the CNP by about 30 V (the highest mobility value in figure 2), the maximums

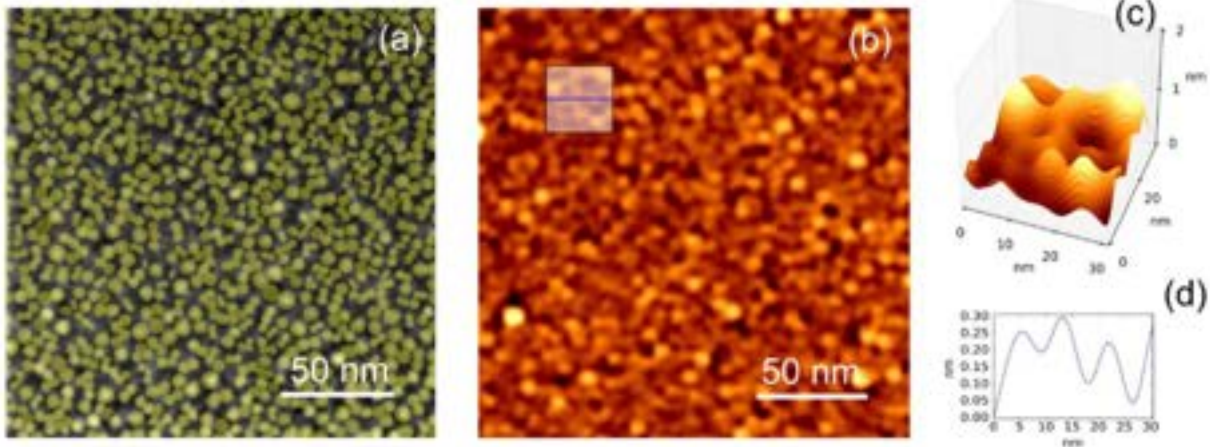

Figure 3. (a) SEM image of a surface with a high Ga concentration of 37.6×10^{14} cm^{-2} (∼4 ML) provided with yellow circles constructed with respect to the nearest Ga islands, (b) AFM topography of this surface, (c) detailed AFM 3D topography (marked by the grey square in b), and (d) the corresponding profile of Ga islands (marked by the blue line in b).

of the electron-mobility reaches 110–150 cm^2 V^{-1} s^{-1}, and the hole-mobility 140–250 cm^2 V^{-1} s^{-1}. Such a small value can be hardly compared 2×10^5 cm^2 V^{-1} s^{-1} for suspended graphene at cryogenic temperatures [1, 2] or even with 4×10^4 cm^2 V^{-1} s^{-1} obtained for high quality exfoliated graphene on SiO_2 at room temperature [15]. Generally, the CVD graphene exhibits the lower mobility which is ideally about [20] 4050 cm^2 V^{-1} s^{-1}. Under less ideal growth conditions, due to line defects at grain boundaries, the mobility can fall down to the value [61] 1100 cm^2 V^{-1} s^{-1}, which is still quite high in comparison with our mobilities. Therefore, the lower hole and electron mobilities in our experiment can be probably attributed to higher density of grain boundaries [24]. A certain role can also play impurities disturbing the crystal order, and also a long-range Coulomb scattering caused by induction of electrons by Ga adsorbed atoms.

The scanning electron microscopy (SEM) image (figure 3(a)), and atomic force microscopy (AFM) topography (figure 3(b)) were taken *ex situ* after the deposition of quite huge Ga concentration of 37.6×10^{14} cm^{-2} (∼4 ML). Such a huge concentration (exceeding the maximum concentration 0.5 ML in transport experiments) was necessary to observe the gallium on a surface due to the SEM and AFM resolution. It is obvious the gallium forms islands at such a high concentration. The yellow circles in the SEM image (figure 3(a)) mark the areas of gallium islands with respect to the nearest neighbor. The average radius of these circle areas corresponding the average lateral diffusion radius of Ga atoms is 2.2 ± 0.6 nm. The view on individual Ga islands can be observed in detailed 3D AFM topography (figure 3(c)), and corresponding profile (figure 3(d)).

When Ga coverages were increased to values of 140–300 ML the CNP returned into the measurable range ($V_{BG} > -80$ V). However, the electron and hole-mobilities were reduced approximately by one order of magnitude. At these high coverages the huge droplets of diameters about 400 nm were formed. Therefore, one can assume that transport properties might be affected by stress between Ga droplets and the graphene layer [62], and by the surface conductivity of metallic gallium. Hence, these high coverages are not addressed in the following analysis.

4. Computational results

First, a hexagonal free-standing graphene structure was relaxed and the lattice constant estimated to a value of 2.47 Å. The calculated free-standing graphene had no initial doping—the Fermi energy precisely crossed the CNP.

Three possible sites were considered for the adsorption of gallium atoms on graphene (figure 4(a))—on top of a carbon atom (T), at the center of a carbon hexagon (C) and above a carbon–carbon bond (B). Comparison of the adsorption energies at these sites has shown the site C is the most stable position of Ga atoms with an adsorption energy of 987 meV and a distance of 2.22 Å from the graphene layer (figure 4(a) bottom).

Furthermore, the influence of different Ga concentrations in the range of $4.7 \times 10^{12} - 2.8 \times 10^{15}$ cm^{-2} on the graphene electronic properties was studied. The calculations were mostly performed using a 8×8 graphene superstructure, and only for the lowest concentrations larger superstructures were used (16×16 for 7.4×10^{12} cm^{-2}, 18×18 for 5.8×10^{12} cm^{-2}, 20×20 for 4.7×10^{12} cm^{-2}). First, the Ga atoms were relaxed on the graphene surface, then the electronic band structure and DOS were calculated for all the concentrations. The concentration of charge carriers in graphene was determined from the site-projected DOS.

The examples of band structures and DOS calculations for two different Ga concentrations (3.0×10^{13} cm^{-2} and 4.7×10^{14} cm^{-2}) are shown in figure 5. The energy band diagrams (figures 5(a), (b)) prove the n-doping of graphene by gallium, since the Fermi level is above the CNP. The higher concentration of Ga atoms moves the Fermi level more above

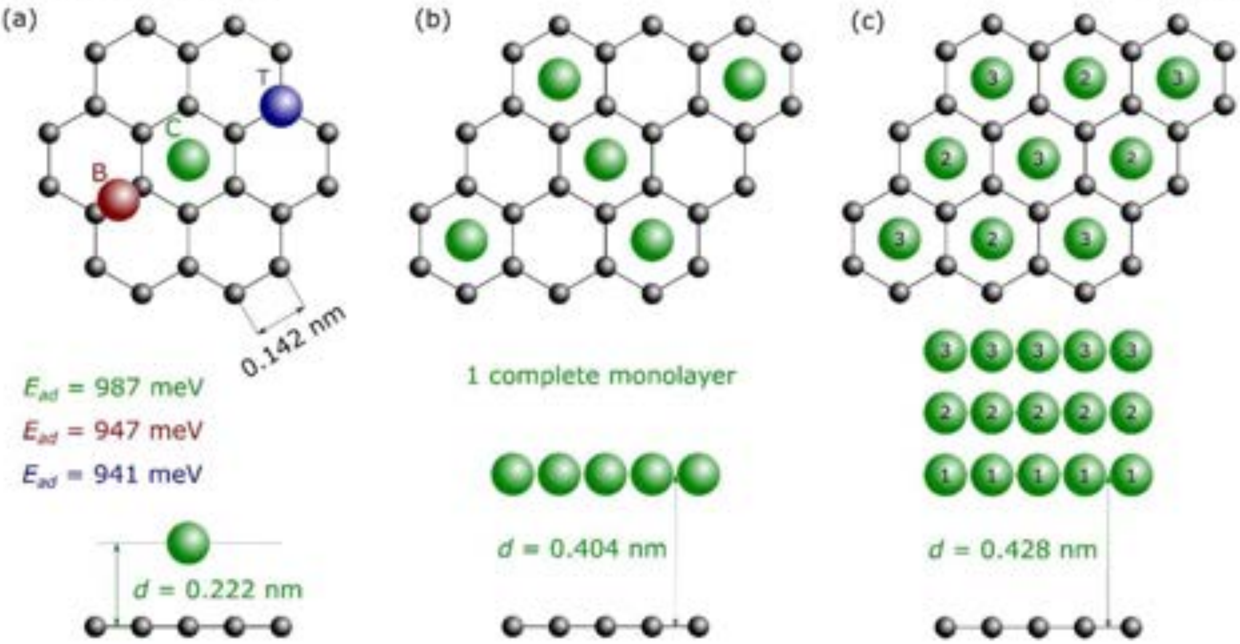

Figure 4. Space arrangement of Ga atoms on a graphene hexagonal lattice in DFT calculations in case of layer-by-layer growth. (a) Three different adsorption sites of Ga atoms—top view, corresponding adsorption energies, and a side view of an individual Ga atom in the central position. (b) The first complete monolayer of gallium atoms in the central positions on graphene—top view, and the distance between Ga and graphene monolayers—side view. (c) The first three gallium monolayers—top view, and their distance from graphene—side view (corresponding layers are labeled by numbers).

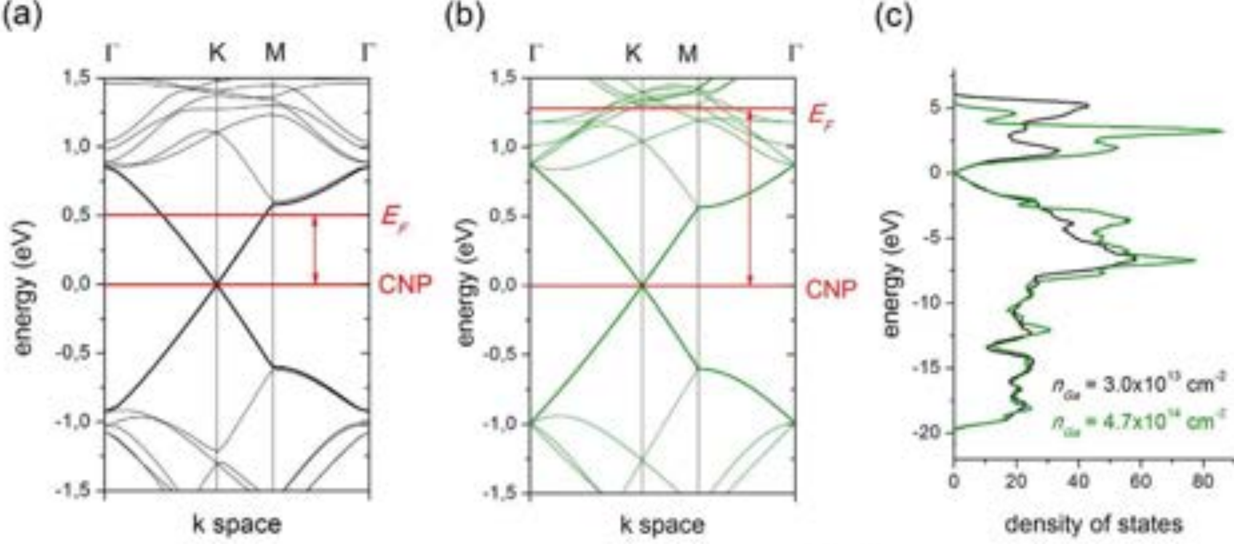

Figure 5. DFT calculated band structures of graphene for Ga concentrations (a) $3.0 \times 10^{13}\ \mathrm{cm}^{-2}$ and (b) $4.7 \times 10^{14}\ \mathrm{cm}^{-2}$, (c) the corresponding DOS.

the CNP, however, the band gap in graphene is not opened. The DOS values (figure 5(c)) close to the CNP are higher for the higher Ga concentration which is caused by formation of new states associated with additional Ga atoms.

The density of charge carriers n_C in the graphene layer (doping) as a function of deposited Ga concentration n_{Ga} calculated by DFT is shown in figure 6(a)—green dots. There are two doping regions. When the concentration of Ga atoms is below $4.7 \times 10^{14}\ \mathrm{cm}^{-2}$ (<0.5 ML) that corresponds to a Fermi level shift of 1282 meV (see figure 5(b)), the graphene electron concentration is increasing, above this Ga concentration value the electron concentration is rapidly decreasing. The DFT calculated charge carrier concentration was fitted by a reasonably smooth curve (black dashed line in

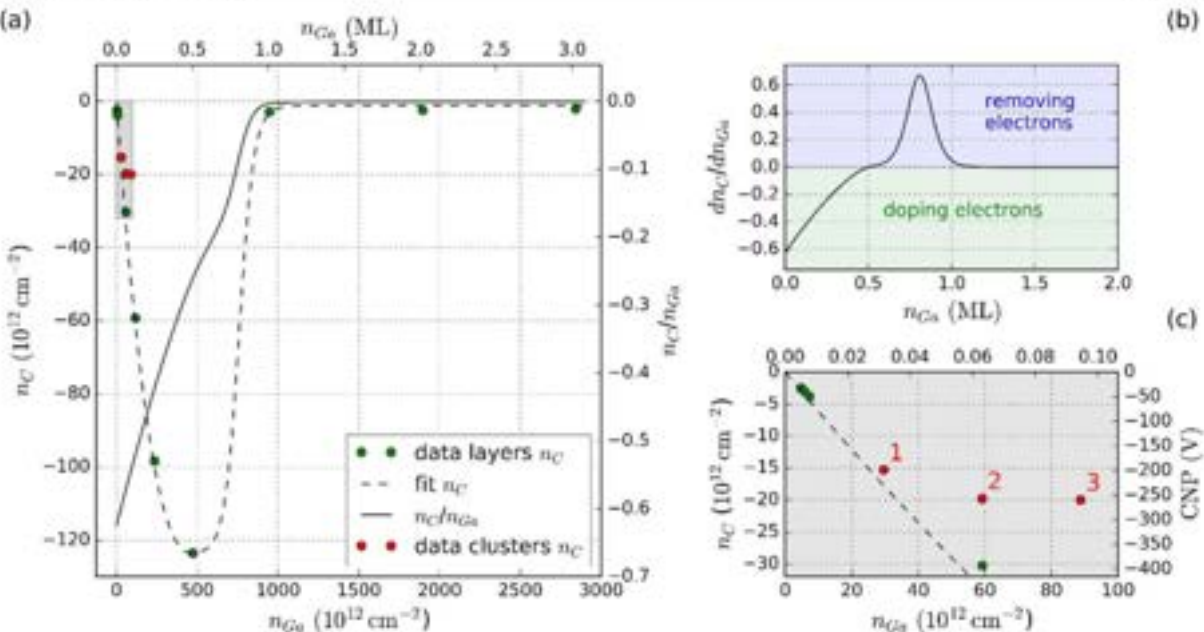

Figure 6. (a) Calculated density of charge carriers (electrons) in graphene as a function of Ga concentration. The green dots are the results of DFT calculation that were fitted by the black dashed curve. The average number of charge carriers per one Ga atom is expressed by the black solid curve. (b) The change of the number of charge carriers per every additional Ga atom was obtained by differentiation of the fitting black dashed curve, and the green and blue areas separate the doping by electrons and removing electrons, respectively. (c) The detail of the chart in (a) (marked by the grey rectangle) where the red dots are the results of DFT calculation for an individual atom (1), and clusters consisting of two (2), and three (3) Ga atoms as depicted in figures 7(a)–(c).

figure 6(a)) which was used for the calculation of an average number of electrons supplied by one Ga atom (n_C/n_{Ga}—black solid line in figure 6(a)), and the change of the electrons inside graphene caused by one additional Ga atom (dn_C/dn_{Ga}—black solid line in figure 6(b)). At the lowest Ga coverage (0.005 ML) the average number of electrons brought by one Ga atom is about 0.6, however, this number rapidly goes down when the Ga concentration increases. At the higher Ga concentration 4.7×10^{14} cm^{-2} (∼0.5 ML) it is equal only to 0.26 electrons per one Ga atom and then goes to zero (figure 6(a)—black solid curve). The DFT calculation for layer-by-layer growth shows the gallium effectively n-dopes graphene only up to the coverages corresponding to the 0.5 ML where the charge carrier density is the most negative (peak in figure 6(a)). Adding more Ga atoms above the coverage of the 0.5 ML the charge carrier density rapidly goes to zero which is caused by the extraction of electrons from graphene (figure 6(b)).

The decrease of electron-doping with higher Ga concentration is a direct result of our DFT calculations. Considering all the DFT results, it can be better understood via the distancing of Ga atoms from the graphene surface (figure 4). The equilibrium distance between the layer of Ga atoms and graphene is approximately 2.2 Å for low Ga coverages (< 0.5 ML), 2.3 Å for the 0.5 ML coverage and more than 4 Å for higher coverages (>0.5 ML). In other words, the further the Ga atom from graphene is, the less graphene is doped. In this context, the significant decrease of graphene doping by Ga at concentrations corresponding to the 0.5–1.0 ML coverages can be explained by a profound (almost double) increase of the distance between Ga and graphene (from 2.2 to 4.0 Å). Although the distance between Ga and graphene gradually increases with the concentration, the step change in the distance is associated with the creation of much stronger chemical bonds between gallium atoms when the complete first monolayer is formed. Consequently, the creation of chemical bonds between Ga atoms weaken the interaction between the Ga atoms and graphene that results in this step increase of the distance between the Ga monolayer and the graphene. A further smaller increase of the Ga-graphene distance can be observed when the second, and third complete Ga layer is formed (Ga-graphene distance for two layers of Ga is 4.13 Å and for three layers of Ga is 4.28 Å—figure 4(c)). However, the effect is not as significant as in case of the first monolayer completion.

This fact is supported by the comparison of the adsorption energy of the individual Ga atom, and a monolayer of Ga atoms on a graphene surface, which is 987 meV, and 8 meV (per one Ga atom), respectively. It means the attractive interaction of individual Ga atoms onto the graphene is much weaker (more than hundred times) when the complete monolayer is formed.

The effect of strong chemical bonds between neighboring Ga atoms at short distances is especially important if we assume the gallium prefers the clusters (islands) growth before layer-by-layer growth. In this case the withdrawal of the Ga atoms from the surface as a consequence of strong Ga–Ga chemical bonds begins at much lower concentrations as can be seen in figures 7(a)–(c). Here, the DFT calculated

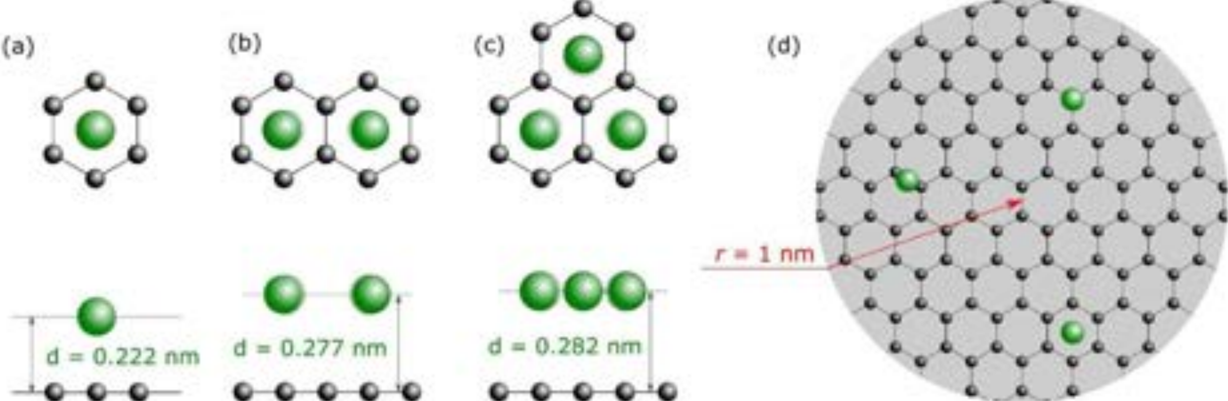

Figure 7. Space arrangement of Ga atoms on the graphene hexagonal lattice obtained from DFT calculations for small Ga clusters: (a) individual Ga atom, (b) two-atom cluster, (c) three-atom cluster. Top: top view, bottom: side view. (d) Estimation of the Ga diffusion length on a circle area.

arrangement of small clusters consisting of two and three Ga atoms in C sites is depicted. Adding Ga atoms into a cluster causes their lateral displacement mutually from each other and also relatively with respect to the original C site, and a noticeable lift of Ga atoms from the surface. In case of the two- and three-Ga atom cluster the equilibrium distance of Ga atoms from the graphene surface is 2.78 Å, and 2.88 Å, respectively. This is a quite significant increase (more than 24%) in comparison with the original distance of the individual Ga atom from graphene (2.2 Å)—see figure 7(a).

The DFT calculated charge density of electrons in graphene for doping from Ga clusters is depicted as red points in figure 6(c). It can be seen that two- (point 2), and three- (point 3) Ga atom clusters dope the graphene significantly less than layer-by-layer grown Ga atoms at the same concentration (red points are above the green points and fitting dashed black curve). Moreover, the charge carrier density of two- and three-Ga atom clusters is almost the same, approximately $-20 \times 10^{12}\,\mathrm{cm}^{-2}$, so that the saturation of doping occurs in case of the island (cluster) growth at much lower Ga concentrations than in case of the layer-by-layer growth.

5. Discussion

During the real experiments (part III), Ga was deposited on graphene, and the change of transport properties was measured at room temperature. Therefore, temperature activated surface diffusion of Ga atoms along the graphene surface occurs which might lead to cluster formation. On the other hand, the DFT calculation was performed for static arrangement of atoms, which corresponds to conditions at absolute zero temperature.

Furthermore, the DFT software VASP enables the calculation of large system only if they can be combined from smaller periodic structures. Thus, the numerical processing of individual Ga atoms or layers of periodically arranged Ga atoms with graphene is a standard feasible calculation. On the other hand, the calculation of Ga cluster interaction with graphene is much harder, because the individual building blocks (clusters) are bigger structures and cannot be easily made periodic. Therefore, this was the reason why only small clusters consisting of maximally three Ga atoms have been calculated. Hence, there is a question how the results of the experimental and computational part can be compared.

First, as for qualitative comparison, both the experimental and computational results are in good agreement. They show the Ga atoms n-dope graphene, and that there is a certain critical Ga concentration at which graphene is not more n-doped, and even the electrons start to be removed from graphene (return point in figure 1(a)—experiment, and figures 6(a), (c)—computation).

Second, in order to compare the computational and experimental results quantitatively, it is necessary to make a simple estimation of the Ga diffusion length. In case of the DFT calculation for two- and three-Ga atom clusters, the n-doping saturation appears already for three Ga atoms in a cluster which for our choice of computational cell corresponds to the Ga concentration $n_{\mathrm{Ga}} = 89 \times 10^{12}\,\mathrm{cm}^{-2}$. It can be assumed that three Ga atoms diffusing along the graphene surface at room temperature can form one uniform cluster only if they are inside of a circle area having a radius r comparable with the diffusion length (figure 7(d)). Then the radius can be easily estimated using the simple formula

$$r = \sqrt{3/(\pi \cdot n_{\mathrm{Ga}})} \cong 1\ \mathrm{nm}. \quad (1)$$

In case of the experimental results, the average radius of Ga islands $r \cong 2.2 \pm 0.6$ nm (figure 3) with respect to the nearest neighbors is proportional to the surface diffusion length, and is only about two times higher than predicted in DFT calculations. However, both the SEM and AFM images of clusters in figure 3 were taken at much higher Ga concentration $n_{\mathrm{Ga}} = 37.6 \times 10^{14}\,\mathrm{cm}^{-2}$ (~4 ML) to be able to see them on the surface at a given resolution. Therefore, the islands consist of a large number of Ga atoms and cannot be precisely compared with three Ga-atom clusters used in the DFT calculation.

The last way how to find the surface diffusion length is a combination of both, computational and experimental results. The calculation has proved the n-doping saturation starts at three Ga atoms in the cluster, and from the experimentally found return point in transport properties we know the Ga critical concentration is $n_{Ga} \cong 40 \times 10^{12}\,\mathrm{cm}^{-2}$ (figure 1(a)). Using the formula (1) the diffusion radius is $r \cong 1.5$ nm, which is in a good agreement with the calculated value of 1 nm. Moreover, the DFT calculation gives the answer to the question why the return of CNP was not observed in figure 1(a) at n_{Ga} $40 \times 10^{12}\,\mathrm{cm}^{-2}$. It is because the high level of n-doping and corresponding position of CNP equals to −250 V (figure 6(c)—right CNP axis) is still far outside the measurement range (±80 V).

The resolution of microscopic methods (AFM, SEM) we used for the mapping of initial stages of Ga growth on graphene was not sufficient to observe clusters smaller than about 1 nm and is not at all sufficient to observe the three-Ga atom clusters formation and give the direct evidence linking the DFT results for three atoms clusters with the AFM, SEM observation. On the other hand, in connection with the DFT results, especially with the conclusion that even formation of smaller Ga clusters can significantly reduce the level of n-doping, an indirect experimental proof in change of doping (return point in figure 1(a)) was introduced. From this point of view, the measurement of change in doping using transport measurement could be an interesting method for estimation of diffusion length.

Finally, let us summarize and compare our results with the results of other groups. The performed experiments and calculations prove Ga n-dopes graphene which is similar to n-doping caused by other metallic adsorbates such as Al, Ag, Cu [33, 35], and opposite to p-dopants like Au [29], Pt, water vapours [7] or to p-doping by a SiO_2 substrate. Moreover, the presented results show the n-doping saturation at a certain Ga concentration the exceeding of which leads to removal of electrons from graphene. Such an ambiguous effect was described in case of Au by Wu *et al* [43] who showed that gold in form of a continuous film p-doped the graphene while gold in form of isolated nanoparticles n-doped the graphene.

Many authors support their arguments on the type of doping by a simple comparison of the WFs of relevant metallic adsorbates and graphene, instead of DFT calculation. They directly assume the material with the lower WF with respect to graphene will n-dope graphene, or they incorporate a certain minimal WF difference that causes the electron transport (e.g. 0.9 eV) [33]. Such an approach can offer excellent results in case of large bulk volumes of materials, however, at small scales the significant discrepancies can appear due to material morphology, and inhomogeneity (effect of clusters). The bulk Ga WF being 4.2 eV [41, 63] is slightly lower than that one of graphene being reported in the interval 4.20–5.16 eV [64, 65]. It could explain the n-doping of graphene, but not the existence of the saturation point and removal of electrons in case of high Ga concentrations. These effects cannot be clarified without the DFT simulations similar to those in our paper.

The DFT calculations performed by different groups distinguish the weak and strong binding [33, 35] between graphene and adsorbed metals like Al, Ag, Au, Cu, Pt, and Co, Ni, Pd, respectively. In this works the minimum distance 3.41 Å from graphene for weakly bonded adsorbates, and the maximum distance 2.3 Å for the strong bonds were reported. These values are in agreement with our calculations when the strong bonds between individual Ga atoms and graphene result in the 2.2 Å distance between these atoms and graphene, the weaker bonds between small clusters and graphene in the 2.82 Å mutual distance, and the weakest ones in case of complete Ga layers to the 4.04 Å distance.

The surface diffusion and formation of small clusters is beside our SEM, AFM results and return point in the measurement of resistivity versus back-gate voltage dependency also supported by a low migration energy 0.03 eV estimated by Nishi *et al* [37], however, they used the DFT based on local density approximation. They also calculated the distance of the individual Ga atom from graphene 2.11 Å which is very close to the value of 2.2 Å obtained in our calculation.

Our work contributes to the explanation of fundamental principles of electronic properties of a Ga-graphene system which is essential for increasing the application potential of this system. Besides the simple tuning of the charge carrier density by Ga doping, important in electronics, our results are useful for other applications as well. For instance, gallium, being insoluble in graphene, is a suitable catalyst for graphene synthesis at the liquid–solid interface between Ga and amorphous carbon. It also enhances the graphene sensitivity and reactivity to different gases, e.g. neurotoxic hydrogen sulfide (H_2S) [66] and, finally, localized surface plasmon resonances in Ga nanoparticles can be tuned to increase almost 100 times surface-enhanced Raman scattering [41] from graphene.

6. Conclusion

The experiments and DFT calculations performed in this work prove that Ga atoms at low concentrations negatively dope the underlying CVD graphene. Simultaneously, it has been shown that n-doping level (i.e. electron concentration) grows with the gallium coverage until its maximum value is obtained at a specific value of gallium atom surface concentration. Exceeding such a surface concentration by the ongoing Ga deposition leads to a decrease in n-doping. The whole effect has been explained by means of DFT calculations showing the return point in doping is a direct consequence of weakening the graphene–Ga bonds (and strengthening the Ga–Ga bonds) during the formation of Ga clusters related to an exchange of electrons. We hypothesize the return point is a sign of formation of larger Ga clusters caused in the room temperature experiment by surface diffusion. The estimation of surface diffusion 1.5 nm from

transport measurement, 2.2 ± 0.6 nm from experimentally measured AFM, SEM data, and 1 nm from DFT calculations for small three-atom clusters are very comparable, supporting thus the proposed model of the real experimental behavior.

Acknowledgments

We acknowledge the support by the Grant Agency of the Czech Republic (grant No. 17-21413S and grant No. 15-21581S), Technology Agency of the Czech Republic (grant No. TE01020233 and grant No. TH01011284), European Regional Development Fund (project No. CZ. 1.05/1.1.00/02.0068), MEYS CR (project No. LQ1601—CEITEC 2020), and BUT (project No. FSI-S-14-2469). This work was also supported by The Ministry of Education, Youth and Sports from the Large Infrastructures for Research, Experimental Development and Innovations project 'IT4Innovations National Supercomputing Center—LM2015070'.

ORCID iDs

J Mach https://orcid.org/0000-0003-1896-0715
M Bartošík https://orcid.org/0000-0003-4706-9112
L Kormoš https://orcid.org/0000-0001-9099-4595

References

[1] Du X, Skachko I, Barker A and Andrei E Y 2008 *Nat. Nanotechnol.* **3** 491–5
[2] Bolotin K I, Sikes K J, Jiang Z, Klima M, Fudenberg G, Hone J, Kim P and Stormer H L 2008 *Solid State Commun.* **146** 351–5
[3] Castro Neto A H, Peres N M R, Novoselov K S and Geim A K 2009 *Rev. Mod. Phys.* **81** 109–62
[4] Goerbig M O 2011 *Rev. Mod. Phys.* **83** 1193–243
[5] Frank I W, Tanenbaum D M, van der Zande A M and McEuen P L 2007 *J. Vac. Sci. Technol.* B **25** 2558
[6] Lee C, Wei X, Kysar J W and Hone J 2008 *Science* **321** 385–8
[7] Bonaccorso F, Sun Z, Hasan T and Ferrari A C 2010 *Nat. Photon.* **4** 611–22
[8] Avouris P and Freitag M 2014 *IEEE J. Sel. Top. Quantum Electron.* **20** 72–83
[9] Liu H, Liu Y and Zhu D 2011 *J. Mater. Chem.* **21** 3335
[10] Chen S, Cai W, Chen D, Ren Y, Li X, Zhu Y, Kang J and Ruoff R S 2010 *New J. Phys.* **12** 125011
[11] Lee B, Chen Y, Duerr F, Mastrogiovanni D, Garfunkel E, Andrei E Y and Podzorov V 2010 *Nano Lett.* **10** 2427–32
[12] Kong X-K, Chen C-L and Chen Q-W 2014 *Chem. Soc. Rev.* **43** 2841–57
[13] Nouchi R and Tanigaki K 2015 *Appl. Phys. Lett.* **106** 083107
[14] Strasser C, Ludbrook B M, Levy G, Macdonald A J, Burke S A, Wehling T O, Kern K, Damascelli A and Ast C R 2015 *Nano Lett.* **15** 2825–9
[15] Chen J, Jang C, Xiao S, Ishigami M and Fuhrer M S 2008 *Nat. Nanotechnol.* **3** 206–9
[16] Nagashio K, Yamashita T, Nishimura T, Kita K and Toriumi A 2011 *J. Appl. Phys.* **110** 024513
[17] Dean C R *et al* 2010 *Nat. Nanotechnol.* **5** 722–6
[18] Yu L *et al* 2014 *Nano Lett.* **14** 3055–63
[19] Emtsev K V, Speck F, Seyller T, Ley L and Riley J D 2008 *Phys. Rev.* B **77** 1–10
[20] Li X *et al* 2009 *Science* **324** 1312–4
[21] Mattevi C, Kim H and Chhowalla M 2011 *J. Mater. Chem.* **21** 3324–34
[22] Batzill M 2012 *Surf. Sci. Rep.* **67** 83–115
[23] Zhang Y, Zhang L and Zhou C 2013 *Acc. Chem. Res.* **46** 2329–39
[24] Jauregui L A, Cao H, Wu W, Yu Q and Chen Y P 2011 *Solid State Commun.* **151** 1100–4
[25] Lherbier A, Dubois S M-M, Declerck X, Niquet Y-M, Roche S and Charlier J-C 2012 *Phys. Rev.* B **86** 75402
[26] Yazyev O V and Chen Y P 2014 *Nat. Nanotechnol.* **9** 755–67
[27] Pi K, McCreary K M, Bao W, Han W, Chiang Y F, Li Y, Tsai S W, Lau C N and Kawakami R K 2009 *Phys. Rev.* B **80** 1–5
[28] Blake P, Yang R, Morozov S V, Schedin F, Ponomarenko L A, Zhukov A A, Nair R R, Grigorieva I V, Novoselov K S and Geim A K 2009 *Solid State Commun.* **149** 1068–71
[29] Ren Y, Chen S, Cai W, Zhu Y, Zhu C and Ruoff R S 2010 *Appl. Phys. Lett.* **97** 053107
[30] Liu W, Wei J, Sun X and Yu H 2013 *Crystals* **3** 257–74
[31] Chen W, Qin S, Zhang X A, Zhang S, Fang J, Wang G, Wang C, Wang L and Chang S 2014 *Appl. Phys. Lett.* **104** 2012–6
[32] Bangert U and Zan R 2015 *Int. Mater. Rev.* **60** 133–49
[33] Giovannetti G, Khomyakov P A, Brocks G, Karpan V M, Van Den Brink J and Kelly P J 2008 *Phys. Rev. Lett.* **101** 26803
[34] Vanin M, Mortensen J J, Kelkkanen A K A, Garcia-Lastra J M J, Thygesen K S K and Jacobsen K W 2010 *Phys. Rev.* B **81** 81408
[35] Gong C, Lee G, Shan B, Vogel E M, Wallace R M and Cho K 2010 *J. Appl. Phys.* **108** 123711
[36] Xu Z and Buehler M J 2010 *J. Phys.: Condens. Matter* **22** 485301
[37] Nakada K and Ishii A 2011 *Solid State Commun.* **151** 13–6
[38] Xia F, Perebeinos V, Lin Y, Wu Y and Avouris P 2011 *Nat. Nanotechnol.* **6** 179–84
[39] Gong C, Hinojos D, Wang W, Nijem N, Shan B, Wallace R M, Cho K and Chabal Y J 2012 *ACS Nano* **6** 5381–7
[40] Silvestrelli P L and Ambrosetti A 2015 *Phys. Rev.* B **91** 1–9
[41] Losurdo M, Yi C, Suvorova A, Rubanov S, Kim T, Giangregorio M M, Jiao W, Bergmair I, Bruno G and Brown A S 2014 *ACS Nano* **8** 3031–41
[42] Giangregorio M M, Jiao W, Bianco G V, Capezzuto P, Brown A S, Bruno G and Losurdo M 2015 *Nanoscale* **7** 12868–77
[43] Wu Y *et al* 2012 *Small* **8** 3129–36
[44] Procházka P *et al* 2014 *Nanotechnology* **25** 185601
[45] Kresse G and Furthmüller J 1996 *Phys. Rev.* B **54** 11169–86
[46] Kresse G and Furthmuller J 1996 *Comput. Mater. Sci.* **6** 15–50
[47] Kresse G and Hafner J 1993 *Phys. Rev.* B **47** 558–61
[48] Blöchl P E 1994 *Phys. Rev.* B **50** 17953–79
[49] Kresse G 1999 *Phys. Rev.* B **59** 1758–75
[50] Perdew J P, Burke K and Ernzerhof M 1996 *Phys. Rev. Lett.* **77** 3865–8
[51] Monkhorst H J and Pack J D 1976 *Phys. Rev.* B **13** 5188–92
[52] Lafkioti M, Krauss B, Lohmann T, Zschieschang U, Klauk H, Klitzing K V and Smet J H 2010 *Nano Lett.* **10** 1149–53
[53] Ni Z H, Wang H M, Luo Z Q, Wang Y Y, Yu T, Wu Y H and Shen Z X 2010 *J. Raman Spectrosc.* **41** 479–83
[54] Pirkle A, Chan J, Venugopal A, Hinojos D, Magnuson C W, McDonnell S, Colombo L, Vogel E M, Ruoff R S and Wallace R M 2011 *Appl. Phys. Lett.* **99** 2–5
[55] Nomura K and MacDonald A H 2007 *Phys. Rev. Lett.* **98** 1–4
[56] Morozov S V, Novoselov K S, Katsnelson M I, Schedin F, Elias D C, Jaszczak J A and Geim A K 2008 *Phys. Rev. Lett.* **100** 11–4
[57] Hong X, Zou K and Zhu J 2009 *Phys. Rev.* B **80** 241415

[58] Huard B, Stander N, Sulpizio J A and Goldhaber-Gordon D 2008 *Phys. Rev.* B **78** 121402
[59] Barraza-Lopez S, Vanević M, Kindermann M and Chou M Y 2010 *Phys. Rev. Lett.* **104** 1–4
[60] Bai K K, Wei Y C, Qiao J, Bin, Li S Y, Yin L J, Yan W, Nie J C and He L 2015 *Phys. Rev.* B **92** 121405
[61] Song H S, Li S L, Miyazaki H, Sato S, Hayashi K, Yamada A, Yokoyama N and Tsukagoshi K 2012 *Sci. Rep.* **2** 337
[62] Mohiuddin T M G *et al* 2009 *Phys. Rev.* B **79** 205433
[63] Michaelson H B and Michaelson H B 2013 *J. Appl. Phhys.* **48** 4729–33
[64] Song S M, Park J K, Sul O J and Cho B J 2012 *Nanolett.* **12** 3887–92
[65] Liang S and Ang L K 2015 *Phys. Rev. Appl.* **12** 014002
[66] Sharma S and Verma A S 2013 *Physica* B **427** 12–6

4.3 Vysokoteplotní zdroje atomů žáruvzdorných materiálů (do 2 500 °C)

U těchto typů atomárních zdrojů jsou kladeny vysoké nároky na použitý materiál jak efuzní cely, tak topných těles i izolátorů. Tyto materiály musí nejen vydržet požadovanou vysokou teplotu, ale také by neměly reagovat s atomy svazku. Seznamy vhodných materiálů a jejich vlastnosti lze najít v literatuře [40]. Radiačním ohřevem pomocí molybdenové topné spirály lze dosáhnout teploty až 1 700 °C, a to v závislosti na hustotě navinutí drátu a kvalitě radiačního štítu. Při vyšších teplotách reaguje molybden i wolfram (1 700 °C) s keramikou Al_2O_3 tvořící izolaci. Jinou možností dosažení vysokých teplot (až 2 300 °C) je užití indukčního ohřevu [40], nebo využitím dopadu urychlených elektronů, viz část 4.2 a literatura [41].

Jako příklad zdroje atomů s ultra-vysokou pracovní teplotou uvádím zdroj atomů uhlíku, kde je využito k ohřevu kalíšku průchodu proudu sublimujícím materiálem (vláknem). Námi realizované vlákno bylo vyhotoveno z destičky HOPG (*High Oriented Pyrolytic Graphite*) pomocí elektroerozivního obrábění, viz obrázek 14b). Tímto vláknem, které je uloženo na uhlíkových kontaktech vyhotovených z pyrolytického grafitu (PG), protéká proud $I \approx 60$ A způsobující jeho ohřev až na sublimační teplotu 2 300 °C. 3D model uložení HOPG vlákna a fotografie realizovaného zdroje atomů uhlíku je zobrazen na obrázku 14a). Obecnou nevýhodou atomárních zdrojů získávajících svazky atomů používající k ohřevu materiálu žhavených vláken (iridiové, wolframové, tantalové, uhlíkové, …) je jejich relativně nízká intenzita svazku. Podrobný popis konstrukce a aplikace popsaného vysokoteplotního zdroje atomárních svazků lze nalézt v bakalářské práci [42]. Výše popsaný vysokoteplotní zdroj atomů, zkonstruovaný a využívaný na ÚFI FSI, je veden jako funkční vzorek VaV ID 113853 .

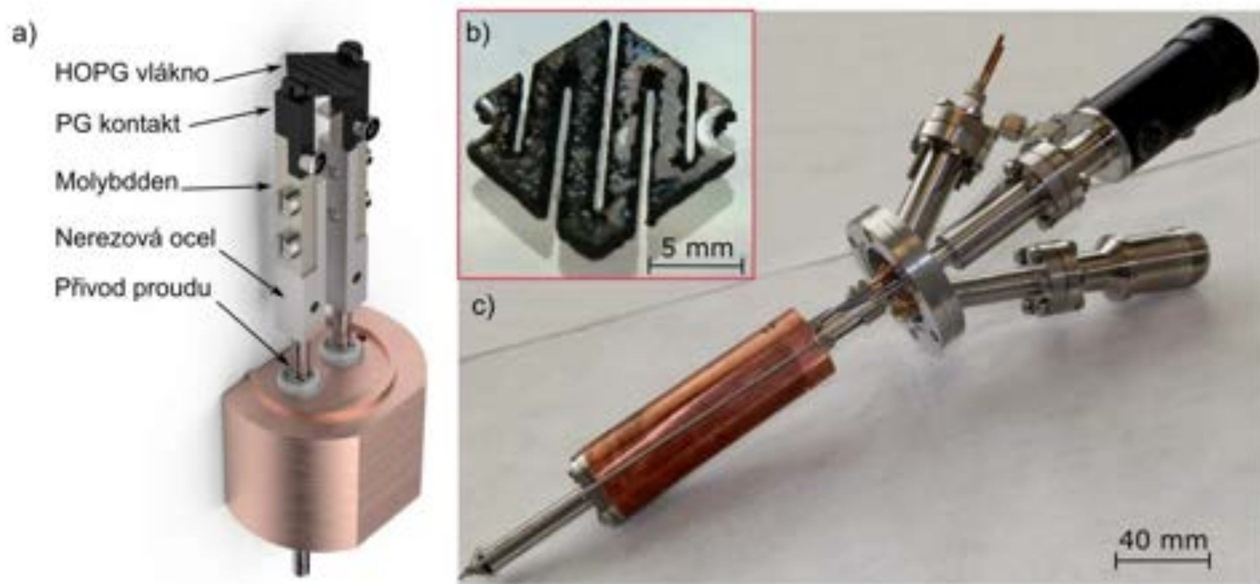

Obrázek 14: Sublimační zdroj svazků atomů uhlíku: a) 3D model uložení HOPG vlákna, b) fotografie vyrobeného HOPG vlákna připraveného pomocí elektroerozivního obrábění, c) fotografie realizovaného zdroje atomů uhlíku uchyceného na přírubě DN40. Zdroj je využíván na ÚFI FSI VUT v Brně k depozici grafenových vrstev v UHV (funkční vzorek VaV ID 113853).

Další realizovanou variantu zdroje s velmi vysokou pracovní teplotou je námi navržený, zkonstruovaný a otestovaný zdroj atomů uhlíku využívající ohřev vypařovaného materiálu dopadem fokusovaného svazku urychlených elektronů. V uváděném případě je kruhový HOPG terčík o průměru

10 mm usazen na molybdenovém držáku. Na tento držák je přiveden elektrický potenciál (≈ + 5 kV), který urychluje termoemisní elektrony ze žhaveného wolframového vlákna umístěného naproti terčíku. Mezi vláknem a HOPG terčem se nachází válcová elektroda sloužící k fokusaci elektronů do středu terče, viz schéma na obrázku 15a). Při této konfiguraci bylo dosaženo významného ohřevu středu HOPG terče, z kterého sublimovaly uhlíkové částice. Na obrázku 15b) je fotografie vnitřní části zdroje atomů uhlíku s kruhovým HOPG terčem, kde je patrné odpaření jeho centrální části. Jednou z nevýhod tohoto ohřevu je vznik parazitních iontů vlivem srážky urychlených elektronů s vypařovanými částicemi. Maximální energie těchto iontů je dána rozdílem potenciálů mezi kalíškem (terčem) a vzorkem. Tyto ionty mohou negativně ovlivnit vznik ultratenkých vrstev a nanostruktur. Z těchto důvodů je námi navržený zdroj vybaven decelerační elektrodou, která je umístěna u výstupu ze zdroje. Na ni přivedený elektrický potenciál (≈ + 5 kV) dokáže odfiltrovat zmíněné parazitní ionty. Na obrázku 15c) je fotografie realizovaného vysokoteplotního zdroje atomů uhlíku využívající k ohřevu fokusovaný svazek urychlených elektronů.

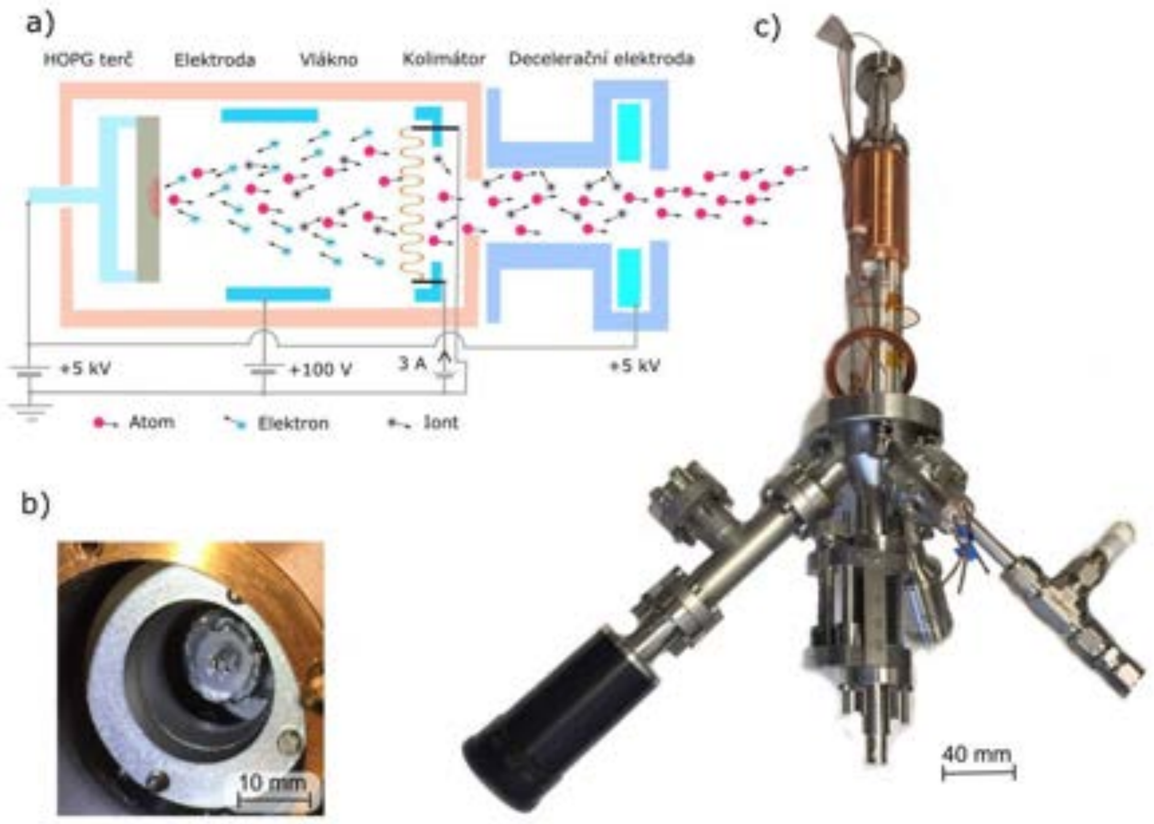

Obrázek 15: Zdroj atomů uhlíku využívající k ohřevu fokusovaný elektronový svazek, a) schematické uspořádání elektrod uvnitř zdroje, b) fotografie HOPG kruhového terče v centru lokálně odpařeného fokusovaným elektronovým svazkem, c) fotografie realizovaného zdroje vyvinutého na ÚFI FSI v Brně.

Výše dva uvedené zdroje atomů uhlíku jsou v současné době užívány studenty na Ústavu fyzikálního inženýrství, FSI VUT v Brně ke studiu růstu grafenu v UHV podmínkách. Navíc by měly být v budoucnu užity k řízenému dopování nanostrukturních materiálů, například GaN nanokrystalů. Podrobnější popis konstrukce a realizované experimenty užívající tyto zdroje nalezneme v závěrečných pracích studentů studijního oboru Fyzikální inženýrství a nanotechnologie [43–45].

4.3.1 Speciální zdroje atomů

Některé látky se za normálních podmínek v přírodě vyskytují v molekulární podobě (například H_2, O_2, N_2 a další). Pro získání atomárního svazku z těchto molekul je nutno provést nejprve jejich disociaci. Toho lze dosáhnout dodáním disociační energie molekule. Disociaci molekul lze realizovat například pomocí vysoké teploty (pyrolýza), světlem (fotolýza) nebo pomocí srážek elektronů v plazmatickém výboji. Další možností je využití katalytického rozkladu molekul během jejich dopadu na vhodný povrch trysky [46]. V mnoha chemických reakcích hrají právě atomy a radikály důležitou roli, a to kvůli jejich vysoké reaktivitě. Například atomy kyslíku mohou hrát důležitou roli jak při tvorbě oxidových ultratenkých vrstev (tzv. high-*k*) [47] tak i při nízkoteplotním čištění povrchů (obdobně se užívají atomy vodíku) [48]. Při nízkoteplotním čištění reagují atomy kyslíku s uhlíkovými nečistotami za tvorby plynného CO a CO_2, který desorbuje z povrchu. Svazky atomů disociovaných molekul nacházejí také perspektivní uplatnění při epitaxním růstu vrstev, kdy během současné depozice (pomocí jiných atomárních svazků) chemicky reagují a vytvářejí ultratenké vrstvy. Tyto reakce by za daných podmínek nenastávaly. Jako příklad lze uvést růst GaN polovodičových vrstev, při kterém se kombinují svazky atomů dusíku a atomů Ga.

Námi navržený a realizovaný zdroj atomů vodíku představuje zástupce zdrojů atomů využívající k disociaci princip pyrolýzy. V tomto případě je do žhavené wolframové kapiláry (2 000 °C) o vnitřním průměru 3 mm přiveden plyn molekulárního vodíku. Vlivem této vysoké teploty dochází při interakci molekul vodíku s horkým povrchem wolframové kapiláry k jejich disociaci. Uvedeným způsobem vzniklé atomy proudí efuzním tokem do UHV komory směrem na vzorek. Schematické uspořádání zdroje je uvedeno na obrázku 16. Žhavení kapiláry, na kterou je přivedeno vysoké napětí (2 kV), je realizováno dopadem urychlených termoemisních elektronů pocházejících ze žhaveného wolframového vlákna. Výměnou wolframové kapiláry za iridiovou lze přeměnit zařízení k produkci svazku atomů kyslíku.

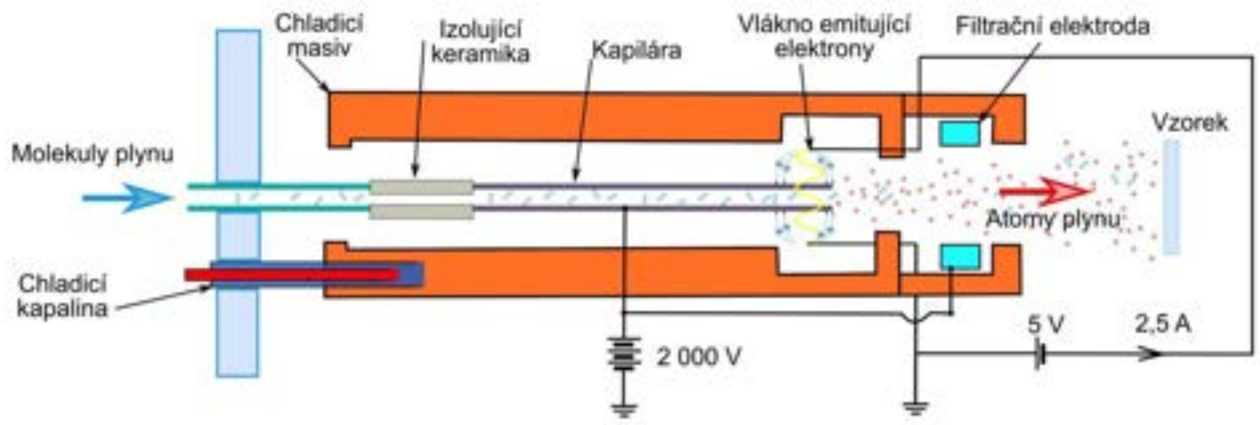

Obrázek 16: Schéma termálního disociačního zdroje atomů vodíku s wolframovou kapilárou, který je uzpůsoben pro užití v rastrovacích elektronových mikroskopech.

Uvedený termální disociační zdroj atomů vodíku je uzpůsoben pro užití v elektronových mikroskopech a je vybaven brzdnou (decelerační) elektrodou, která omezuje výstup parazitních iontů vznikajících při interakci atomů a molekul s elektrony. Fotografie uvedeného disociačního zdroje atomů, který je evidován jako funkční vzorek VaV ID 154978, a námi vyhotovené elektronické

ovládací jednotky je na obrázku 17. Podrobnější popis zapojení ovládací elektroniky lze nalézt bakalářské práci [49].

Obrázek 171: Fotografie realizovaného termálního disociačního zdroje atomů s elektronickou jednotkou. Zdroj je navržený pro přímé pozorování interakce atomů vodíku s materiály v rastrovacích elektronových mikroskopech (funkční vzorek VaV ID 154978).

K získávání intenzivních atomárních svazků lze využít vysokofrekvenčního (VF) plazmatu. Jako příklad uvádím námi navržený a realizovaný plazmový indukčně buzený VF zdroj atomů vodíku, kyslíku a dusíku, viz jeho 3D model na obrázku 18. Tento zdroj se skládá z PBN disociační komory, kolem které je navinuta měděná trubička sloužící jako cívka. Na tuto cívku je přiváděno VF napětí (13,56 MHz) o výkonu až 500 W, které uvnitř PBN disociační komory umožní vznik indukčně buzeného plazmatického výboje. V tomto výboji dochází k disociaci molekul, které následně proudí efuzním tokem přes multikolimátor (soustava mikrokanálků, viz obrázek 9) do komory směrem na vzorek. Během výboje měděnou dutou trubičkou (stočenou do tvaru cívky) proudí voda zajišťující odvod tepla z okolí výbojové komory. Mezi VF atomárním disociačním zdrojem a VF napěťovým generátorem je umístěna námi navržená vyrovnávací elektronická jednotka. Ta je složená ze dvou laditelných vysokonapěťových kondenzátorů, které slouží k vyrovnávání impedance mezi výbojovou komoru a generátorem (o dané impedanci $Z = 50\ \Omega$). Tím je zajišťováno dodávání maximálního výkonu do výbojové komory. Tlak plynu ve výbojové komoře je regulován UHV napouštěcím ventilem.

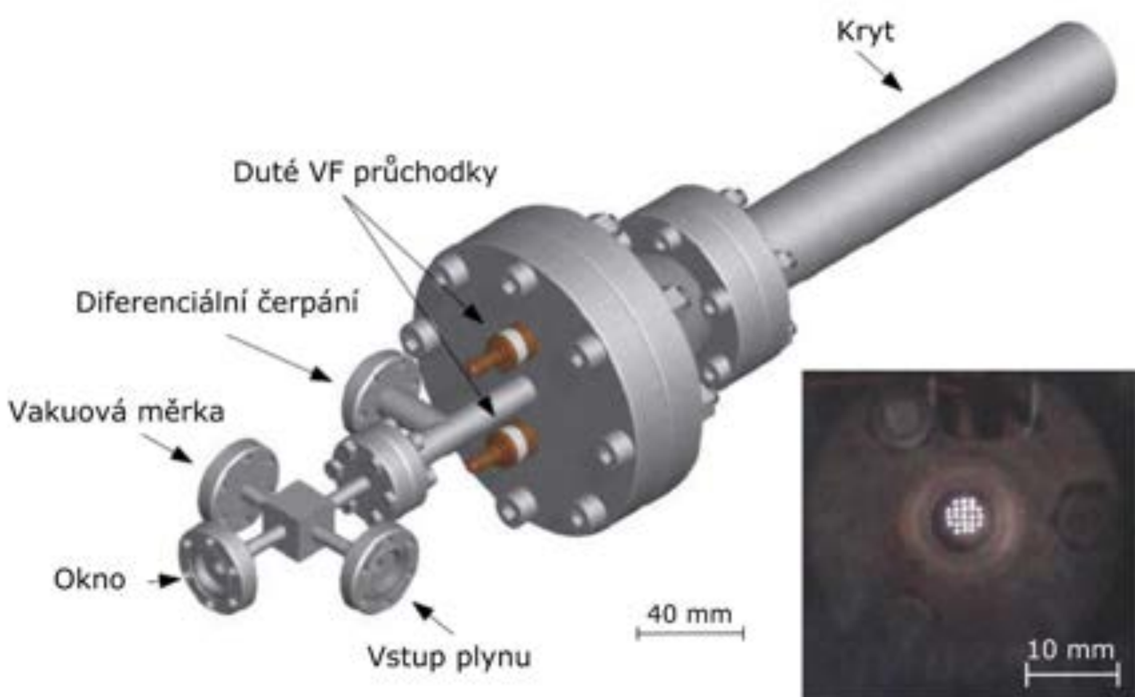

Obrázek 18: 3D model VF disociačního zdroje užívající k disociaci molekul indukčně vázané plasma. Ve výřezu je fotografie čela zdroje se zapáleným plazmatickým výbojem dusíkového plynu.

Námi navržená konstrukce umožňuje snímat optické spektrum plazmatu během jeho zažehnutí, čímž lze monitorovat zastoupení jednotlivých částic. Ukázka typických optických spekter během provozu VF disociačního atomárního zdroje pro jednotlivé plyny (vodík, kyslík a dusík) je na obrázku 19. Podrobnější popis konstrukce tohoto typu atomárního zdroje a konstrukce vyrovnávací jednotky je uveden v bakalářské práci [50].

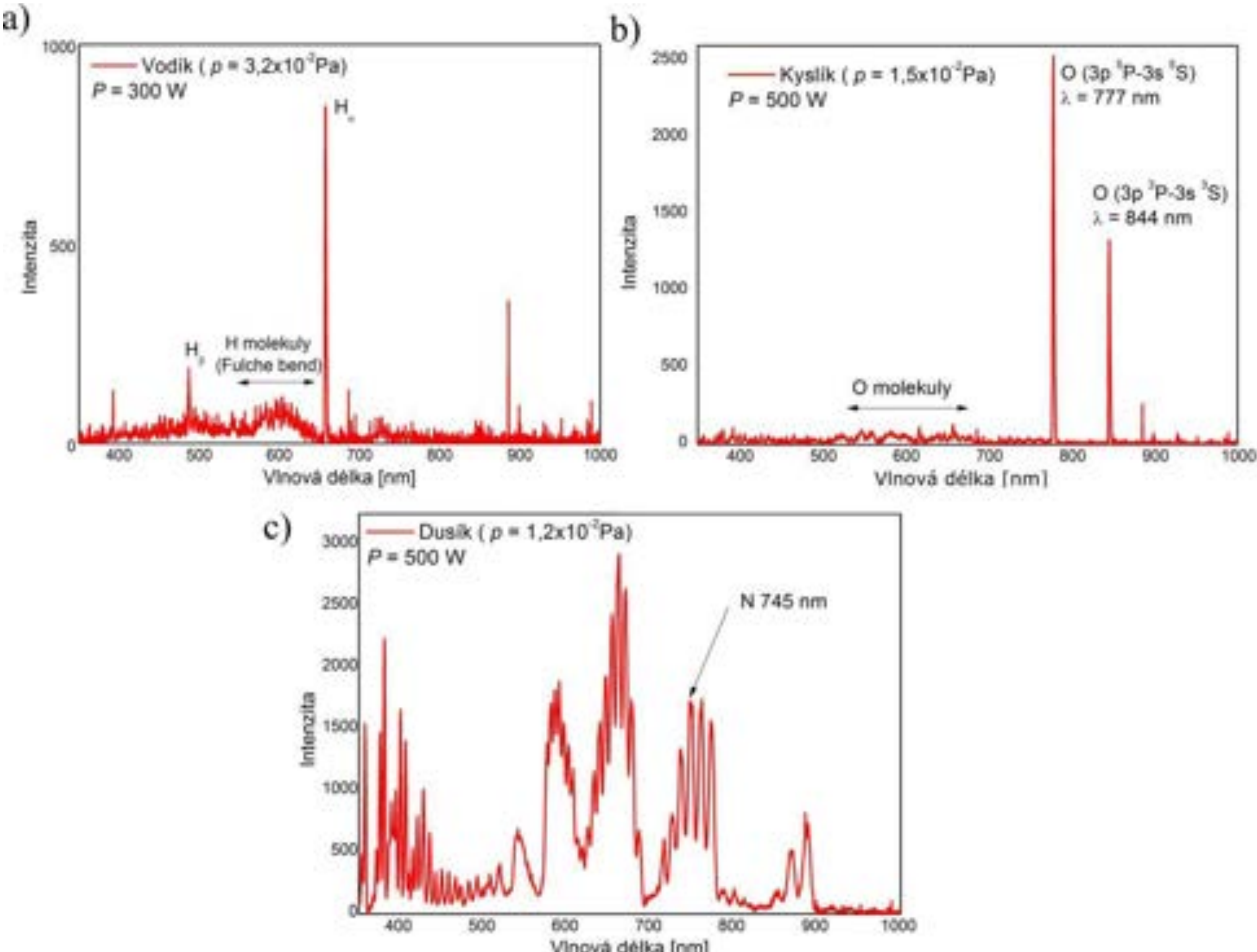

Obrázek 19: Ukázka optických spekter z VF plazmatického výboje pro plyny: a) vodík, b) kyslík, c) dusík.

5. Iontově-atomární svazkové zdroje

Výsledné vlastnosti ultratenkých vrstev a nanostrukturních materiálů deponovaných pomocí atomárních svazků lze do značné míry ovlivňovat souběžným tokem atomů a iontů na vzorek. Parametry asistujících iontů při růstu vrstvy (jejich energie, intenzita, úhel dopadu a druh) mají značný vliv na výsledné vlastnosti nanostruktur (zrnitost, morfologie,…). Zvýšená energie iontů může spouštět chemické reakce s povrchem, nebo s asistujícím atomárním svazkem, které by za daných podmínek vůbec nenastávaly. Za účelem studia vlivu dopadu iontů na růst GaN byly navrženy a sestaveny unikátní iontově-atomární zdroje poskytující svazky atomů Ga a iontů dusíku N_2^+. Základní uspořádání zdroje je obdobné jako u zdroje atomů s ohřevem pomocí dopadu urychlených termoemisních elektronů (část 4.2). Podstatný rozdíl je ale v umístění ionizační mřížky uvnitř zdroje, a to mezi wolframovým vláknem a kalíškem. Navíc je možno do vnitřní části zdroje napouštět plyn N_2 nebo Ar. Schéma uspořádání iontově-atomárního zdroje je zobrazeno na obrázku 20a). Wolframové vlákno, které je umístěno na plovoucím potenciálu (-50 V), je žhaveno průchodem proudu. Potenciál na ionizační mřížce (+50 V) urychluje termoemisní elektrony z povrchu vlákna směrem do prostoru ionizační mřížky. Jejich energie je zvolena tak, aby pravděpodobnost ionizace plynu byla maximální. Elektrony vystupující z ionizační mřížky na druhém konci jsou potenciálem kalíšku urychleny a při dopadu na kalíšek způsobují jeho ohřev, a to až na teplotu vypařování uvnitř umístěného materiálu (Ga). Vypařované atomy (Ga) proudí efuzním tokem zdrojem směrem na vzorek. V prostoru ionizační mřížky je určité množství těchto vypařovaných atomů spolu s molekulami (atomy) napouštěného plynu ionizováno srážkou s elektrony. Ionty vzniklé v prostoru ionizační mřížky se pohybují termálním pohybem, protože se nalézají v prostoru s konstantním potenciálem. Pokud se dostanou až k jejímu přednímu okraji, jsou vlivem rozdílného potenciálu na extrakční elektrodě urychleny ze zdroje směrem na vzorek a soustavou elektrod na vstupu do kolimátoru fokusovány. Tímto způsobem získáváme svazek složený převážně z atomů (Ga) a iontů (N_2^+). Intenzitu iontového svazku lze regulovat fokusací (defokusací) iontů a energii iontů změnou elektrického potenciálu (oproti uzemněnému vzorku) na ionizační mřížce.

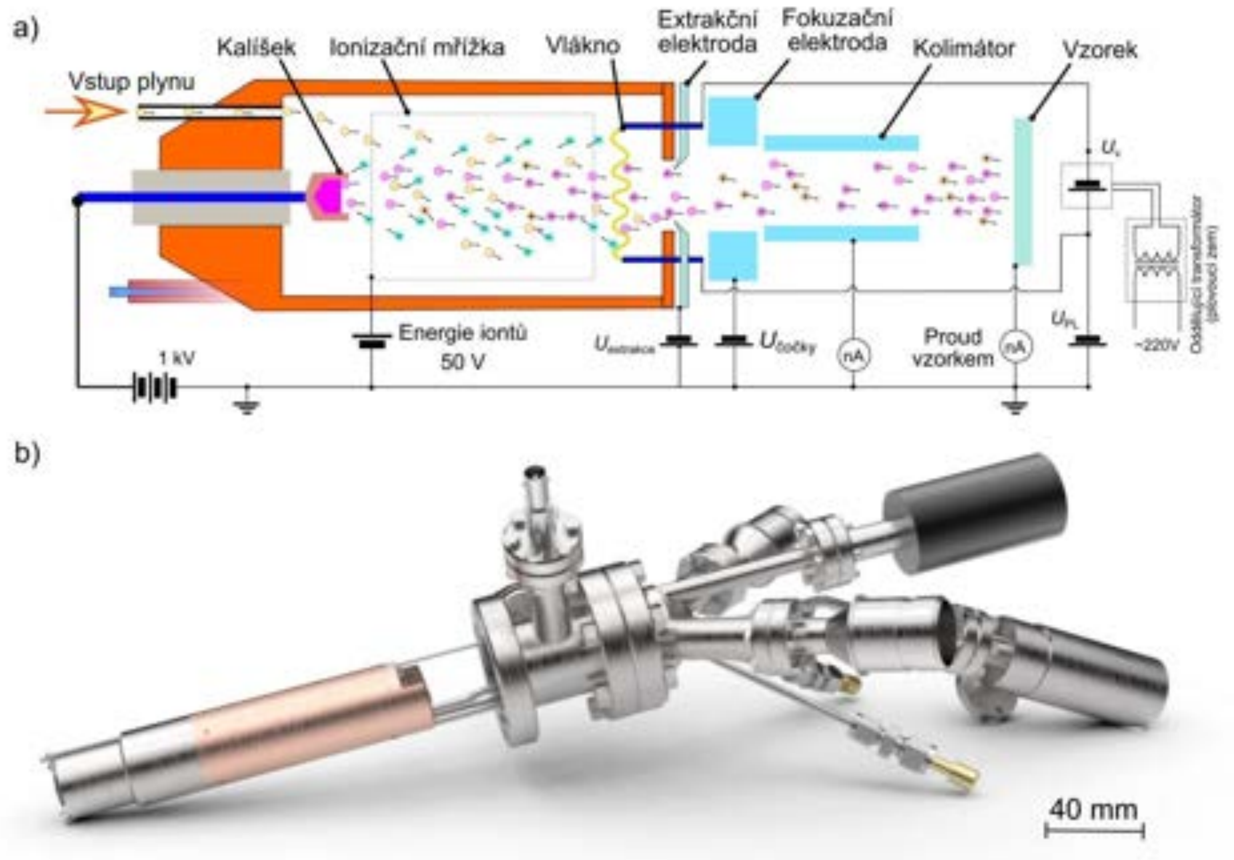

Obrázek 20: Iontově-atomární zdroj užívaný k růstu GaN ultratenkých vrstev a nanokrystalů, a) schematické uspořádání, b) 3D model (Patent 303867).

Popsané uspořádání iontově-atomárního zdroje umožní jeho provoz v následujících módech: i) efuzní cela, ii) iontový zdroj, iii) iontově-atomární zdroj. Podrobný popis konstrukce a funkce iontově-atomárního zdroje nalezneme v přiložených článcích v kapitolách 5.1.1 a **Chyba! Nenalezen zdroj odkazů.**.
V současné době je iontově-atomární zdroj aktivně užíván studenty ÚFI FSI VUT v Brně k růstu GaN ultratenkých vrstev a nanokrystalů za nízké teploty $T < 200$ °C, přičemž teplota růstu při komerčně užívaných CVD technologiích je cca 1 000 °C. Morfologie růstu GaN vrstvy závisí silně na poměru počtu atomů (Ga) ku počtu iontů (N_2^+) ve svazku. Ionty při dopadu na povrch vzorku reagují s atomy Ga a vytváří vazbu Ga-N. Takto vytvořený dimer Ga-N zůstává na místě (má velmi malou difuzi po povrchu) a vytváří tenkou vrstvu, zatímco samotné galium difunduje po povrchu snadno. Proto tedy Ga atomy, které nereagovaly s dopadajícími dusíkovými částicemi, migrují po povrchu a začnou tvořit ostrůvky Ga. Na takovýto ostrůvek dopadají ionty dusíku a reagují s Ga (vytváří Ga-N dimer). Tento Ga-N dimer snadno difunduje po povrchu Ga ostrůvku k povrchu substrátu, kde dochází k formování krystalů GaN. Schéma růstového procesu probíhajícího na povrchu substrátu při teplotě 200 °C během dopadu atomů Ga a iontů dusíku N_2^+ o energii 50 eV je zobrazeno na obrázku 21. Chceme-li získat hladkou vrstvu GaN, musí na povrch substrátu dopadat více iontů dusíku. Pokud chceme získat jen krystaly GaN, musíme nejprve narůst Ga ostrůvky a ty posléze vystavit iontům dusíku. Tato metoda přípravy nanokrystalů GaN se nazývá nízkoteplotní kapková epitaxe (*Low Temperature Droplet Epitaxy*). Opakovanou střídavou aplikací svazků atomů Ga a iontů dusíku lze „kultivovat“ tyto nanokrystaly a regulovat jejich velikost. Tohoto principu bylo využito k selektivnímu růstu

uspořádaných matic GaN nanokrystalů. Detaily výše popsaných principů a experimentů jsou podrobně popsány v přiloženém článku 5.1.3 a také v závěrečných pracích studentů ÚFI FSI VUT v Brně [10, 51–55].

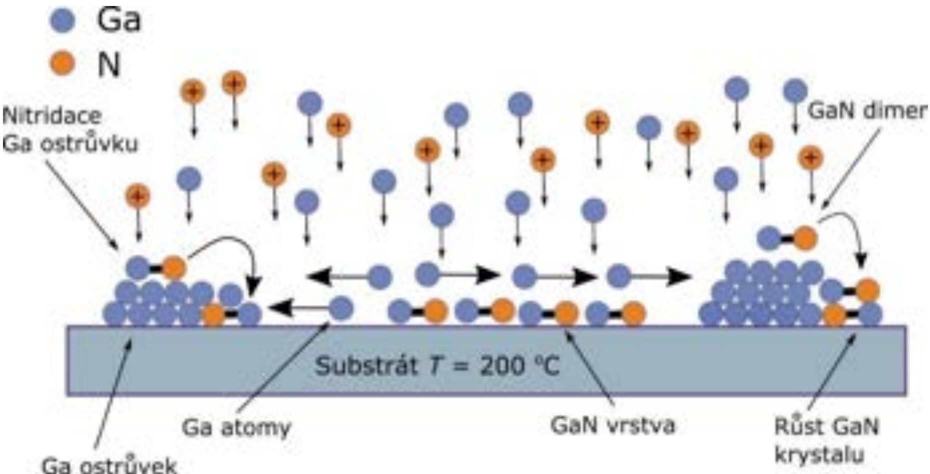

Obrázek 21: Schematické znázornění růstu GaN vrstvy při vyšší teplotě substrátu $T > 200$ °C. Tento proces je řízen rozdílnou difuzí GaN dimerů, Ga atomů a Ga ostrůvků po povrchu substrátu.

5.1.1 Článek č. 4 – Iontově-atomární svazkový zdroj s ultranízkou energií (30-200 eV) iontů pro depozici za asistence iontových svazků v ultravysokém vakuu

Autoři:

J. Mach, T. Šamořil, S. Voborný, M. Kolíbal, J. Zlámal, J. Spousta, L. Dittrichová a T. Šikola

Review of Scientific Instruments [online]. 2011, **82**(8), 083302. Dostupné z: doi: 10.1063/1.3622749.

Abstrakt:

Příspěvek popisuje návrh a konstrukci zdroje iontově-atomárního svazku s optimalizovaným generováním iontů pro depozici pomocí iontového svazku za podmínek ultravysokého vakua (UHV). Zdroj kombinuje efuzní celu a elektronově srážkový zdroj iontů a poskytuje svazky iontů o ultranízké energii v rozsahu od 30 eV do 200 eV. Snížení energie ionů na hypertermální hodnoty ($\approx 10^1$ eV) za optimalizovaných podmínek bylo dosaženo hlavně pomocí začlenění ionizační komory s dostatečně perforovanou mřížkou vhodnou pro elektronové a iontové svazky. Tímto způsobem byla řádově dosažena energie 10^1 eV a proudová hustota dusíkových iontů ve svazku 10^1 nA/cm^2. Zdroj je schopen zajistit růst ultratenkých vrstev nebo nanostruktur při ultranízkých energiích s rychlostí růstu několika ML/h. Zdroj iontově-atomárních svazků bude přednostně užíván k syntéze GaN v podmínkách UHV.

REVIEW OF SCIENTIFIC INSTRUMENTS 82, 083302 (2011)

An ultra-low energy (30–200 eV) ion-atomic beam source for ion-beam-assisted deposition in ultrahigh vacuum

Jindřich Mach,[1,2,a] Tomáš Šamořil,[1] Stanislav Voborný,[1] Miroslav Kolíbal,[1,2]
Jakub Zlámal,[1] Jiří Spousta,[1] Libuše Dittrichová,[1] and Tomáš Šikola[1,2]
[1]Institute of Physical Engineering, Brno University of Technology, Technická 2, 616 69 Brno, Czech Republic
[2]CEITEC BUT, Brno University of Technology, Technická 10, 61669 Brno, Czech Republic

(Received 31 January 2011; accepted 14 July 2011; published online 15 August 2011)

The paper describes the design and construction of an ion-atomic beam source with an optimized generation of ions for ion-beam-assisted deposition under ultrahigh vacuum (UHV) conditions. The source combines an effusion cell and an electron impact ion source and produces ion beams with ultra-low energies in the range from 30 eV to 200 eV. Decreasing ion beam energy to hyperthermal values ($\approx 10^1$ eV) without loosing optimum ionization conditions has been mainly achieved by the incorporation of an ionization chamber with a grid transparent enough for electron and ion beams. In this way the energy and current density of nitrogen ion beams in the order of 10^1 eV and 10^1 nA/cm^2, respectively, have been achieved. The source is capable of growing ultrathin layers or nanostructures at ultra-low energies with a growth rate of several MLs/h. The ion-atomic beam source will be preferentially applied for the synthesis of GaN under UHV conditions. © *2011 American Institute of Physics*. [doi:10.1063/1.3622749]

I. INTRODUCTION

During the last two decades ion beam assisted deposition[1,2] (IBAD) has become a powerful method for an improvement of properties of thin films including their ultrathin variants (less than 10 nm thick) and multilayers.[3] In this method, assisting ions simultaneously bombard the growing layers being deposited either by vacuum evaporation or sputtering. Generally, assisting ion beams bring an excess energy with respect to conventional evaporation and sputtering methods. Hence, they provide higher mobility of adatoms and non-equilibrium conditions of the film growth which leads to a modification of parameters of the resulting films. For instance, assisting ions were used for a better development of polycrystalline structures and imposing a preferential orientation of thin film grains,[4] improvement of surface smoothness of ultrathin film interfaces,[5] enhancement of in-plane magnetic anisotropy,[6] and low-temperature synthesis of materials not achievable by conventional near-equilibrium methods.[7,8] As an example of such a synthesis, low temperature GaN ultrathin films prepared by IBAD can be mentioned.[7] Contrary to the conventional synthesis of GaN thin films by metalorganic vapor phase epitaxy demanding as high temperatures as 1000 °C, the employment of assisting nitrogen ions (<200 eV) in the IBAD method enabled us to prepare these films at substrate temperatures below 500 °C.

To carry out IBAD a setup combining two devices is commonly used: an evaporator or sputtering facility for delivering atoms of a fundamental thin film material and an ion beam source providing assisting ion beams. This makes the method more complicated and expensive in comparison to single deposition methods as vacuum beam evaporation and sputtering deposition (using magnetron or ion beam source).

In Ref. 9, a commercially available gun generating both atomic and ion beams was reported. The gun is mounted on a single flange and its design is based on well known e-beam evaporators of the company Omicron. Availability of both atomic and ion beams makes it possible to carry out IBAD of ultrathin films by the single compact device. However, the energy of assisting ions was able to vary only from 700 eV to 900 eV. Such relatively high energies lead to local defects in growing layers and not to negligible resputtering of thin film atoms. In addition to that, electron-impact ionization was not optimized here as the electron energy was too high (hundreds of eV instead of ≈100 eV at which the ionization cross section is maximal) and so ion beam current densities provided by this gun were relatively small. In this paper we describe a similar ion-atomic beam source with an optimized generation of ions and enabling to decrease the ion beam energy to hyperthermal values without loosing optimum ionization conditions. In this way the ion beams of as low hyperthermal ion energy as 30 eV have been achieved. The ion-atomic beam source has been preferentially designed for the preparation of Ga and GaN thin films under UHV conditions.

II. PRINCIPLES OF THE ION-ATOMIC BEAM SOURCE

The ion-atomic beam source designed in our group is capable of modification of surfaces and deposition of ultrathin films under assistance of hyperthermal ions (<100 eV). Similar to the source described in Ref. 9, our source produces a mixture of atoms and ions and, hence, combines an effusion cell generating beams of thermal atoms and an electron-impact-ion beam source. Contrary to the source in Ref. 9 producing ions of a typical energy of 700–900 eV, our source generates ultra-low energy ion beams in the energy range from 30 eV to 200 eV. A schematic of the source is shown in Fig. 1.

[a]Author to whom correspondence should be addressed. Electronic mail: mach@fme.vutbr.cz.

 © 2011 American Institute of Physics

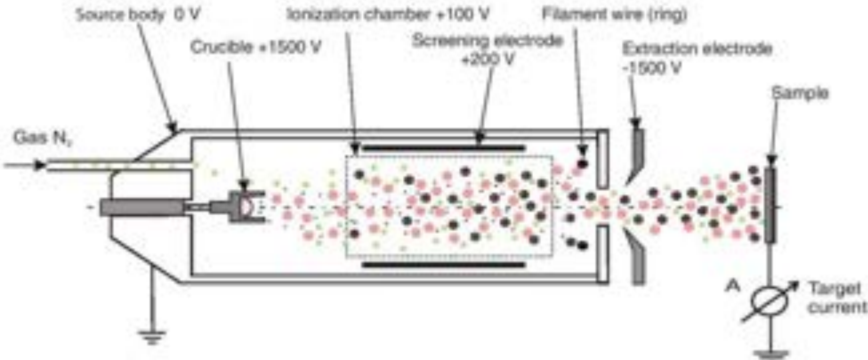

FIG. 1. (Color online) Schematic of the ion–atomic beam source generating beams of thermal atoms and ultra-low energy ions (30–200 eV). The potential setup provides ions of 100 eV energy at the target.

Electrons having initial energies 0.1–1 eV are emitted from a heated tungsten filament (resistive heating, $I_f = 2.6$ A) and accelerated by a voltage of ~100 V towards a grid forming walls of a cylindrical ionization chamber (an envelope of an ionizer), and consequently enter the ionization area. The stainless steel grid defines both a constant potential inside the ionization chamber and an acceleration voltage between the cathode filament being at a floating potential and the grid. In this way electrons can collide with neutral atoms inside the ionization chamber at a well defined energy optimized to the most effective ionization (i.e., the highest ionization cross section). According to Ref. 10, for most of inert gases, such an energy is close to 100 eV (see below). Additionally, the potential of the ionization chamber defines the energy of ions at the earthed target (ion energy at the target is defined by the potential difference between the place of ion creation and the target). This fact together with the floating potential of the filament makes it possible to change the target ion beam energy while keeping the electron energy close to 100 eV and, hence, to the most effective ionization conditions. The implementation of the ionization chamber having a potential defined by the grid and the floating potential of the cathode represents the most significant design features distinguishing our source from that one defined in Ref. 9.

Other electrons not interacting with atoms go through the grids of the ionization chamber and are post-accelerated towards the crucible being at the typical potential $U_c = 1000$ V (Fig. 1). In this way the crucible is heated by electron bombardment to a temperature sufficient for the evaporation of a material inside the crucible. The evaporated atoms having thermal energy (0.1–1 eV) pass through the grid of the ionization chamber by an effusion flow along straight trajectories towards the target. The gas is introduced into the source through an UHV valve, the pressure in the main chamber is commonly $p = 10^{-7}$–10^{-8} mbar. Ionized gas atoms together with the atoms evaporated from a crucible form the major constituents of the beam. The positive ions generated in the ionization chamber are extracted by an extraction electrode

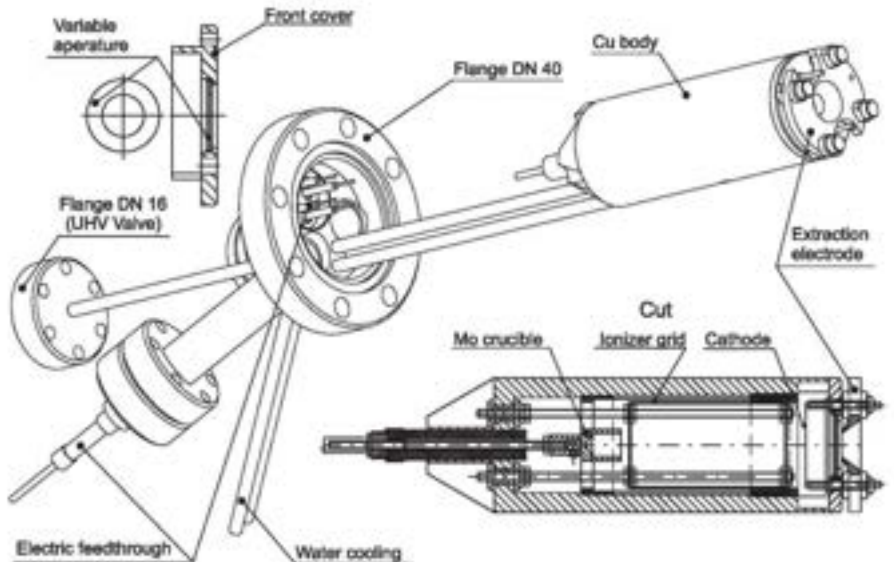

FIG. 2. 3D model of the ion-atomic beam source and the cross section of the source body.

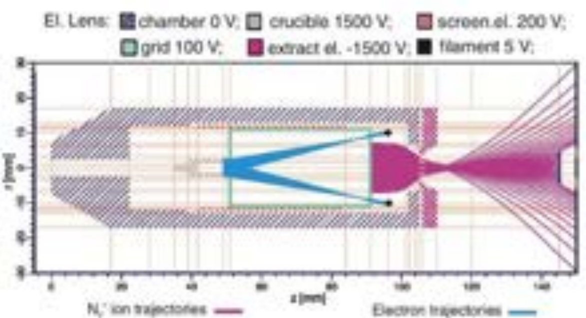

FIG. 3. (Color online) Trajectories of electrons and N_2^+ ions ($E_k \approx 100$ eV) inside the ion-atomic beam source simulated by the EOD simulation program (see Ref. 12).

being at a negative potential towards the earth. Additionally, the negative potential at the extraction electrode influences the profile of the ion beam.

III. DESIGN OF THE ION-ATOMIC BEAM SOURCE

The mechanical design of the source is shown via a 3D model and a cross section of the source in Fig. 2. The source body is made of free oxygen copper having high heat conductivity. The thickness of the body wall is 4 mm. The body is cooled down by water running through two cooling pipes fastening the body to a DN 40 CF flange simultaneously. All the electrical feedthroughs and a gas inlet tube are incorporated into this flange. The tube is terminated by a DN 16 CF flange for connecting a UHV dosing valve. The crucible is made of molybdenum and attached to a high voltage electrical feedthrough isolating it electrically from the body. The feedthrough can be moved along the longitudinal axes of the body in order to optimize the distance of the crucible from the grid wall of the ionization chamber (ionizer grid). This distance can be changed in the range of $\Delta l = 20$ mm.

The cylindrical ionizer grid is made of stainless steel and has the length $l = 40$ mm and diameter $\phi = 22$ mm. The grid mesh size is 1.5×1.5 mm^2. The grid is attached to an electrically isolated screw rod which enables to change its distance from the filament and thus to optimize the emission of electrons. Between the grid and the inner body wall an additional cylindrical electrode is inserted to better screen off the zero wall potential (grounded source body) and, thus, the relevant field which would penetrate through the mesh. The thoriated tungsten filament (diameter $\phi_{fil} = 0.150$ mm, active length $l = 60$ mm) is spot-welded to two special low voltage feedthroughs mounted to a front cover of the source body. The ion beam is extracted by an extraction electrode. To further modify the parameters of ion and atomic beams a variable aperture can be placed in front of the extraction electrode.

IV. EXPERIMENT

The ion-atomic beam source has been tested and optimized for the two distinct ultra-low ion energy ranges as follows.

A. 100 eV–200 eV ion beams

The energy of ions hitting the target is determined by a potential difference between the place of their origin (potential defined by the grid of the ionization chamber) and the target. The probability of ionization of atoms by an electron collision process depends on electron energy. In the case of Ar and N_2 the ionization cross sections have their maxima at about 100 eV.[10,11] The position of each functional part of the source was optimized by simulations of ion and electron trajectories using an EOD software package.[12] The corresponding trajectories of N_2^+ ions (starting from front grid) and electrons (between filament and crucible) are depicted in Fig. 3. In the simulations the starting positions of ions and electrons were defined at the front wall of the ionization chamber (with respect to the filament) and at the filament, respectively. The simulations revealed that the trajectories of electrons were strongly dependent on the filament position.

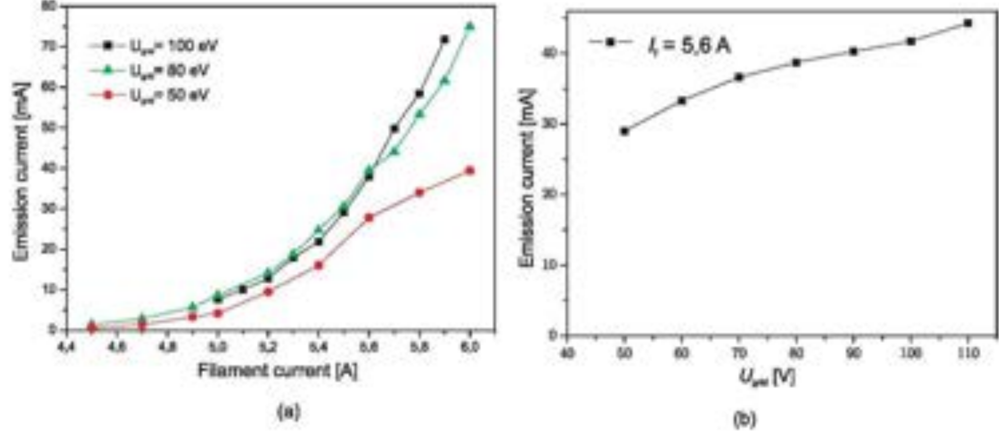

FIG. 4. (Color online) Dependence of the emission electron current on the filament current for different grid voltages (a), dependence of the emission electron current on the grid potential for the constant filament current $I_f = 5.6$ A (b). The potential of the crucible was kept zero.

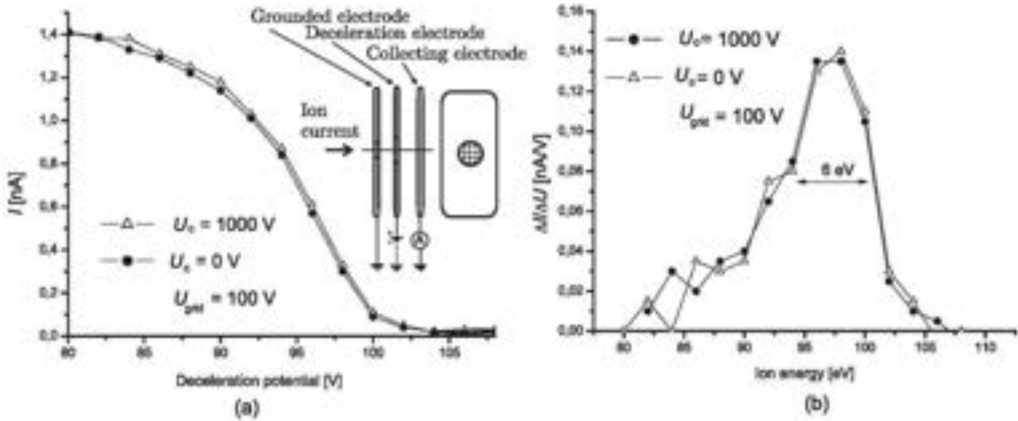

FIG. 5. Dependence of nitrogen ion-beam current on the potential of the deceleration electrode of a Faraday probe for $I_f = 5.6$ A, $U_{grid} = 100$ V, $U_{scr} = 100$ V and two different crucible potentials U_c (a), the resulting energy distribution of ions in the beam (b).

Consequently, the flux of electrons bombarding the crucible was significantly affected by the filament position as well. Depending on it, up to 20% of electrons emitted by the filament managed to pass through the ionizer grid and reached the crucible. Hence, the distance between the filament and the front wall of the grid has to be exactly adjusted.

The value of the emission electron current influences both the target ion current and the heating power delivered to the crucible. The experimental dependence of the emission current on the filament current (resistive heating) for different values of grid voltage and a work pressure of 5×10^{-7} Pa is shown in Fig. 4(a). The emission current goes down with the decreasing filament current and significantly with the grid voltage. Hence, to provide a reliable operation of the ion source the grid voltage should be 80 eV or higher, at optimum. The dependence of the emission electron current on the grid voltage for the same pressure as in the case of Fig. 4(a) and at a constant filament current of 5.6 A is shown in Fig. 4(b).

The properties of thin films strongly depend on the ion-to-atom arrival ratio and energy of ions. To measure both the ion beam current and the ion-beam energy a Faraday cup placed 150 mm far away from the source exit aperture was used.

The ion energy distribution was measured using a retarding field generated by a deceleration electrode of the Faraday cup put at a positive potential. The dependence of nitrogen ion-beam current on the potential of the deceleration electrode for an ion beam accelerated by a voltage of 100 V (U_{grid} = 100 V) and two different crucible potentials (U_c = 0 V and 1000 V) is shown in Fig. 5(a). The energy dispersion curve of nitrogen ions obtained by the derivative of this dependence according to the potential is shown in Fig. 5(b). The energy of the ion beam and the energy spread of its ions defined by the full-width at half maximum of the energy dispersion curve were ~100 eV and 6 eV, respectively, for both values of the crucible potential. Hence, the electrostatic field generated by the crucible is sufficiently screened off by the grid of the ionization chamber.

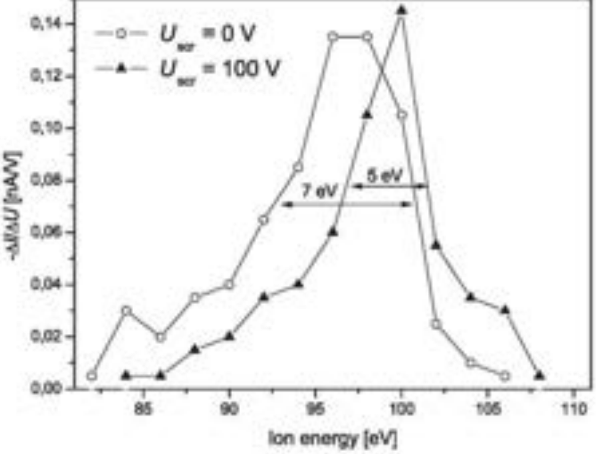

FIG. 6. Nitrogen-ion beam energy distribution for two different screening electrode potentials (U_{grid} = 100 V, U_c = 100 V).

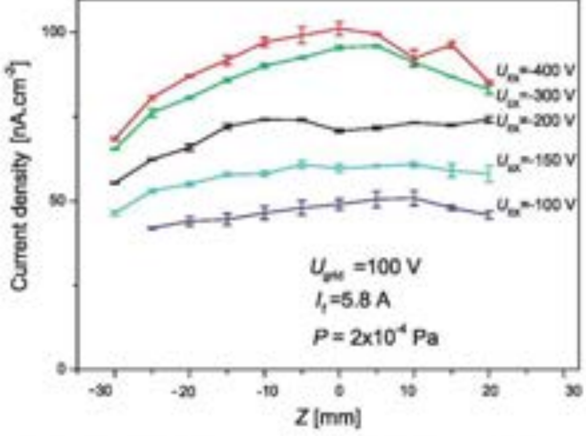

FIG. 7. (Color online) Current profiles of a 100 eV ion beam for different extraction electrode potentials, measured by a Faraday cup ($p_{N2} = 2 \times 10^{-4}$ Pa, ΔU = 100 V, I_f = 5.8 A, U_c = 400 V).

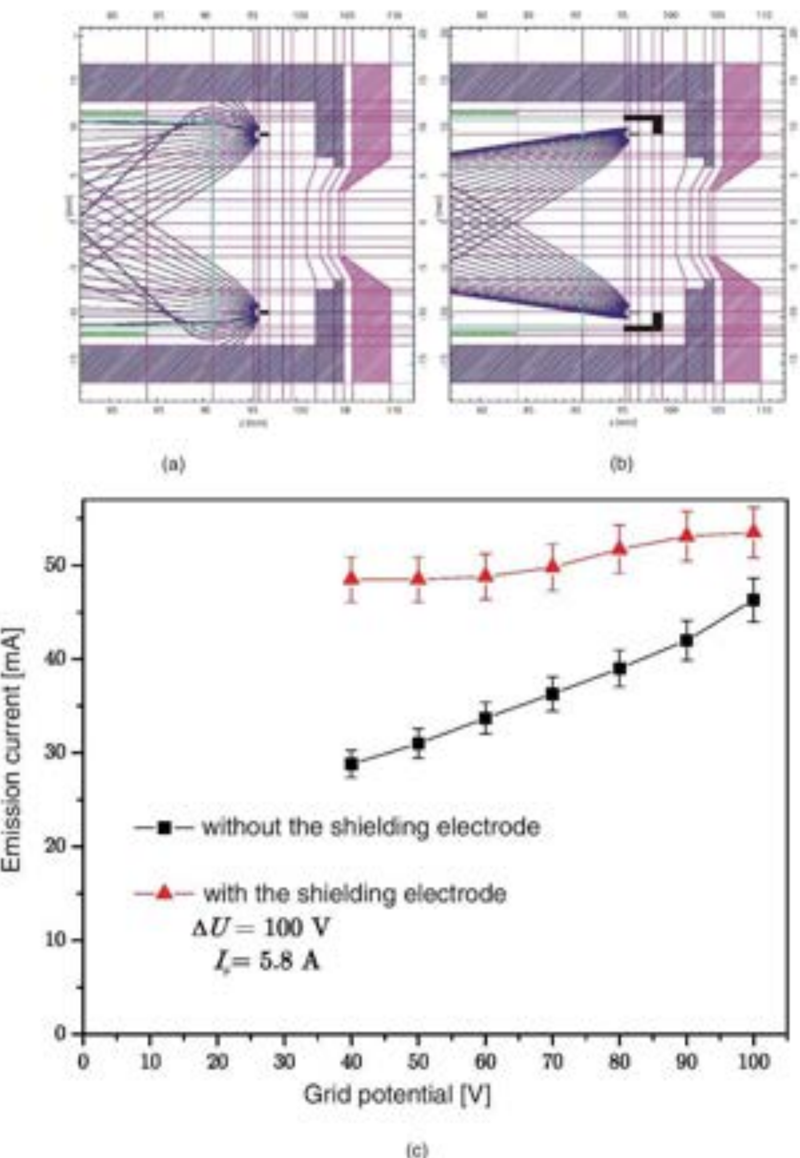

FIG. 8. (Color online) Simulated trajectories (EOD) of electrons emitted from the filament without (a) and with (b) the presence of the shielding electrode being set to the filament potential $U_f = -50$ V ($U_{grid} = 50$ V), (c) dependence of the emission electron current on the grid potential with (triangles) and without (squares) the shielding electrode at a potential of the filament for the constant grid-filament voltage difference $\Delta U = 100$ V.

The influence of the screening electrode potential on the energy of nitrogen-ion beam and its energy distribution is shown in Fig. 6. The lower energy of ions for $U_{scr} = 0$ V results from a decrease of the potential inside the ionization chamber due to the penetration of the electrostatic field through the grid towards the grounded source body. A wider energy spread of ions at zero voltage on the screening electrode (≈7 eV) is caused by a lower homogeneity of the field potential inside the ionization chamber than in the case of U_{scr} = 100 V.

The nitrogen ion beam profiles measured by the Faraday cup at a distance of 150 mm from the exit source aperture for an ion beam energy of 100 eV and different potentials on the extraction grid are shown in Fig. 7. The results revealed a strong divergence of the ion beam. To reduce it, a focusing electrode has to be installed yet.

B. Hyperthermal ion beams (<100 eV)

Due to resputtering processes and defect formation during ion beam assisted deposition the energy of assisting ions should be kept at specific lower energies for which these effects are limited, but assisting ions still bring enough excess energy. In practice, such energies correspond to a hyperthermal energy region, i.e., to the values below 100 eV.[9,10]

To provide such hyperthermal ion beams, the potential of the grid must be approximately kept at the same nominal values in volts as the required ion energy at a target in

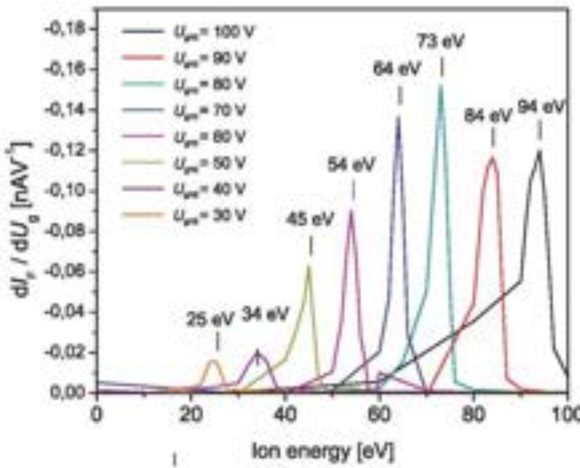

FIG. 9. (Color online) Energy distribution curves of nitrogen ions for different grid potentials determining the energy of ions and measured by a Faraday cup ($p_{N2} = 2 \times 10^{-4}$ Pa, $\Delta U = 100$ V, $I_f = 5.8$ A, $U_c = 400$ V).

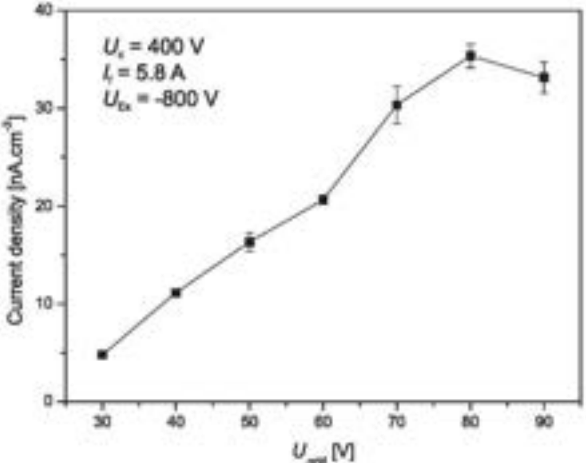

FIG. 10. Dependence of nitrogen ion-beam current density on the grid potential ($p_{N2} = 2 \times 10^{-4}$ Pa, $\Delta U = 100$ V).

electronvolts is planed, i.e., below 100 eV. Hence, to keep the energy of ionizing electrons at the most effective values ($\approx$100 eV), the filament must be electrically floating, so that its potential could be set to negative values with respect to ground, and thus the potential difference between the grid and the filament is kept at $\Delta U \approx 100$ eV. However, to screen off the grounded body of the source being positive towards the filament (and so attracting the electrons emitting from the filament), an additional shielding electrode around the filament had to be installed.

To demonstrate the effect of the shielding electrode the EOD simulations of electron trajectories emitted from the filament without and with the electrode are shown in Figs. 8(a) and 8(b), respectively, for $U_{grid} = 50$ V. The electrode, the potential of which was set to the value of the filament potential ($\approx$−50 V), prevents the electrons from hitting the body and promotes their aiming towards the grid and, consequently, to the crucible. In addition, the shielding electrode reduces the influence of the grid potential, determining the ion energy at the target, on the emission electron current as can be seen in Fig. 8(c).

The energy distribution curves of nitrogen ions measured by the same retarding field methods as mentioned above for different grid potentials (30–100 V) determining the energy of ions and for the constant grid-filament voltage $\Delta U = 100$ V are depicted in Fig. 9. The differences in nominal values between the grid potentials and the energies of peak maxima are caused by distinct potentials at the walls of the ionization chamber (grid) and inside this chamber.

The profiles of ultra-low energy nitrogen ion beams measured by the Faraday cup were of a similar broad shape as those shown in Fig. 7.

As expected, for the lowest ion-beam energies the ion beam current grows with the kinetic energy of ions.

Dependence of nitrogen ion-beam current density on the grid potential for specific values of operational parameters is shown in Fig. 10. The current density is in the order of tens of nA/cm^2 for energies not exceeding 100 eV. This corresponds to the flux densities of 10^{10}–10^{11} ions/cm^2 s. Compared to the typical atomic fluxes provided by the effusion of atoms from the crucible of our source (or other corresponding effusion cells of this size) these values are about 10^2-10^3 smaller. Hence, to use the ion-atomic beam source described in this paper for the ion-beam assisted deposition of nitrogen compounds (e.g., GaN), the source must be equipped with a focusing electrode providing higher current densities over the sample area ($\approx$1 cm^2). Supposing most of the ions would be focused by this electrode, the ion current density would increase in one order of magnitude, i.e., to 10^{11}–10^{12} ions/cm^2 s which makes it possible to grow ultrathin layers or nanostructures (e.g., nanodots) at ultra-low energies with a growth rate of several MLs/h.

V. CONCLUSION

An ion-atomic beam source with an optimized generation of ions and enabling decreasing ion beam energy to hyperthermal values ($\approx 10^1$ eV) has been designed. This has been mainly achieved by the incorporation of an ionization chamber, the grid walls of which are transparent enough for electron and ion beams. The optimal energy of electrons with respect to ionization efficiency is controlled by the voltage difference between the grid and the filament. As the potential of the grid determines the energy of the ion beam at the grounded target as well, the filament potential must be floating towards the earth. In this way the energy and current density of nitrogen ion beams of the order of 10^1 eV and 10^1 nA/cm^2, respectively, have been achieved. Supposing the source is equipped with a focusing electrode providing higher current densities over the sample, the growth of ultrathin layers or nanostructures at ultra-low energies with a growth rate of several ML/h is possible. The ion-atomic beam source will be preferentially applied for the deposition of Ga and GaN ultrathin films and nanostructures under UHV conditions.

ACKNOWLEDGMENTS

This work was supported by the research programmes of the Ministry of Education of the Czech Republic (Project Nos. MSM0021630508 and LC06040), GAAV (Project No. KAN400100701), MPO project (FR_TI2/736), the European Regional Development Fund - (CEITEC-CZ.1.05/1.100/02.0068). J. M. acknowledges the support of Vakuum Prague.

[1] J. M. E. Harpera, J. J. Cuomo, R. J. Gambinoa, and H. R. Kaufman, Nucl. Instrum. Methods Phys. Res. B **7-8**(2), 886 (1985).
[2] B. Rauschenbach, Vacuum **69**, 3 (2003).
[3] J. C. van der Linden, L. J Seijbel, and B. J Thijsse, Nucl. Instrum. Methods Phys. Res. B **148**(1-4), 98 (1999).
[4] L. Alberts, R. Leutenecker, and G. K. Wolf, Surf. Coat. Technol. **84**(1-3), 443 (1996).
[5] X. W. Zhou and H. N. G. Wadley, Surf. Sci. **487**, 159 (2001).
[6] T. Šikola, J. Spousta, L. Dittrichová, M. Stránský, J. Zlámal, F. Matějka, A. Nebojsa, J. Zemek, V. Peřina, D. Rafaja, and L. Ranno, Nucl. Instrum. Methods Phys. Res. B **148**(1-3), 907 (1999).
[7] S. Voborný, M. Kolíbal, J. Mach, J. Čechal, P Bábor, S Průša, J. Spousta, and T. Šikola, Thin Solid Films **459**(1-2), 17 (2004).
[8] J. W. Gerlach, S. Sienz, W. Attenberger, and B. Rauschenbach, Physica B **308-310** 81 (2001).
[9] J. Kirschner, H. Engelhard, and D. Hartung, Rev. Sci. Instrum. **73**(11), 3853 (2002).
[10] J. T. Tate and P. T. Smith, Phys. Rev. **39**, 270 (1939).
[11] M. J. Seaton, Phys. Rev. **113**, 814 (1959).
[12] B. Lencová and J. Zlámal, Phys. Procedia **1**, 315 (2008).

5.1.2 Článek č. 5 – Optimalizace iontově-atomárního zdroje pro depozici GaN ultratenkých vrstev

Autoři:

J. Mach, T. Šamořil, S. Voborný, M. Kolíbal, J. Zlámal, S. Voborný, M. Bartošík a T. Šikola

Review of Scientific Instruments [online]. 2011, **82**(8), 083302. Dostupné z: doi: 10.1063/1.3622749.

Abstrakt:

V článku je popisovaná optimalizace a aplikace iontově-atomárního svazkového zdroje určeného pro depozici ultratenkých vrstev v ultravysokém vakuu. Zařízení kombinuje efuzní celu a elektronově srážkový iontový zdroj a vytváří iontové svazky s velmi nízkou energií (20–200 eV) a současně produkuje termální atomární svazky. Zdroj byl vybaven systémem fokusačních elektrostatických elektrod zvyšující maximální hustotu proudu iontů dusíku ve svazku o průměru cca 15 mm o jeden řád ($j \approx 1\,000$ nA/cm^2). Bylo úspěšně dosaženo růstu ultratenkých GaN vrstev na substrátu Si(111) 7×7 při různých časech a při teplotách výrazně nižších (RT, 300 °C) než je užívaná v konvenčních technologiích jako je metalorganické chemické depozice z plynné fáze (≈ 1000 °C). Chemické složení těchto vrstev bylo charakterizováno *in-situ* rentgenovou fotoelektronovou spektroskopií a morfologie *ex-situ* pomocí rastrovací elektronové mikroskopie. Ukázalo se, že morfologie vrstev GaN silně závisí na relativní koncentraci vazby Ga-N ve vrstvách.

REVIEW OF SCIENTIFIC INSTRUMENTS 85, 083302 (2014)

Optimization of ion-atomic beam source for deposition of GaN ultrathin films

Jindřich Mach,[1,2,a)] Tomáš Šamořil,[1] Miroslav Kolíbal,[1,2] Jakub Zlámal,[1,2] Stanislav Voborny,[1,2] Miroslav Bartošík,[1,2] and Tomáš Šikola[1,2]
[1]*Institute of Physical Engineering, Brno University of Technology, Technická 2, 616 69 Brno, Czech Republic*
[2]*CEITEC BUT, Brno University of Technology, Technická 10, 61669 Brno, Czech Republic*

(Received 10 May 2014; accepted 26 July 2014; published online 14 August 2014)

We describe the optimization and application of an ion-atomic beam source for ion-beam-assisted deposition of ultrathin films in ultrahigh vacuum. The device combines an effusion cell and electron-impact ion beam source to produce ultra-low energy (20–200 eV) ion beams and thermal atomic beams simultaneously. The source was equipped with a focusing system of electrostatic electrodes increasing the maximum nitrogen ion current density in the beam of a diameter of ≈15 mm by one order of magnitude ($j \approx 1000$ nA/cm^2). Hence, a successful growth of GaN ultrathin films on Si(111) 7 × 7 substrate surfaces at reasonable times and temperatures significantly lower (RT, 300 °C) than in conventional metalorganic chemical vapor deposition technologies (≈1000 °C) was achieved. The chemical composition of these films was characterized *in situ* by X-ray Photoelectron Spectroscopy and morphology *ex situ* using Scanning Electron Microscopy. It has been shown that the morphology of GaN layers strongly depends on the relative Ga-N bond concentration in the layers. © *2014 AIP Publishing LLC*. [http://dx.doi.org/10.1063/1.4892800]

INTRODUCTION

GaN is an attractive material for semiconductor industry. This material belongs to one of the most important semiconductors for microelectronic and optoelectronic applications because of its excellent electrical properties such as a wide direct band gap, high electron saturation velocity, high break down voltage, etc.[1,2] It has been widely used in applications of light emitting devices operating in the blue and ultraviolet (UV) spectral region[3] and solar cells because of its direct band gap. Further, high voltage diodes and switching transistors based on wide band gap materials belong to strategic devices due to their applications in the field of power electronics used for instance in automotive industry, including electric vehicles, where an improved efficiency in energy conversion is a fundamental requirement.[4,5]

Recently, the attention has been paid to the synthesis of GaN nanostructures such as nanowires and nanocrystals.[6] In contrast to 2D planar structures, GaN nanowires and nanocrystals are loosely attached to substrates and, therefore, less affected by the lattice-mismatch. The GaN 2D planar nanostructures have been commonly prepared using metalorganic vapour phase epitaxy (MOVPE) at about 1000 °C. However, such a high temperature growth induces residual strains in the grown structures being detrimental to their properties. As an alternative method for fabrication of 1D-0D GaN nanostructures, a low temperature (400–800 °C) post-nitridation of Ga droplets by nitrogen plasma source was reported.[7–12] Another possibility for low temperature preparation of GaN thin films and nanocrystals is the ion beam assisted deposition IBAD (sometimes called IBA-MBE).[13–15] Due to an excess of the energy delivered by ions to the substrate, this method can improve the adhesion of the grown structures and lead to the synthesis of compounds and various metastable phases at temperatures substantially lower than in conventional methods.

In IBAD, it is generally necessary to combine and synchronize two distinct devices: an ion beam source and an atomic beam source. In this paper, we report on an optimization of a home-built ion-atomic beam source[16] for preparation of GaN ultrathin films and related 1D-0D nanostructures. The source produces both a thermal atomic beam of Ga and an ultra-low energy (20–200 eV) nitrogen ion beam. Compared to other techniques, it is in principle easier to control GaN film thickness, GaN nanocrystal size and density, and composition of these structures by this source, as the flux of Ga atoms and nitrogen ions can be simply and independently varied. In the paper the ability of the source to be used for preparation of ultrathin films of GaN at room- and low-deposition substrate temperatures will be demonstrated.

EXPERIMENTAL

The experiments were performed in a complex UHV apparatus[15] enabling *in situ* analysis of GaN chemical composition by X-ray photoelectron spectroscopy (XPS) without exposure of the films to ambient atmosphere. XPS was performed by an experimental setup consisting of DAR400 X-ray source and a hemispherical electrostatic analyser EA125 (both Omicron). All the measurements were carried out at room temperature using Mg Kα radiation and the pressure during the measurement was better than 7×10^{-7} Pa. The morphology and topography of the samples was observed by a Scanning Electron Microscopy (SEM) microscope (TESCAN LYRA). The samples having a size of 10 × 15 mm^2 were cut from a Si(111) wafer doped by phosphorus (specific resistivity 0.029–0.030 Ω cm). Subsequently, they were transferred into the complex UHV apparatus with the base pressure

a)mach@fme.vutbr.cz

 © 2014 AIP Publishing LLC

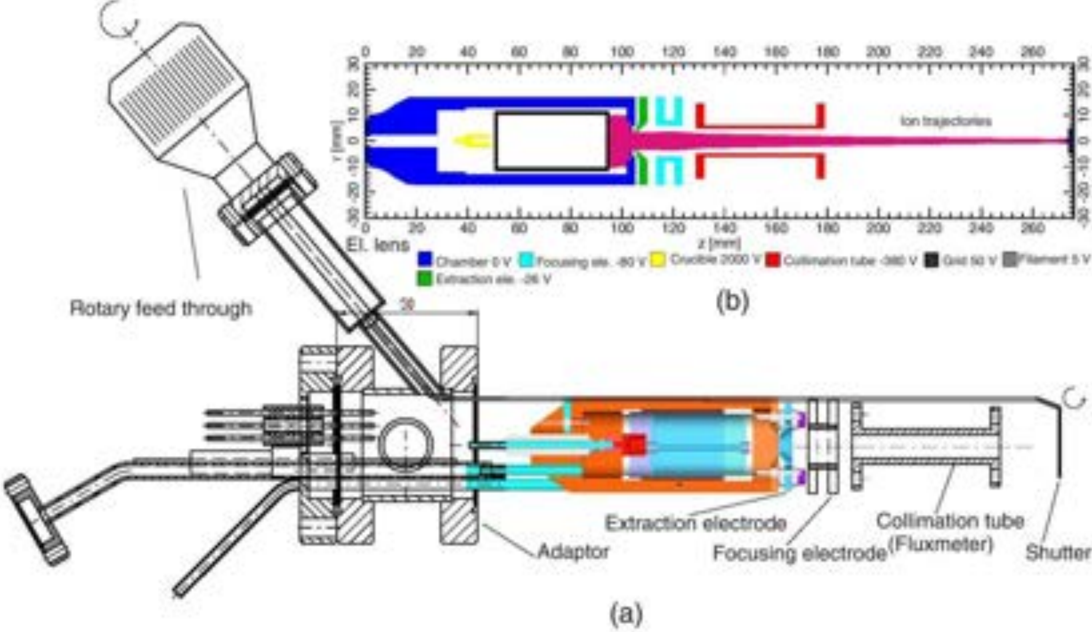

FIG. 1. Design of the ion-atomic beam source: (a) cross section and (b) simulation of nitrogen ion trajectories (in pink) by the EOD 213 software package.[17]

3×10^{-8} Pa and thermally flashed by direct resistive heating up to 1250 °C (1–2 min in total) to provide the surface with the Si(111) 7 × 7 reconstruction. The structure and cleanness of the substrate was checked *in situ* by low-energy-electron diffraction (LEED) and XPS, respectively.

The substrates were exposed to nitrogen ion- and gallium atom-beams produced by the home-made ion-atomic beam source being 13 cm away from the sample. It combines both an effusion cell and electron impact ion-beam source, as can be seen in Fig. 1. The construction details of the source were described in Ref. 16. In the source high purity (99.9999%) nitrogen gas (N_2) was used to generate ultra-low energy ion beams (20–200 eV). Thermal energy Ga atoms were evaporated from a PBN boat inside a Mo crucible.

The ion-atomic beam source can be operated in three different modes to provide: (1) the beam of thermal Ga neutral atoms (suppression of ions), (2) pulsed or continuous beam of ultra-low energy nitrogen (altern. noble gas) ions, and (3) simultaneous generation of Ga atom- and nitrogen ion-beams (simultaneous operation in the 1st and 2nd modes). In the last hybrid mode an enhanced fraction (≈1%) of ionised ultra-low energy Ga atoms in the beam is present as well. The work pressure in the deposition chamber measured by an ion gauge was $p_{N2} = 3 \times 10^{-5}$ Pa. The temperature of the substrate was measured by an optical pyrometer (emissivity set to 0.7).

The optimization of this ion-atomic beam source for the deposition of GaN thin films is discussed below. The typical thickness of these films was about 2 nm (growth rate 2 nm/h), therefore we refer to them as to GaN ultrathin films.

OPTIMIZATION OF THE ION-ATOMIC BEAM SOURCE

The ion-atomic beam source is generally capable of modifying the surfaces and depositing ultrathin films and nanostructures. The source can produce a mixture of thermal Ga atoms and nitrogen ions of an optimum energy. However, before the optimization the ion beam was too wide and its ion current density too low for technology applications. The nitrogen ion-beam current density measured by a Faraday cup for ion beams of the energy $E = 50$ eV was 35 nA/cm^2 as described in Ref. 16. To increase the ion current density, two electrostatic electrodes were designed and implemented into the front area of this source (Fig. 1(a)). The first electrode acts as a focusing electrode and the second one as a collimation tube.

The electrostatic potential at this tube is able to affect the trajectories of the positive ions leaving the source, while simultaneously the neutral atoms are collimated by tube geometrical restrictions. The ion beam current measured at the collimation electrode can be used as a flux monitor of atoms generated by the effusion cell. Additionally, the source was equipped by an adapter with a shutter. The position of each functional part of the source was optimized by simulations of ion trajectories using an EOD software package.[17] The trajectories corresponding to nitrogen ions are depicted in Fig. 1(b). In the simulation the starting positions of all ions were defined at the front wall of the ionizer grid. The simulations revealed that the trajectories of ions were strongly dependent on the potential of electrodes. As an example, two ion-beam current density profiles for different voltage settings on electrostatic electrodes are shown in Fig. 2. Compared to the source without the focusing electrostatic optics,[14] the optimized source provides by more than one order of magnitudes higher maximum of the ion current density ($j \approx 1000$ nA/cm^2), at least.

Room temperature deposition of GaN on Si(111)

First, the optimized ion-atomic beam source was applied for the growth of ultrathin GaN films at room temperature. After the flash annealing procedure the Si(111) 7 × 7

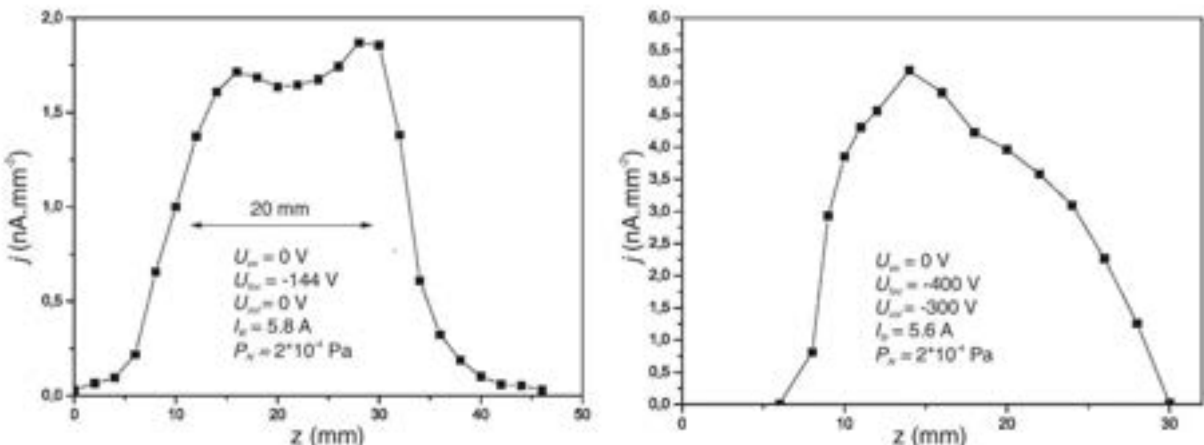

FIG. 2. Nitrogen ion-beam current density profiles measured by a Faraday cup and obtained for specific potential settings of electrostatic lenses and 50 eV ion beam energy. Legend: U_{ex} – extraction electrode voltage, U_{foc} – focusing electrode voltage, U_{col} – collimation tube voltage, I_{fil} – filament current, detection area of the Faraday cup is $A = 0.8$ mm^2.

substrates were cooled down to room temperature and then the deposition started. The flux of Ga atoms was primarily controlled by the power applied to the crucible. It was found that the electron current collected by the crucible was increasing with the growing nitrogen pressure inside the ion-atomic beam source. This increase can be explained by the contribution of secondary electrons being emitted upon collisions of nitrogen ions with the walls of the ionization chamber. For the GaN deposition two different energies of nitrogen ions (100 eV and 50 eV) were used. During the deposition assisted with 100 eV nitrogen ions resputtering of the deposited GaN layer atoms by these ions was observed. This effect was significantly reduced by using 50 eV assisting nitrogen ions. The XPS spectra corresponding to both kinds of ultrathin films are shown in Fig. 3, where the significantly different Ga $2p_{3/2}$/Si 2p intensity peak ratios are evident.

The chemical composition of GaN films was determined by fitting the Ga $2p_{3/2}$ peak. The spectral peak corresponding to the sample prepared using the ion-atomic beam source without the electrostatic optics, together with its components (sub-peaks), is shown in Fig. 4(a). The same is shown in Fig. 4(b) for the optimized source. Due to the higher current density of nitrogen ions ($\approx$1000 nA cm^{-2}) provided by the electrostatic electrodes of this source the relative number of Ga-N bonds in the GaN film characterized by the Ga-N subpeak increased from an original value of 15%, obtained for

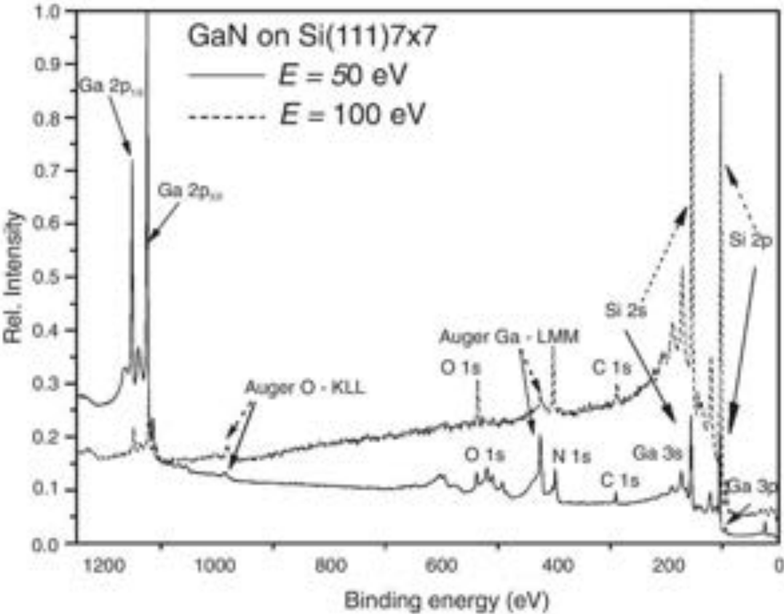

FIG. 3. XPS spectra of GaN ultrathin films deposited under assistance of 50 eV and 100 eV nitrogen ions at RT. Deposition parameters: crucible heating power $P = 11$ W and nitrogen ion current density $j = 300$ nA cm^{-2}.

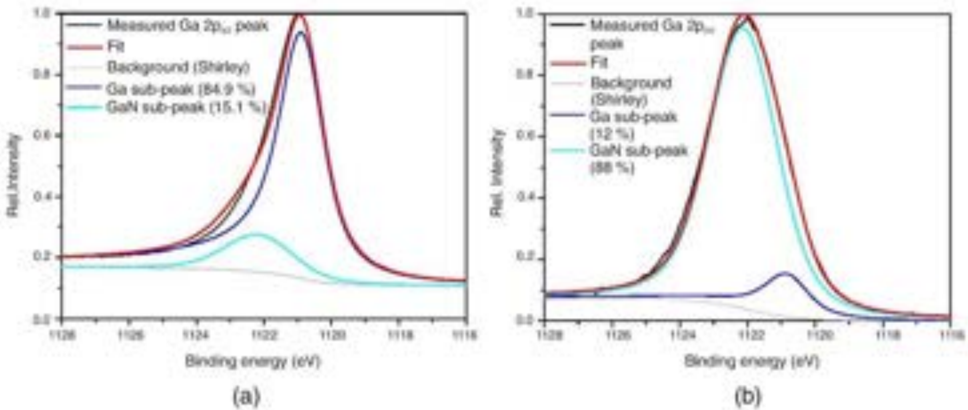

FIG. 4. The fitted XPS spectra for the GaN ultrathin films deposited (a) without ($j = 280$ nA cm^{-2}) and (b) with the focusing electrostatic optics ($j = 1000$ nA cm^{-2}). Deposition parameters: crucible heating power $P = 11$ W and nitrogen ion energy $E = 50$ eV.

the ion source without the focusing electrostatic optics, to that one of 88%.

The experimental peak intensities were obtained from the measured XPS spectra by a fitting procedure using the UNIFIT 2006 software package and application of the Voigt peak profile, and then corrected by a known spectrometer transmission function.[18]

The Ga $2p_{3/2}$ peak parameters and their assignment according to Ref. 19 are discussed in our previous paper and summarized in Table I. The fitting parameters of the Ga-Ga bond were deduced from a 2 ML thick gallium layer on the Si(111) 7 × 7 substrate prepared without the assisting nitrogen ion beam. The chemical shift according to the peak of metallic gallium (ΔE), Gaussian (GW), and Lorentzian (LW) widths, and asymmetry parameters of the peak components used in the fitting procedure of gallium oxide were published in our previous paper.[20] The fit parameters of the Ga-N bond were determined from the shift of the metallic Ga $2p_{3/2}$ peak taken from two distinct samples. The first sample was prepared by deposition of Ga under the assistance of the 50 eV nitrogen ion beam, the second sample was obtained by exposure of a Ga layer to the 50 eV nitrogen ion beam (post-nitridation). In both cases, the parameters of the Ga-N bond (energy shift (ΔE), Gaussian (GW) and Lorentzian (LW) width, and asymmetry) were identical. The summary of the fitting parameters of the Ga $2p_{3/2}$ peak is given in Table I.

The morphology of GaN films strongly depends on their chemical composition, namely on the ratio of Ga-N to Ga-Ga bonds. Such a dependence of surface morphology is shown in Figs. 5(a)–5(d). The shift of the Ga $2p_{3/2}$ peak with the

TABLE I. Fitting parameters of the Ga $2p_{3/2}$ peak.

Parameters (eV)	Ga-Ga	Ga-N	Ga-O
Energy	1120.7	1.33[a]	2
Gauss width	0.79	1.34	1.42
Lorentz width	1.7	1.14	1.7
Asymmetry	0.089	0	0

[a]Relative shift towards the Ga-Ga peak.

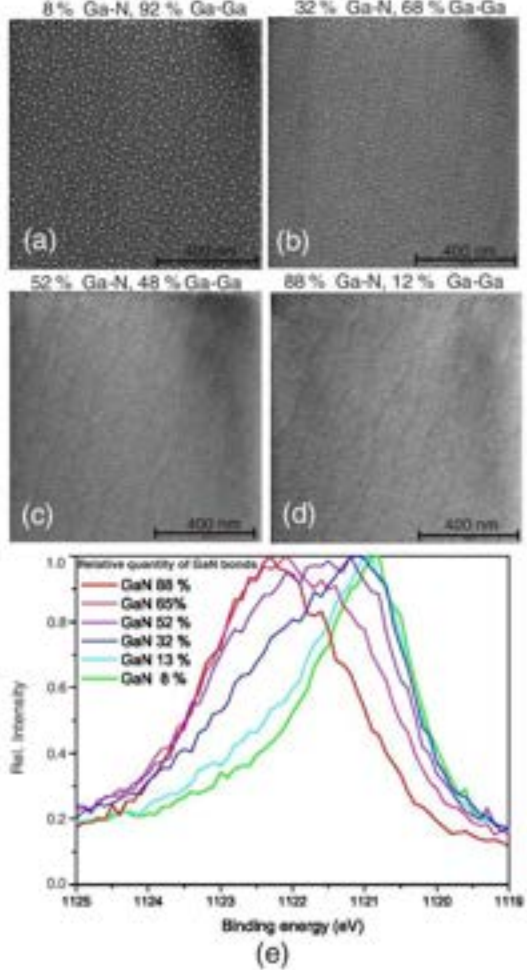

FIG. 5. Surface morphology of GaN layers observed by SEM in the outer parts of the nitrogen ion beam spot as a function of their chemical composition (a)–(d) and the Ga $2p_{3/2}$ peak-shift development with an increasing GaN content (e). Deposition parameters: crucible heating power $P = 11$ W, nitrogen ion energy $E = 50$ eV, and nitrogen ion current density $j = 800$ nA cm^{-2}.

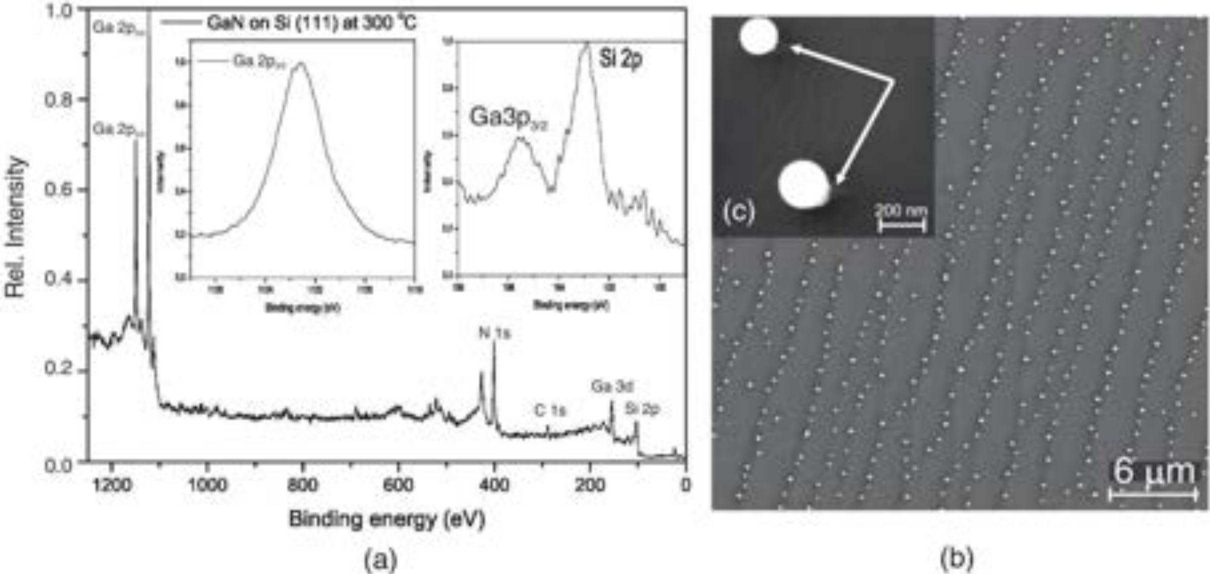

FIG. 6. (a) XPS spectrum of the GaN ultrathin film deposited at 300 °C under assistance of 50 eV nitrogen ions (in the insets the detailed spectra of Ga $2p_{3/2}$, Ga $3p_{3/2}$, and Si 2p peaks are shown). (b) SEM image of the film provided by BSE (scan area $30 \times 30\ \mu m^2$). (c) Detail of Ga droplets (scan area $1 \times 1\ \mu m^2$). Deposition parameters: crucible heating power $P = 12$ W and ion current density $j = 800$ nA cm^{-2}.

increasing GaN content is depicted in Fig. 5(e). The SEM images and XPS spectra were taken from the outer areas of the 50 eV nitrogen ion beam spot, where the ratio of Ga-N to Ga-Ga bonds is not constant and grows towards the centre due to a rapid increase of the nitrogen ion-beam current (see Fig. 2). We can see that the island-growth mode (Ga droplets), being typical for Ga layers on a Si substrate, changes to the layer-growth mode, typical for GaN. The surface of the pristine Si substrate consisted of closely spaced atomic steps and narrow terraces due to a 0.2° miscut of the surface towards the (111) plane. The terraces are visible in Figs. 5(c) and 5(d), when Ga droplets are replaced by smooth layers with the prevailing content of the GaN component, as shown by XPS (Fig. 5(e)).

Deposition of GaN at enhanced temperatures

GaN films were also prepared at a substrate temperature of 300 °C which is small compared with temperatures used in MBE or metalorganic chemical vapor deposition (MOCVD) growth. Similarly to the RT deposition experiments, XPS spectra confirmed the formation of Ga-N bonds in the layers (Fig. 6(a)) and their relative concentration increase with the nitrogen ion flux. Contrary to the RT deposition, the SEM images obtained by backscattered electrons (BSE) revealed the presence of droplets with a diameter of 300 nm segregated along the individual step edges between neighbouring terraces (Fig. 6(b)).

The signal provided by backscattered electrons is more sensitive to the elemental nature of sample atoms than that one related to secondary electrons.[21] Therefore, the intensity contrast in the BSE image between the droplets and the terraces remarkable in Fig. 6(b) indicates that the droplets consist of a different material compared to the terraces. As the GaN tends to create smooth layers over terraces (see the RT deposition and Fig. 5(d)) and the higher coverage of the substrate by these droplets (proportional to the number of the droplets) corresponds to an increase of the Ga-Ga bonds in the sample (Fig. 7), one can deduce that the droplets are formed by Ga atoms segregated at the atomic steps acting as nucleation centres. This is consistent with our previous experiments at higher substrate temperatures providing enhanced surface diffusion of excessive Ga atoms, and thus enabling them to reach these centres. Details of such Ga droplets are shown in

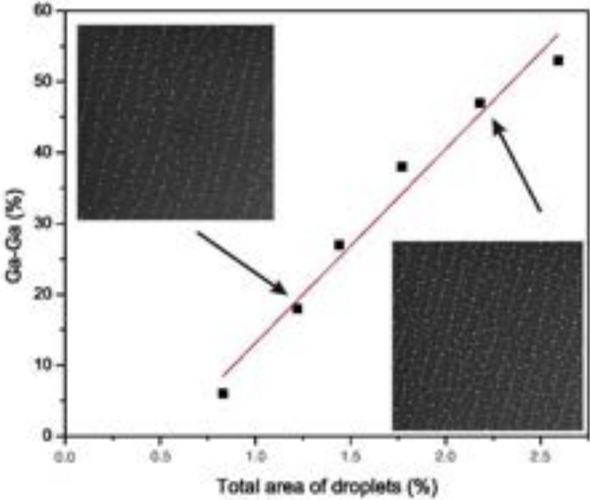

FIG. 7. Dependence of the relative number of the Ga-Ga bonds, obtained by decomposition of the Ga $2p_{3/2}$ peak, on the droplet coverage.

Fig. 6(c). Each droplet has a small tail at its borderline with the substrate (marked in the figure by the arrow). This tail will be the subject of our next research.

CONCLUSION

Optimization of an ion-atomic beam source towards producing ultra-low energy (20–200 eV) ion beams and thermal atomic beams simultaneously has been successfully performed. It is based on attaching a beam focusing system to the exit of the source combining an effusion cell and electron-impact ion beam source. The system consists of two electrostatic lenses such as a focusing electrode and a collimation tube. In addition to ions, the tube helps to collimate evaporated neutral atoms as well. The optimization resulted in a more than one order of magnitude increase of the maximum ion current density ($j \approx 1000$ nA/cm^2) compared to the source without the focusing electrostatic optics. This made it possible to grow GaN ultrathin films on Si(111)7 × 7 substrate surfaces at low deposition temperatures (RT, 300 °C) and reasonable deposition times.

It has been shown that the morphology of GaN layers strongly depends on the relative Ga-N bond concentration in the layers. The island-growth mode, being typical for Ga layers on a Si substrate, changes to the layer-growth mode, typical for GaN layers with a sufficient amount of Ga-N bonds.

Due to enhanced surface diffusion of excessive Ga atoms at a higher deposition temperature (300 °C), Ga droplets with a diameter of 300 nm segregate along the step edges between neighbouring terraces covered by GaN layers.

ACKNOWLEDGMENTS

This work was supported by the project "CEITEC - Central European Institute of Technology" (CZ.1.05/1.1.00/02.0068) from European Regional Development Fund, the Technology Agency of the Czech Republic (Project No. TE01020233), MOREMIT (Project No. FR-TI2/736), and the EU 7th Framework Programme (projects SYLICA, No. 286154, UnivSEM, No. 280566) and Grant Agancy of the Czech Republic (P108/12/P699).

[1] A. M. Morales and C. M. Lieber, Science **279**, 208–211 (1998).
[2] E. Jablonovich and G. D. Gody, IEEE Trans. Electron Dev. **29**, 300–304 (1982).
[3] H. Hirayama, A. Kinoshita, T. Yamabi, Y. Enomoto, A. Hirata, T. Araki, Y. Nanishi, and Y. Aoyagi, Appl. Phys. Lett. **80**, 207 (2002).
[4] P. Friedriechs, Phys. Status Solidi B **245**, 1232 (2008).
[5] T. Nakamura, M. Miura, N. Kawamoto, Y. Nakano, T. Otsuka, K. Okumura, and A. Kamisawa, Phys. Status Solidi A **206**, 2403 (2009).
[6] M. Razeghi and R. McClintock, J. Cryst. Growth **311**, 3067–3074 (2009).
[7] S. Fernández-Garrido, J. Grandal, E. Calleja, M. A. Sánchez-García, and D. López-Romero, J. Appl. Phys. **106**(12), 126102 (2009).
[8] Z. Yang, L. K. Li, and W. I. Wang, Appl. Phys. Lett. **67**(12), 1686 (1995).
[9] T. Kondo, K. Saitoh, Y. Yamamoto, T. Maruyama, and S. Naritsuka, Phys. Status Solidi A **203**(7), 1700–1703 (2006).
[10] T. Maruyama, H. Otsubo, T. Kondo, Y. Yamamoto, and S. Naritsuka, J. Cryst. Growth **301–302**, 486–489 (2007).
[11] S. Naritsuka, T. Kondo, H. Otsubo, K. Saitoh, Y. Yamamoto, and T. Maruyama, J. Cryst. Growth **300**(1), 118–122 (2007).
[12] R. K. Debnath, T. Stoica, A. Besmehn, K. Jeganathan, E. Sutter, R. Meijers, H. Lüth *et al.*, J. Cryst. Growth **311**(13), 3389–3394 (2009).
[13] S. Sienz, J. W. Gerlach, T. H. Höche, A. Sidorenko, T. G. Mayerhöfer, G. Benndorf, and B. Rauschenbach, J. Cryst. Growth **264**, 184 (2004).
[14] J. W. Gerlach, T. Ivanov, L. Neumann, T. Höche, D. Hirsch, and B. Rauschenbach, J. Appl. Phys. **111**(11), 113521 (2012).
[15] S. Voborný, M. Kolíbal, J. Mach, J. Čechal, P. Bábor, S. Průša, J. Spousta *et al.*, Thin Solid Films **459**(1–2), 17–22 (2004).
[16] J. Mach, T. Šamořil, S. Voborný, M. Kolíbal, J. Zlámal, J. Spousta, L. Dittrichová, and T. Šikola, Rev. Sci. Instrum. **82**, 083302 (2011).
[17] B. Lencová and J. Zlámal, Phys. Procedia **1**, 315 (2008).
[18] R. Hesse, P. Streubel, and R. Szargan, Surf. Interface Anal. **37**, 589-607 (2005).
[19] J. Hedman and N. Martensson, Phys. Scr. **22**, 176–178 (1980).
[20] J. Čechal, T. Matlocha, J. Polčák, M. Kolíbal, O. Tomanec, R. Kalousek, P. Dub, and T. Šikola, Thin Solid Films **517**(6), 1928–1934 (2009).
[21] S. Bertazzo, E. Gentleman, K. L. Cloyd, A. H. Chester, M. H. Yacoub, and M. M. Stevens, Nat. Mater. **12**(6), 576–583 (2013).

5.1.3 Článek č. 6 – Nízkoteplotní selektivní růst krystalů GaN na předem vzorovaný Si substrát

Autoři:

J. Mach, J. Piastek, J. Maniš, V. Čalkovský, T. Šamořil, J. Damková, M. Bartošík, S. Voborný, M. Konečný a T. Šikola

Review of Scientific Instruments [online]. 2014, **85**(8). Dostupné z: doi:10.1063/1.4892800.

Abstrakt:

V článku je popsána metoda výroby polí nanokrystalů GaN pomocí nízkoteplotního selektivního růstu na předem vzorkovaných křemíkových substrátech pokrytých nativním oxidem. Vzorkování substrátů bylo provedeno použitím fokusovaného iontového svazku galia (FIB). Za účelem umístění nanokrystalů GaN do specifických poloh, byly nejprve Ga ostrůvky napařeny při teplotě 280 °C na vzorkovaný substrát a poté byly post-nitridovány svazkem dusíkových iontů o ultra nízké energii (50 eV) při teplotě vzorku 200 °C. Pro získání rozměrnějších nanokrystalů GaN (průměr ≈ 150 nm a 200 nm) byl proces v několika cyklech opakován za mírně upravených depozičních podmínek. Kvalita nanokrystalů byla studována měřením jejich fotoluminiscenčních vlastností, které prokázaly výskyt píku emise zakázaného pásu kolem 367 nm (3,38 eV).

Applied Surface Science 497 (2019) 143705

Contents lists available at ScienceDirect

Applied Surface Science

journal homepage: www.elsevier.com/locate/apsusc

Full length article

Low temperature selective growth of GaN single crystals on pre-patterned Si substrates

Jindřich Mach[a,b,*], Jakub Piastek[a,b], Jaroslav Maniš[a], Vojtěch Čalkovský[a], Tomáš Šamořil[a,b], Jana Damková[b], Miroslav Bartošík[a,b], Stanislav Voborný[a,b], Martin Konečný[a,b], Tomáš Šikola[a,b]

[a] CEITEC BUT, Brno University of Technology, Technická 3058/10, 616 00 Brno, Czech Republic

[b] Institute of Physical Engineering, Brno University of Technology, Technická 2, 616 69 Brno, Czech Republic

ARTICLE INFO

Keywords:
GaN
Deposition
Selective growth
Low energy ions
Nanocrystals
Photoluminescence

ABSTRACT

We report on a hybrid method for fabrication of arrays of GaN nanocrystals by low-temperature UHV selective growth on pre-patterned silicon substrates covered by native oxide. Patterning of the substrates was performed by using a gallium focused ion beam (FIB). To get GaN nanocrystals at specific positions, Ga droplets were created at FIB patterned sites by evaporation of Ga atoms at 280 °C substrate temperature first, and then modified by their post-nitridation using an ultra-low energy (50 eV) nitrogen ion-beam at a sample temperature of 200 °C. To get larger arrays of GaN nanocrystals (≈150 nm and 200 nm in diameter), such a sequential process was repeated in several cycles at slightly modified operation conditions. The quality of the nanocrystals was checked by measurement of their photoluminescence properties which proved the occurrence of the peak of a band edge emission at around 367 nm (3.38 eV).

1. Introduction

Organization and positioning of nanoparticles (NPs) and nanowires on semiconductor substrates represent a big challenge to take an advantage of their properties for fabrication of innovative integrated devices [1–3]. While their self-organization on naturally occurring patterns [4] or through different chemical interactions [5] provides high quality of nanocrystals at an ultra-high density ($> 10^{10}\,cm^{-2}$) over large scale surfaces, the array parameters (pattern shape, periodicity) are generally controlled by the material/substrate system and thus the degrees of freedom in their choice are rather limited [6,7]. The main limitations of this method are a lack of control over positioning of individual nanoparticles and thus a poor uniformity of the formed NPs ensemble.

Contrary to that, in fabrication methods of NP arrays grown on artificially pre-patterned substrates one can control the absolute position of dots over a long-range scale. The nucleation sites (e.g. holes, grooves or other features) on substrates can be prepared by various nanofabrication techniques such as electron-beam lithography (EBL), focused ion beam (FIB), nanosphere lithography, anodic aluminum oxidation (AAO), AFM patterning, nanoimprint lithography, etc. [8–13].

In the last decade, many efforts have been put into growth of ordered arrays of III-V quantum nanostructures semiconductors, especially GaAs, InAs, and InP [14–17]. Naturally, growth of group III-nitride nanostructures has also attracted a lot of interest, but mostly ensembles of nanodots and nanocrystals distributed in disorderly have been achieved. One of the reasons for this is that the synthesis of GaN involves high activation energies generally overcome by high process temperatures (≥600 °C) which is associated with techniques such as metal-organic vapour-phase epitaxy (MOVPE) [18], plasma-assisted molecular beam epitaxy (PAMBE) [19] and chemical beam epitaxy (CBE) [20]. As a result, the spectrum of methods enabling selective growth of GaN nanostructures is limited as they must meet additional restraints related to this guided growth. For instance, in Ref. [21] the formation of ordered arrays of GaN microcrystals was studied. The microcrystals were grown by Ga droplet epitaxy at 500 °C on As-terminated Si (1 0 0) substrates patterned by low-energy Ga focused ion beam followed by nitridation at 600 °C using atomic nitrogen radicals generated by an RF radical cell.

However, in all these experiments high substrate temperatures during deposition were used (600–1000 °C) which can have a detrimental effect on some more complex structures and devices, being thus not compatible with some technology constraints laid on related fabrications steps.

To synthesize GaN films at lower temperatures (≈300 °C), a

* Corresponding author at: Institute of Physical Engineering, Brno University of Technology, Technická 2, 616 69 Brno, Czech Republic.
E-mail addresses: mach@fme.vutbr.cz (J. Mach), sikola@fme.vutbr.cz (T. Šikola).

https://doi.org/10.1016/j.apsusc.2019.143705
Received 20 May 2019; Received in revised form 8 August 2019; Accepted 14 August 2019
Available online 16 August 2019
0169-4332/ © 2019 Elsevier B.V. All rights reserved.

combination of Ga atomic beam evaporation (in principle an identical method to molecular beam epitaxy – MBE) and direct ion beam deposition have been successfully used in our group [22]. In this method, similarly to [23], nitrogen ion beams of hyperthermal energies (below 100 eV) provide activation energy needed for synthesis of GaN and so lower substrate temperatures can be used. An important advantage of the combination of the direct Ion beam deposition and "classical" MBE technique over MOCVD is the mutual independence of both processes and compatibility with UHV conditions enabling application of a wider spectrum of in-situ analytical methods. Deposition of nitrogen and gallium can be carried out simultaneously or one after another. This fact together with UHV conditions can be beneficial for a study of the early stages of thin film growth. Individual stages of the deposition process can be synchronized in different ways or separated in time (e. g. alternating atom and ion beam fluxes) and in situ analyzed. On the other hand, the exact mechanism of growth of nitrides by this combined technique is not fully known as the irradiation with hyperthermal ions brings the system into a condition far from thermodynamic equilibrium. The knowledge of this growth mechanism is particularly important for preparation of GaN single crystals and their selective growth.

In this paper, we demonstrate how to utilize such a method for low temperature ($T < 300\,^{\circ}C$) growth of arrays of GaN nanocrystals on Si substrates covered by native oxide. Ordered arrays of nanocrystals will enable us more easily to fabricate arrays of plasmonic antennas attached to these nanocrystals by electron beam lithography (leading to the so called plasmon enhanced photoluminescence). In addition, on purpose built a wide separation of GaN nanocrystals makes it possible to study the optical properties of individual nanocrystals.

The nanocrystals were formed by a sequential deposition, consisting of electron beam evaporation of gallium atoms on Si substrates prepatterned by FIB and resulting in the Stranski-Krastanov (SK) growth mode followed by post-nitridation by low-energy nitrogen ions (50 eV). Electron beam evaporation is well-matched to the hyperthermal ion beam technique because of the stability and controllability of the deposition process. The combination of these techniques generally provides a higher deposition rate, more uniform coverage, and a cleaner environment than ion beam sputtering.

Observation of photoluminescence (PL) peaks from GaN nanocrystals demonstrates cleanness and quality of the grown crystals. The influence of growth conditions and size of FIB-formed nucleation centers on the properties of GaN nanocrystals is discussed. In addition, we have proposed the method for cultivation of GaN nanocrystals and better control of their size.

2. Experimental section

The experiments were performed in a complex UHV apparatus [24] enabling in situ analysis of Ga and GaN structures by X-ray photoelectron spectroscopy (XPS) without their exposure to ambient atmosphere. XPS was performed by an experimental setup consisting of the X-ray source - DAR400 and hemispherical electrostatic analyzer - EA125 (both Omicron). Measurements were carried out at room temperature using Al Kα radiation. The pressure during the measurement was always better than 2×10^{-7} Pa. The morphology was studied ex-situ by scanning electron microscopy (SEM - LYRA 3 system, TESCAN) and atomic force microscopy (AFM - Integra, NT-MDT).

The samples with a size of $5 \times 15\,mm^2$ were cut from a Si(111) wafer doped by phosphorus (specific resistivity 0.029–0.030 Ω·cm). Subsequently, the samples were transferred into the complex UHV apparatus with a base pressure of 3×10^{-8} Pa and thermally annealed by direct resistive heating at 500 °C (> 120 min) under UHV conditions. This temperature was sufficient for removal of contaminants from the sample surface, but not high enough for decomposition of the native SiO_2 layer [25]. The structure and cleanness of the substrate were checked in situ by XPS.

The substrates were exposed to a gallium atom beam from an effusion cell - (Omicron) and to a ultra-low energy nitrogen ion beam (50 eV) produced from nitrogen gas (99.9999%) by a home-made ion-atomic beam source being a combination of an effusion cell and electron impact ion-beam source being 13 cm away from the sample. The detailed design of the source was described elsewhere [22,23]. The flux of nitrogen ions consists both of N^+ and N_2^+ ions (nitrogen current density $j = 1000\,nA/cm^2$). The work pressure in the deposition chamber measured by an ion gauge during nitridation was $p_{N2} = 5 \times 10^{-5}$ Pa. Thermal Ga atoms were evaporated from a PBN boat inside a Mo crucible. The effusion cell was calibrated for a precise control of the Ga growth rate (Ga flux density - 7.2×10^{12} atoms/s·cm²). The experimental setup is schematically shown in Fig. 1.

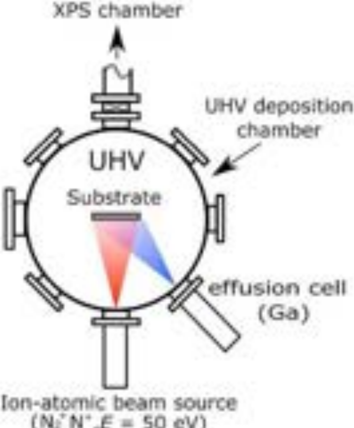

Fig. 1. Schematic of the deposition chamber.

3. Results and discussion

3.1. Formation of GaN nanocrystals

When Ga atoms and hyperthermal nitrogen ions are simultaneously impinging the surface, they mutually react at the surface and form Ga−N bonds. If the ratio of $Ga/N_2^+(N^+)$ flux is set in such a way that each Ga atom creates a bond with a nitrogen atom on the substrate, potential residual extra nitrogen particles are desorbed and the resulting GaN layer is smooth. This is demonstrated in Fig. 2a, b where SEM images of GaN layers on a Si(111)7 × 7 substrate and native SiO_2 surface deposited by a concurrent delivery of Ga atoms and nitrogen ions at substrate temperatures $T = 700\,^{\circ}C$ and $T = 400\,^{\circ}C$, respectively, are shown.

On the other hand, at lower (or zero) fluxes of hyperthermal nitrogen ions, surplus Ga adatoms diffuse along the surface and form Ga droplets at energetically favorable sites, e.g. at terrace edges of the Si (111)7 × 7 surface as reported in [23] and shown in Fig. 2c. This is a typical behavior for Ga atoms as reported in [26]. The size and mutual distance of Ga droplets depend proportionally on substrate temperature and also on surface roughness. In this figure SEM images of GaN smooth layers on terraces of the Si(111)7 × 7 substrate with an excess of Ga atoms condensed preliminary in form of droplets at edges of terraces are shown (Ga flux density - 2.6×10^{16} atoms/h·cm², nitrogen current density $j = 1000\,nA/cm^2$, substrate temperature $T = 300\,^{\circ}C$). It is worth mentioning that some droplets already contain nuclei of GaN at the interface with the substrate as can be seen in detail in Fig. 2d. It is in agreement with [27] where it is hypothesized that the top surface of liquid Ga droplets acts as a major mass transport path for nitrogen species delivered by hyperthermal nitrogen ions which then diffuse to peripheral regions of the droplet-substrate interface. Hence, this interface acts as a collector of nitrogen particles dissolved on the droplet

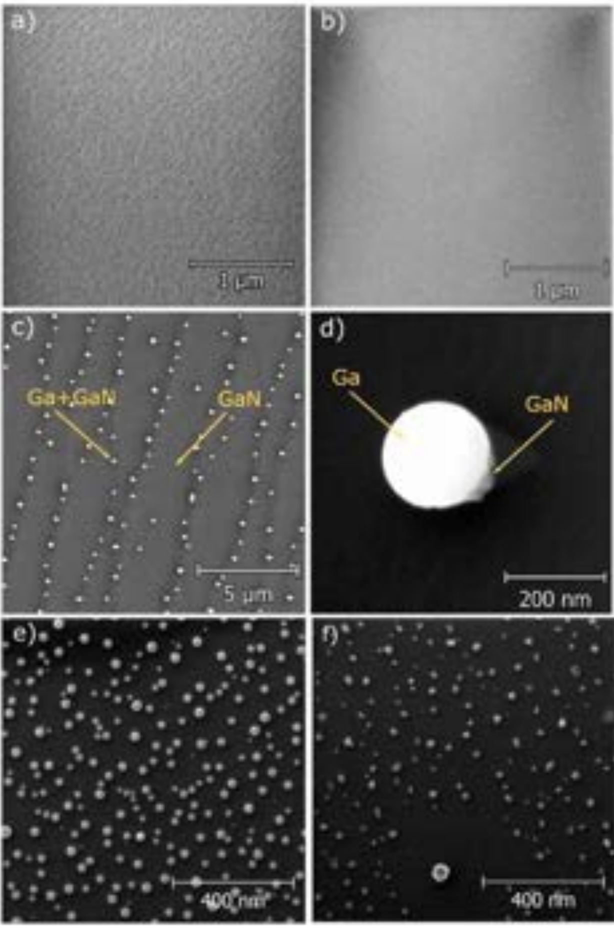

Fig. 2. SEM images of GaN layers deposited by a concurrent delivery of Ga atoms and nitrogen ions (Ga flux density - 7.2×10^{12} atoms/s·cm^2, nitrogen current density $j = 1000$ nA/cm^2) on a) the Si(111)7 × 7 substrate at $T = 700$ °C and b) the native SiO_2 surface at $T = 400$ °C. c) GaN smooth layers on terraces of the Si(111)7 × 7 substrate with an excess of Ga atoms condensed preliminary in form of droplets at edges of terraces [23] (taken by SEM) (Ga flux density - 7.2×10^{12} atoms/s·cm^2, nitrogen current density $j = 1000$ nA/cm^2, $T = 300$ °C). Some droplets already contain nuclei of GaN at the interface with the substrate as can be seen in detail at d). SEM images of e) Ga droplets deposited on the native SiO_2 surface at substrate temperature $T = 200$ °C (7.2×10^{12} atoms/s·cm^2, 60 min), and f) GaN nanocrystals formed after an exposure of Ga droplets by low energy nitrogen ions at substrate temperature $T = 200$ °C (nitrogen current density $j = 1000$ nA/cm^2, 60 min).

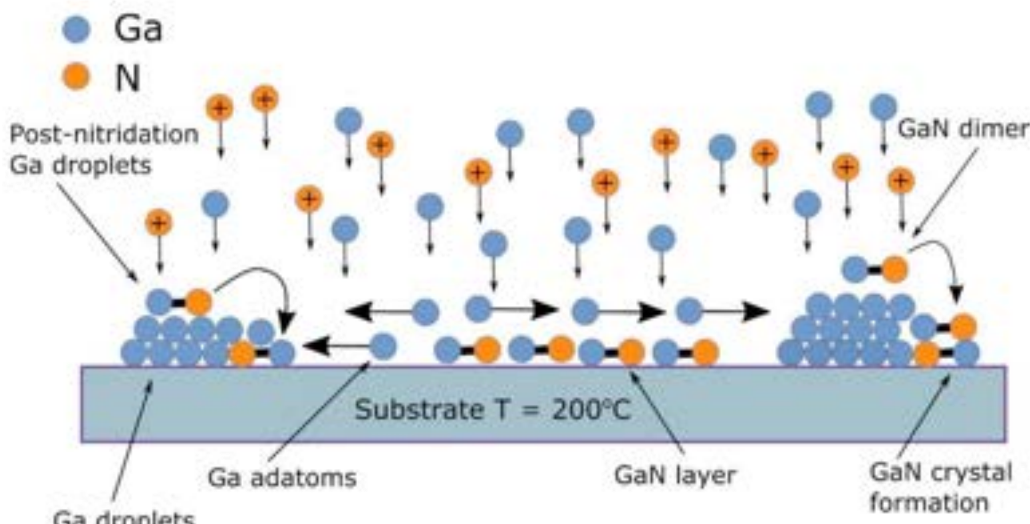

Fig. 3. Schematic of GaN growth based on the relevant surface processes such as adsorption, diffusion, and nucleation. The transformation of Ga droplets to GaN crystals was observed at higher substrate temperatures ($T > 200$ °C). This process is related to diffusion of GaN dimers on Ga droplet surface or inside of Ga droplets.

(and of those diffusing towards the interface from the substrate surface around droplets) as schematically depicted in Fig. 3. These species initiate formation of Ga−N crystallization nuclei at the liquid-solid interface, which is followed by propagation of a crystallization process from the peripheral droplet region towards the center of the interface.

In Fig. 2e a SEM image of Ga droplets deposited without nitrogen ion flux for 60 min on the native SiO_2 surface by a Ga atomic flux density of 7.2×10^{12} atoms/s·cm^2 at substrate temperature $T = 200$ °C is shown. The image of Ga droplets exposed for 60 min to the current of low energy nitrogen ions ($j = 1000$ nA/cm^2) at substrate temperature $T = 200$ °C can be seen in Fig. 2f. In the figure the formation of crystals is apparent. Their chemical composition was checked by XPS which proved the crystals consisted of GaN. It is worth noting that the transformation of Ga islands into GaN nanocrystals was carried out without breaking UHV conditions.

The size and quantity of Ga droplets enabling transformation to GaN crystals depend on the sticking coefficient of Ga atoms on the substrate [26] which is a function of substrate temperature.

At higher temperatures, Ga droplets do not nucleate because most of gallium atoms do not stick to the surface (e.g. $T > 450$ °C on Si(111) 7×7 or $T > 300$ °C on SiO_2) and the substrate is covered only by a GaN layer formed by instantaneous local interaction of Ga atoms with nitrogen species just upon their impingement on the surface. Thus, the final morphology of the ultrathin film prepared by the MBE and direct ion beam deposition is given by a combination of two events: on the one hand, by a direct impact of a nitrogen ion into close vicinity of a Ga adatom (smooth layer), and on the other hand, by its impact on a Ga island (nanocrystal). Consequently, smoother films can be grown by a suitable setting of the Ga atom/nitrogen ion impact ratio. On the other hand, single GaN nanocrystals can be formed by a separate deposition of Ga atoms first, followed by a subsequent nitrogen ion beam irradiation (energy of ions below 50 eV).

3.2. Selective growth of GaN nanocrystals

The surface diffusion plays an important role during selective growth of various materials, as atoms of deposited materials have to be transported to nucleation sites [9]. However, at temperatures in the range from RT to 800 °C the surface diffusion length of Ga−N dimers on SiO_2 and Si surfaces is significantly shorter than for Ga atoms on these surfaces. This shorter diffusion length does not allow carrying out the selective growth by the simultaneous deposition of Ga atoms and nitrogen ions. Under the conditions of this concurrent deposition the SK growth mode has not been observed for SiO_2 surfaces and Si(111)7×7 substrates in the temperature range RT–600 °C and RT–800 °C, respectively. Hence, when the Ga atom/nitrogen ion flux ratio is set at these temperatures to the values not leading to the nucleation of Ga islands, the growth results in a smooth GaN layer as shown in Fig. 2a and b.

To achieve the selective growth of ordered GaN nanostructures, a two-step deposition procedure described already above was applied. In the first step, Ga atoms were deposited on a surface with nucleation sites created by FIB. Due to a long surface diffusion length Ga atoms were transported towards these nucleation sites and formed droplets there. During the second step, Ga droplets were transformed into GaN nanocrystals by low energy nitrogen ions (50 eV) impinging upon them. Such a mechanism of the sequential deposition method enabling fabrication of ordered self-assembled arrays of GaN nanocrystals by this post-nitridation process is schematically shown in Fig. 4a–d.

The experiments were carried out on 10×10 arrays of circular nucleation sites of a diameter ranging from 100 nm to 300 nm and produced by respective ion doses 1.1×10^7 ions/μm^2–31×10^7 ions/μm^2. The spacing of the nucleation centers varied from 100 nm to 1500 nm on the Si(111) substrate covered with a 2 nm-thick native SiO_2 layer. A typical FIB-patterned substrate surface before the nucleation of Ga atoms is shown in Fig. 4e. The profiles of nucleation centers fabricated by FIB at different Ga ion doses measured by AFM are shown in Fig. 4f.

First, at lower ion beam doses the sub-surface layers are amorphized and implanted by Ga ions, which leads to creation of conical features swollen above the surface. It is only for ion beam doses above 5.39×10^{-7} ions·mm^{-2} when the central hole – crater in these features is observed.

Ga atoms were deposited on the FIB patterned substrate at the substrate temperature $T = 280$ °C and a flux density of 7.2×10^{12} atoms/s·cm^2 for 60 min. As the sticking coefficient of Ga atoms on the flat SiO_2 surface is close to zero [9], Ga atoms nucleated preferentially at the surface defects fabricated by FIB. Subsequently, Ga islands were exposed to a low energy (50 eV) nitrogen ion beam with the current density 1000 nA/cm^2 for 60 min at the substrate temperature 200 °C. After this procedure GaN crystals occupied positions exposed to FIB only.

The typical size of deposited crystals measured by contact-AFM was in the range 20–40 nm. The number of GaN crystals occupying the milled nucleation sites depends on the area of these nucleation centers – further called the spot areas (defined as the inner area of the milled crater). Fig. 5a shows GaN crystals grown selectively at circularly shaped nucleation centers of an area of 1.8×10^4 nm^2 and grid spacing of 400 nm prepared by ion-beam scanning over a disk-like area of a diameter of 220 nm. The number of GaN crystals located inside the FIB-made nucleation site depends linearly on its area as shown for different spacing of nucleation sites (300–600 nm), in Fig. 5c. From the results depicted in this figure one cannot claim that decreasing the spot size leads to 1 nanocrystal occupancy. To achieve just one nanocrystal at a FIB-made nucleation center one should apply the so-called "spot" ion-beam irradiation where the ion beam is fixed to one spot without scanning over the time An example of typical selectively deposited GaN crystal structures mostly possessing one GaN crystal in each nucleation site and prepared by this method at an ion beam dose of 5.3×10^7 ions/μm^2 for an array spacing of 300 nm is shown in Fig. 5b.

The occupation of nucleation sites by GaN nanocrystals depends on the FIB Ga ion dose and on the spacing of nucleation sites as well, as shown in Fig. 5d. The higher dose of Ga ions has a more profound influence on the nucleation site profile (see Fig. 4f) and thus the crater area, which leads to the higher capture probability of Ga atoms at this site. At the same time, the occupation probability of the nucleation sites made by FIB rises with the increasing spacing of nucleation sites. This is caused by an increase of the collection area of Ga atoms related to one nucleation site (a decrease of the Ga depletion effect). Obviously, an increase of the nucleation site occupation at a lower spacing of nucleation sites can be provided by a higher Ga atom coverage on the surface.

3.3. Cultivation of nanocrystals

The main challenge of the post-nitridation method is the preparation of GaN nanocrystals with a size bigger than 40 nm. The size of these nanocrystals is primarily controlled by the dimension of Ga droplets. Generally, the size of Ga nanodroplets should grow with the substrate temperature. However, to ensure sufficient mobility of Ga atoms to reach comfortably pre-patterned confining spots, the substrate temperature must be kept close to the values where the sticking coefficient of Ga on the SiO_2 substrate is nearly zero (~280 °C). Hence, there is a sufficient depletion of the Ga material feeding the spots and Ga droplets remain small.

To overcome this problem, we have proposed a method schematically depicted in Fig. 6a. It is based on the already discussed sequential deposition being repeatedly applied in several cycles. In the first step, small GaN crystals are formed by post-nitridation of Ga droplets and then further sequences of Ga deposition and Ga post-nitridation are performed for several times. In this way, the crystals can be significantly increased as demonstrated in Fig. 6b for the case of five deposition cycles.

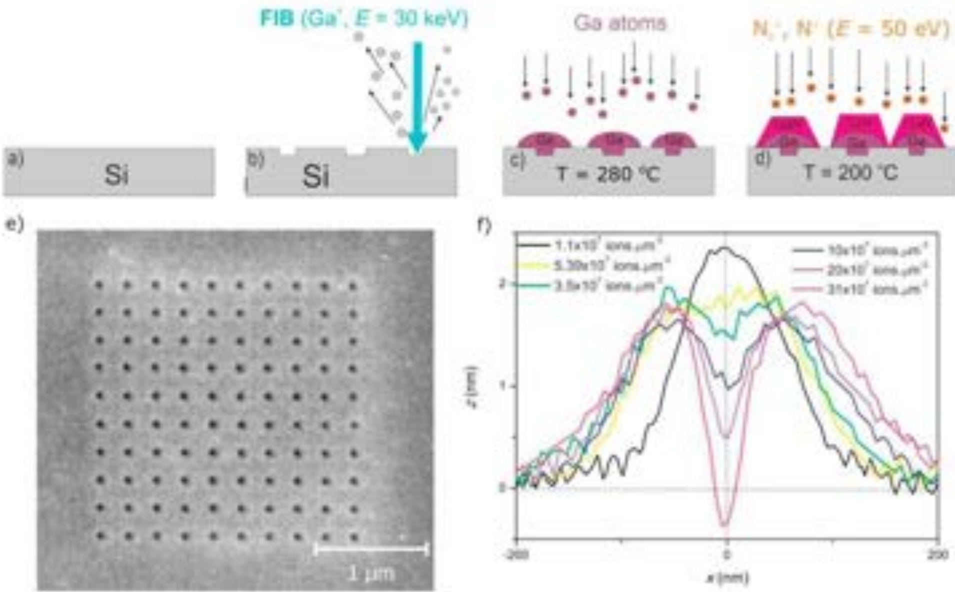

Fig. 4. Description of the selective growth process of an array of GaN nanocrystals (spacing 250 nm): a) Si substrate covered with a native oxide, b) patterning of the substrate by FIB, c) deposition of Ga islands-droplets, d) GaN nanocrystal formation by low-energy ion beam nitridation, e) SEM image of an array of nucleation centers on the Si(111) substrate fabricated by FIB at an ion dose of 6.4×10^7 ions/µm^2 for each spot, and f) AFM profiles of the nucleation centers prepared by FIB for different ion doses.

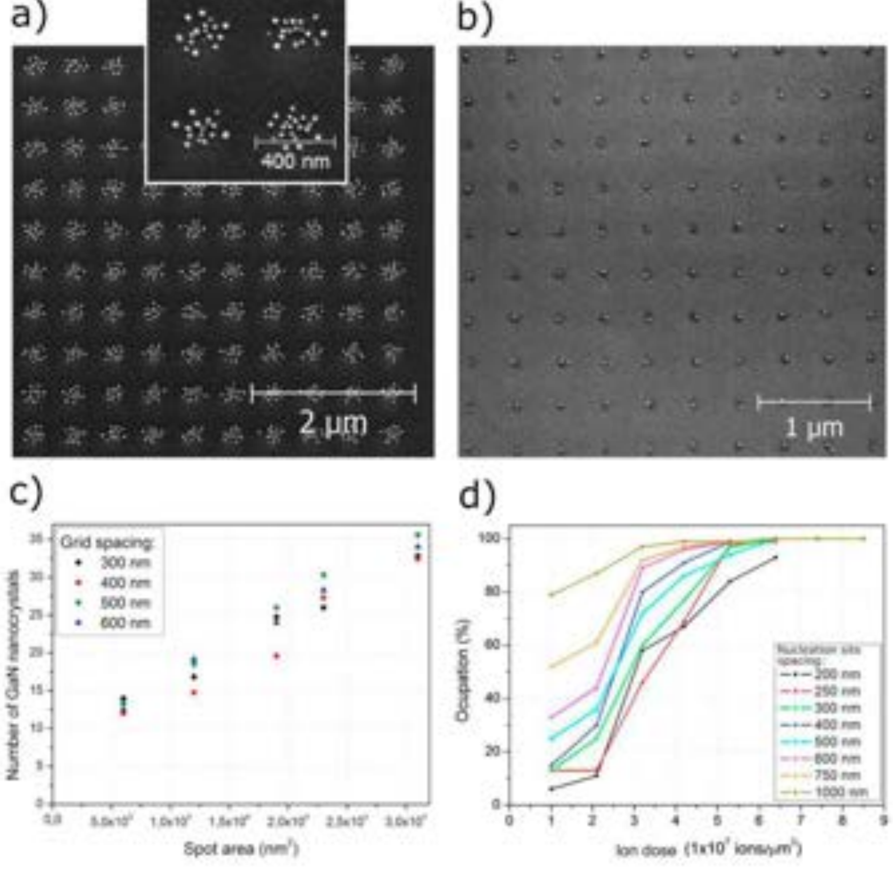

Fig. 5. SEM images of GaN nanocrystals deposited selectively by post-nitridation of Ga droplets on a Si(111) substrate locally exposed to FIB (Ga flux density 7.2×10^{12} atoms/s·cm^2, $t = 60$ min, $T = 280$ °C, nitrogen-ion-beam current density 1000 nA/cm^2, $t = 60$ min, $T = 200$ °C). GaN nanocrystals grown on arrays of nucleation centers with a) the spot diameter 220 nm (area – 1.8×10^4 nm^2) and spacing 400 nm prepared at an ion beam dose of 2.2×10^8 ions/µm^2, and b) the spot diameter 50 nm and spacing 300 nm prepared by "spot" ion beam irradiation at the Ga ion dose 5.3×10^7 ions/µm^2. c) Average number of GaN nanocrystals grown at one nucleation center as a function of the spot area, and d) percentage of GaN crystal occupation at nucleation sites for different FIB Ga ion doses. Parameter in c) and d): different nucleation site spacing.

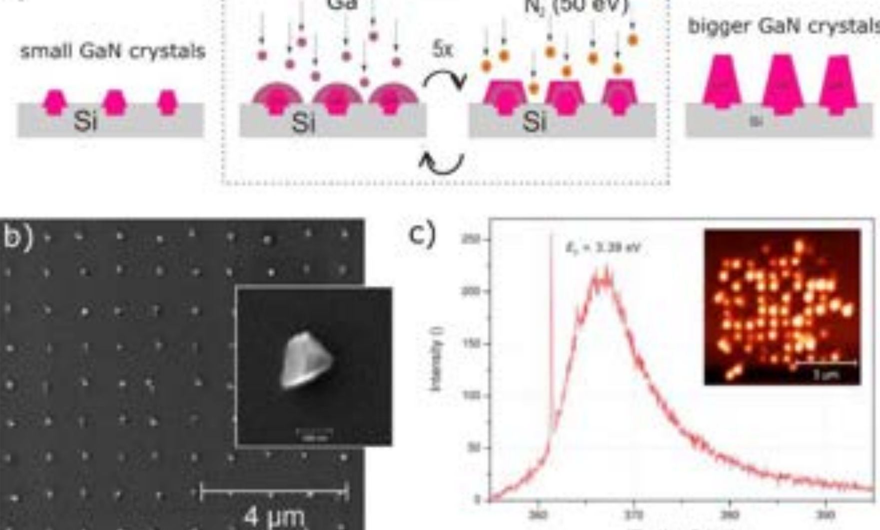

Fig. 6. a) Schematic of the sequential deposition method applied for cultivation of GaN nanocrystals. b) SEM image of GaN islands after five cycles of the sequential deposition, c) µPL spectrum of ordered GaN crystals after five cycles of the sequential deposition (inset – PL radiation from an array of GaN nanocrystals detected by a CCD camera).

In the first step of this experiment, small GaN crystals were formed by the sequential deposition at conditions described in Section 3.2. After that, the first sequential deposition cycle carried out under slightly distinct conditions started - In this cycle gallium was deposited on the sample for 60 min at 300 °C and a Ga flux density of 7.2×10^{12} atoms/s·cm^2. A bit increased substrate temperature in this step towards the previous one (i.e. 300 °C to 280 °C) provided enhanced surface diffusion of Ga atoms and their nucleation at small GaN nanocrystals. Then the surface was cooled down to 200 °C and exposed for 60 min to the 50 eV nitrogen ion beam with a current density of 1000 nA/cm^2 to accomplish post-nitridation. Such a deposition cycle was repeated for five times.

In the inset of Fig. 6b GaN crystal facets are clearly visible. To check the quality of GaN crystals, photoluminescence properties of GaN crystals grown up to an approximate size of 150 nm and 200 nm (measured by AFM) were tested.

The PL measurement was carried out at room temperature using a micro-Raman spectroscopy system (WITEC, alfa 300R) with the excitation laser wavelength λ_{ex} = 355 nm (solid state laser). The PL emission was detected by a CCD camera (DU420A-BU-352) and spectra taken by a spectrophotometer (UHT 400). The diameter of the focused laser spot was about 0.5 µm.

A typical PL spectrum obtained for a laser excitation power of 2 mW is demonstrated in Fig. 6c. The spectrum was collected from an array of GaN nanocrystals shown in the inset of the figure and clearly revealed the peak of a band edge emission at around 367 nm (3.38 eV, blue luminescence). Interestingly, not all nanocrystals were PL active despite their similar morphology and size. With this respect, additional studies going beyond the scope of this paper should be carried out.

4. Conclusion

The successful approach on UHV growth of arrays of GaN nanocrystals has been presented. This selective growth was achieved by replacing a concurrent deposition of Ga atoms and nitrogen ions, provided by the simultaneous MBE and direct ion beam deposition and preferentially leading to continuous thin films of GaN, by time splitting of delivery of these individual constituents on a FIB pre-patterned SiO_2 substrate. It means, first Ga atoms were deposited on these pre-patterned substrate at a trade-off temperature (280 °C) high enough to reach the FIB-made nucleation spots and sufficiently low to prevent desorption of Ga atoms from the surface. After that a post- nitridation of small Ga droplets nucleated at the spots was carried out by a 50 eV-nitrogen ion beam deposition to get GaN nanocrystals at T = 200 °C. Synthesis of GaN at such a low temperature was achieved by an excess energy locally delivered by hyperthermal nitrogen ions. To get larger arrays of GaN nanocrystals (≈150 nm and 200 nm in diameter), such a sequential deposition was repeated in several cycles at slightly modified operation conditions. The quality of the nanocrystals was checked by measurement of their photoluminescence properties which proved the occurrence of the peak of a band edge emission at around 367 nm (3.38 eV).

Acknowledgment

This work was supported by the Technology Agency of the Czech Republic (grant No. TE01020233), H2020 Twinning programme (project SINNCE, 810626), Grant Agency of the Czech Republic (grant 17-33767L), and MEYS CR (grant No. LQ1601 – CEITEC 2020). We also acknowledge the support by the Grant Agency of the Czech Republic (grant No. 17-21413S).

References

[1] C. Lee, A.L. Barabási, Spatial ordering of islands grown on patterned surfaces, Appl. Phys. Lett. 73 (18) (1998) 2651–2653.
[2] T.W.H. Oates, A. Keller, S. Noda, S. Facsko, Self-organized metallic nanoparticle and nanowire arrays from ion-sputtered silicon templates, Appl. Phys. Lett. 93 (6) (2008) 063106-3.
[3] K.V. Sarathlal, D. Kumar, A. Gupta, Growth study of Co thin film on nanorippled Si (100) substrate, Appl. Phys. Lett. 98 (12) (2011) 123111–123113.
[4] V. Repain, J.M. Berroir, S. Rousset, J. Lecoeur, Growth of self-organized cobalt nanostructures on Au(111) vicinal surfaces, Surf. Sci. 447 (1) (2000) L152–L156.
[5] B. Yang, F. Liu, M.G. Lagally, Local strain-mediated chemical potential control of quantum dot self-organization in heteroepitaxy, Phys. Rev. Lett. 92 (2) (2004) 025502–025504.
[6] H. Sekiguchi, K. Kishino, A. Kikuchi, Ti-mask selective-area growth of GaN by RF-plasma-assisted molecular-beam epitaxy for fabricating regularly arranged InGaN/GaN nanocolumns, Appl. Phys. Express 1 (12) (2008) 124002–124003.
[7] H. Sekiguchi, K. Kishino, A. Kikuchi, Emission color control from blue to red with nanocolumn diameter of InGaN/GaN nanocolumn arrays grown on same substrate, Appl. Phys. Lett. 96 (23) (2010) 96–99.
[8] L. Liu, M. Shan, L. Cheng, S. Zhao, R. Qun, S.T. Lee, Edge-enhanced Raman scattering effect from Au deposited nanoedge array, Appl. Phys. Lett. 98 (7) (2011) 073114-3.

[9] M. Bartošík, M. Kolíbal, J. Čechal, J. Mach, T. Šikola, Selective growth of metallic nanostructures on surfaces patterned by AFM local anodic oxidation, J. Nanosci. Nanotechnol. 9 (10) (2009) 5887–5890.
[10] T. Yasuda, S. Yamasaki, Nanoscale selective-area epitaxial growth of Si using an ultrathin SiO_2/Si_3N_4 mask patterned by an atomic force microscope, Appl. Phys. Lett. 77 (24) (2000) 3917–3919.
[11] T. Mårtensson, P. Carlberg, M. Borgström, L. Montelius, W. Seifert, L. Samuelson, Nanowire arrays defined by nanoimprint lithography, Nano Lett. 4 (4) (2004) 699–702.
[12] X. Qian, J. Li, D. Wasserman, W.D. Goodhue, Uniform InGaAs quantum dot arrays fabricated using nanosphere lithography, Appl. Phys. Lett. 93 (23) (2008) 1–4.
[13] K. Meneou, K.Y. Cheng, Z.H. Zhang, C.L. Tsai, C.F. Xu, K.C. Hsieh, Site-controlled InAs quantum dots regrown on nonlithographically patterned GaAs, Appl. Phys. Lett. 86 (15) (2005) 1–3.
[14] J. Tommila, et al., Nanoimprint lithography patterned GaAs templates for site-controlled InAs quantum dots, J. Cryst. Growth 323 (1) (2011) 183–186.
[15] C.C. Cheng, K. Meneou, K.Y. Cheng, Effects of nano-pattern size on the property of InAs site-controlled quantum dots, J. Cryst. Growth 323 (1) (2011) 180–182.
[16] E. Seljuk, A.Y. Silov, R. Nötzel, Single InAs quantum dot arrays and directed self-organization on patterned GaAs (311)B substrates, Appl. Phys. Lett. 94 (26) (2009) 263108-3.
[17] H. Heidemeyer, C. Müller, O.G. Schmidt, Structural and optical investigations of 1-, 2-, and 3-dimensional InAs quantum dot arrays, Physica E 23 (3–4) (2004) 237–242.
[18] S.D. Hersee, J.C. Ramer, K.J. Malloy, G. Sapphire, The Microstructure of Metalorganic-Deposition GaN on Sapphire, no. July (1997), pp. 45–51.
[19] C. Skierbiszewski, et al., Nitride-based laser diodes grown by plasma-assisted molecular beam epitaxy, J. Phys. D. Appl. Phys. 47 (7) (2014) 073001–073018.
[20] M. Kappers, J.L. Guyaux, J. Olivier, R. Bisaro, C. Grattepain, J.C. Garcia, Chemical beam epitaxy of GaN on (0001) sapphire substrate, Mater. Sci. Eng. B 59 (1–3) (1999) 52–55.
[21] T. Nagata, P. Ahmet, T. Sekiguchi, T. Chikyow, Low-temperature growth of GaN microcrystals from position-controlled Ga droplets arrayed by a low-energy focused ion beam system, J. Cryst. Growth 283 (3–4) (2005) 328–331 Oct.
[22] J. Mach, et al., An ultra-low energy (30–200 eV) ion-atomic beam source for ion-beam-assisted deposition in ultrahigh vacuum, Rev. Sci. Instrum. 82 (8) (2011) 083302-083308.
[23] J. Mach, et al., Optimization of ion-atomic beam source for deposition of GaN ultrathin films, Rev. Sci. Instrum. 85 (8) (2014) 083302-083306.
[24] S. Voborný, et al., Deposition and in-situ characterization of ultra-thin films, Thin Solid Films 459 (1–2) (2004) 17–22 Jul.
[25] K. Xue, J.B. Xu, H.P. Ho, Nanoscale in situ investigation of ultrathin silicon oxide thermal decomposition by high temperature scanning tunnelling microscopy, Nanotechnology 18 (48) (2007) 485709-7.
[26] M. Kolíbal, T. Čechal, E. Brandejsová, J. Čechal, T. Šikola, Self-limiting cyclic growth of gallium droplets on Si(111), Nanotechnology 19 (47) (2008) 475606-5.
[27] J.W. Gerlach, T. Ivanov, L. Neumann, T. Höche, D. Hirsch, B. Rauschenbach, Epitaxial GaN films by hyperthermal ion-beam nitridation of Ga droplets, J. Appl. Phys. 111 (11) (2012) 113521-10.

6. Iontové zdroje

Jestliže je z atomu odstraněn jeden elektron, stává se s něj jednou ionizovaný kladný iont. Toto je jeden z nejběžnějších jevů vyskytujících se při výbojích v plynech. V případech odstranění více elektronů z atomů hovoříme o vícekrát ionizovaných iontech v závislosti na počtu odebraných elektronů. K ionizaci je potřebná určitá minimální hodnota energie E_{ion}. Hodnota ionizační energie[3] je silně závislá na elektronové konfiguraci ionizovaného prvku. Negativní ionty mohou být vytvářeny interakcí kladných iontů s atomy s nízkým ionizačním potenciálem. Ionty jsou tvořeny z neutrálních atomů různými ionizačními způsoby, jako například elektronově srážková ionizace, fotoionizace, ionizace polem nebo povrchovou ionizací. V případě elektronově srážkové ionizace, kdy dochází k interakci atomů plynu s elektrony, lze výsledný proud iontů I_{ion}vyjádřit následovně

$$I_{\text{ion}} = J_e \, V_{\text{ef}} \, n \; \sigma_{\text{i}} \, , \tag{18}$$

kde J_{e} je proudová hustota elektronů, V_{ef} je efektivní objem ionizačního prostoru, n je koncentrace atomů plynů určených k ionizaci a σ_{i} je ionizační účinný průřez [30]. Tento ionizační účinný průřez je závislý na energii interagujících elektronů. Na obrázku 22 jsou zobrazeny průběhy ionizačních účinných průřezů pro vybrané prvky v závislosti na energii interagujících elektronů.

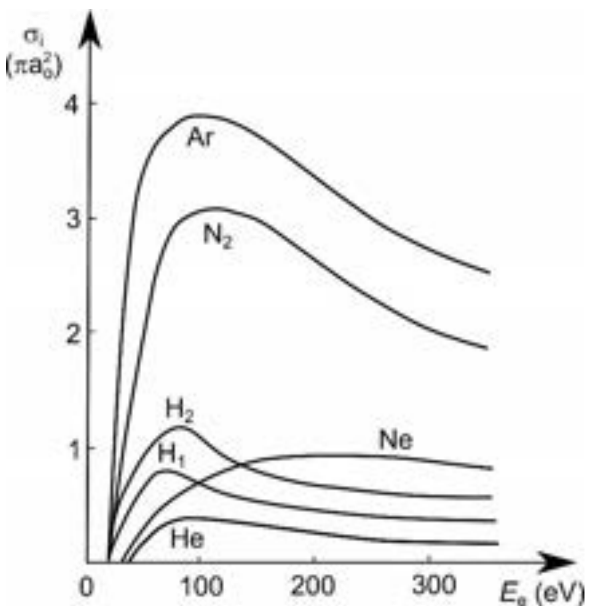

Obrázek 22: Závislost ionizačního účinného průřezu na energii elektronů pro vybrané plyny [30].[4]

Iontové zdroje využívající elektronově srážkového principu jsou velmi rozšířené a existuje mnoho jejich konstrukčních variant. Společným jmenovatelem těchto konstrukcí je katoda emitující elektrony (často termoemisní), které jsou urychlovány k anodě. Tyto elektrony se sráží s atomy plynu a vytváří jejich ionty. Při vyšších tlacích dochází k výboji, který je vyvolán vzniklou lavinou ionizujících sekundárních elektronů, což vede k vytvoření plazmy o specifickém potenciálu. Ionty lze extrahovat kolmo skrz anodu nebo katodu. Ke zvýšení ionizační účinnosti se často užívá magnetického pole,

---

[3] Také nazývaný ionizační potenciál.

[4] a_o značí Bohrův poloměr $0{,}529 \times 10^{-10}$ m.

způsobující pohyb elektronů po spirále, čímž se prodlouží jejich trajektorie směrem k anodě a tím se zvýší pravděpodobnost srážky (vzniku iontů). Nicméně aplikace magnetického pole nemusí být vhodná pro umístění iontového zdroje do elektronových mikroskopů. Jinou možností, jak prodloužit trajektorie elektronů, je užití speciálně tvarovaných elektrod vytvářejících sedlové elektrické pole. Jako příklad lze uvést námi vyvinutý iontový zdroj se sedlovým polem určený pro odprašování vzorků. Jedná se o elektronově srážkový zdroj se žhavenou wolframovou katodou. Mezi anodou a katodou jsou umístěny dvě speciálně tvarované elektrody, které vytváří v prostoru zdroje sedlové elektrické pole. Toto pole zapříčiňuje pohyb elektronů opisující trajektorii ležaté osmičky a tím se zvyšuje pravděpodobnost ionizace. Je možné říci, že elektron opisuje zmíněnou trajektorii tak dlouho, dokud nedojde k jeho srážce s atomem plynu a vytvoření kladného iontu. Simulace trajektorie elektronů (černá čára) provedená v programu EOD je zobrazena na obrázku 23. Z trajektorií elektronů byla určena místa vzniku argonových iontů a následně spočtena jejich trajektorie (růžová barva).

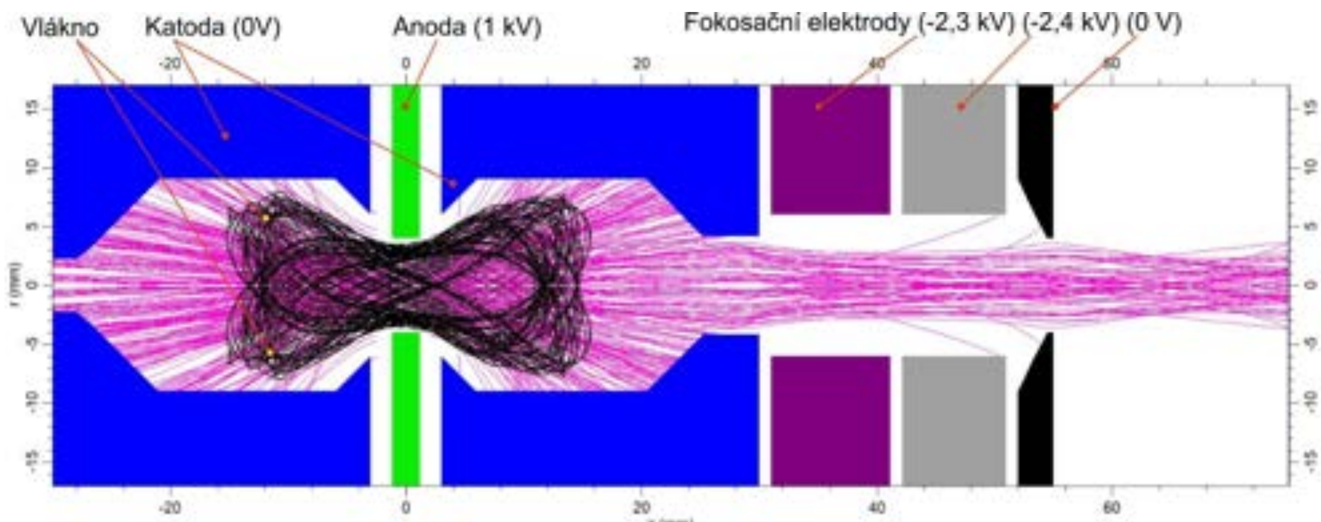

Obrázek 23: Trajektorie elektronů (černá) a iontů Ar^+ (růžová) uvnitř elektronově srážkového iontového zdroje. Simulace provedena v programu EOD [56].

3D model realizovaného sedlového iontového zdroje je zobrazen na obrázku 24. Zdroj je určen primárně pro odprašování povrchu substrátů. V současné době se provádí optimalizace a charakterizace jeho vlastností. Při tlaku $p_{Ar} = 3 \cdot 10^{-3}$ Pa a napětí na anodě 1 000 V je dosahována proudová hustota argonových iontů Ar^+ až $j_{ion} = 70\ \mu A/cm^2$. Parametry, profil a energie iontového svazku argonu byly měřeny pomocí Faradayovy sondy o průměru detekčního otvoru 2 mm a jsou uvedeny na obrázku 25. Profil kráteru vzniklého na Si substrátu po 30 minutách odprašování byl měřen pomocí profilometru Bruker Dektak XT a je zobrazen na obrázku 26.

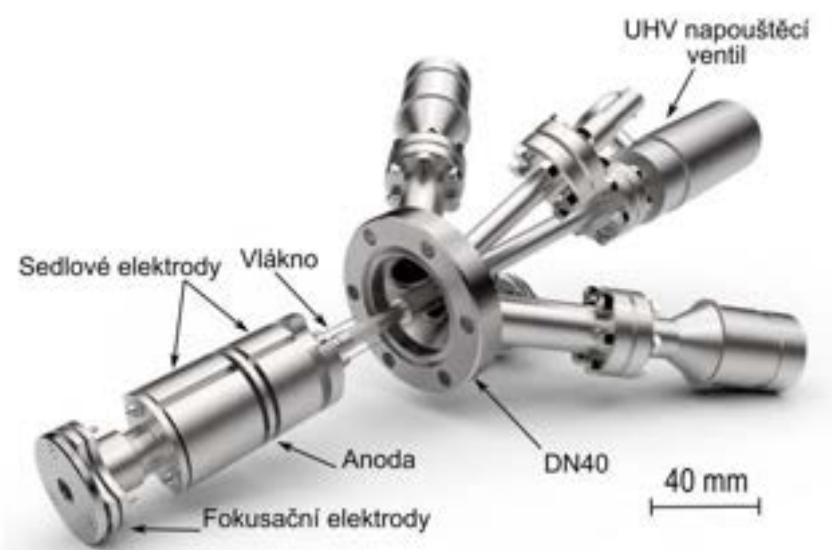

Obrázek 24: 3D model sedlového iontového zdroje s fokusační optikou.

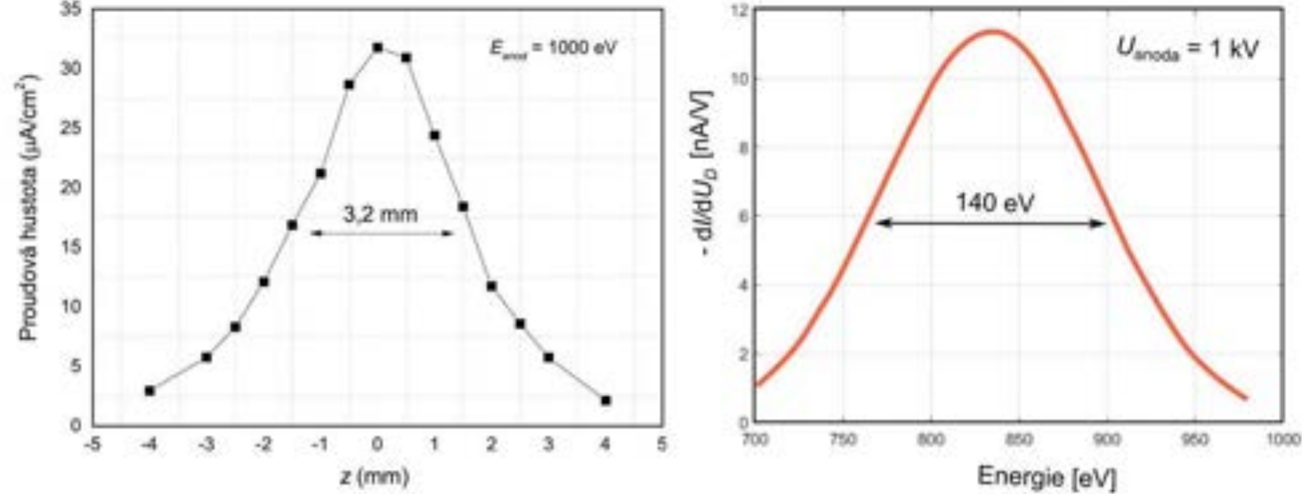

Obrázek 252: Parametry iontového sedlového zdroje pro nastavené napětí na anodě 1 000 V: a) profil intenzity a b) rozložení energií iontů ve svazku argonu (měřeno Faradayovou sondou).

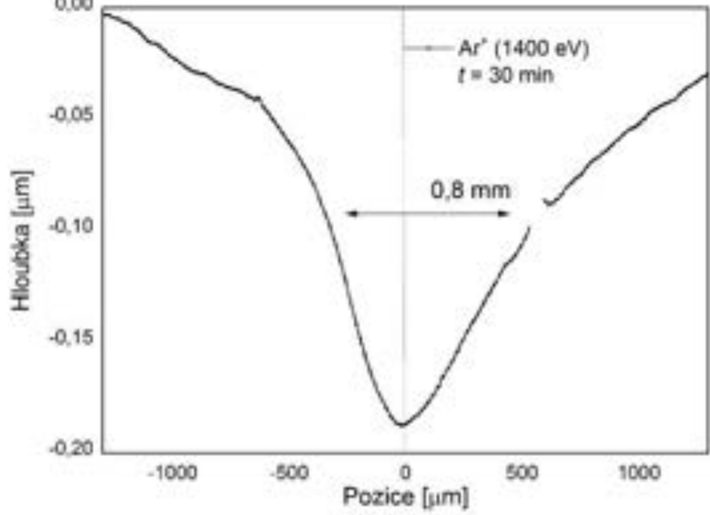

Obrázek 26: Profil vytvořeného kráteru po 30 minutovém odprašování vrstvy SiO_2 ionty Ar^+ o nastavené energii 1 400 eV měřeny pomocí profilometru Bruker Dektak XT.

7. Závěr

V práci byly přehledně popsány základní principy tvorby ultratenkých a nanostrukturních materiálů v podmínkách vysokého a ultravysokého vakua a z nich vyplývající nároky na konstrukci zařízení určených pro jejich tvorbu. Uváděná zařízení byla vybrána s ohledem na jejich konstrukci a užívání na Ústavu fyzikálního inženýrství FSI VUT v Brně. V části popisující depozici tenkých vrstev ve vakuu pomocí chemických metod jsou popsány základní principy jejich tvorby. Jako příklad je uvedena konstrukce a realizace jednoduchého vysokoteplotního CVD reaktoru určeného pro růst grafenu na unikátní ultrahladké měděné folii. K tématu jsou přiřazeny dva publikované vědecké články, které doplňují popis vědeckého přínosu navrženého reaktoru. První uvedený článek je věnován unikátní metodě přípravy grafenových vrstev a jejich charakterizaci. Autor navrhl konstrukci reaktoru a podílel se spolu se svými studenty na realizaci růstu grafenu. Navíc je spoluautorem metody přípravy ultra-hladké měděné folie. Druhá publikace doplňuje význam užívání grafenových vrstev v oblasti senzorů vlhkosti a studia jeho základních fyzikálních principů měření. Autor realizoval UHV komoru pro měření transportních vlastností a provedl měření interakce grafenu s adsorbovanými molekulami vody.

Dále je v práci popsána příprava ultratenkých a nanostrukturních materiálů v podmínkách ultravysokého vakua využívající fyzikální principy PVD. Teoreticky jsou popsány základní vlastnosti a principy tvorby atomárních svazků užívaných v efuzních atomárních zdrojích. Atomární (molekulární) zdroje jsou zde rozděleny dle teploty potřebné k přípravě atomárních svazků v podmínkách UHV s ohledem na základy jejich konstrukce. Zprvu je popsána problematika konstrukce nízkoteplotního zdroje atomů do 400 °C pro materiály s nízkou teplotou nasycených par. Jako příklad jsou uvedeny dvě vyvinuté unikátní konstrukce atomárního zdroje pro depozici organických polovodičů a depozici Zn.

Následně pokračuje popis konstrukce moderních atomárních zdrojů s pracovní teplotou do 1 000 °C, které jsou reprezentovány dvěma návrhy lišícími se zejména konstrukcí ohřevu. První zde uvedený atomární zdroj je žhaven vlivem termální radiace pocházející z proudem ohřívaného odporového tantalového drátu navinutého kolem kalíšku. Další alternativní typ ohřevu je zastoupený zdrojem atomů využívajícím dopadu urychlených termoemisních elektronů na kalíšek pocházejících z wolframové katody. Úspěšná aplikace uváděných zdrojů je demonstrována na studiu elektrických transportních vlastností grafenu ovlivněných atomy Ga, kde autor tato měření navrhl a realizoval.

Ve třetí skupině jsou uvedeny vysokoteplotní atomární zdroje neboli atomární zdroje žáruvzdorných materiálů operujících při teplotách zdroje do 2 000 °C. Problematika konstrukce těchto typů zdrojů je demonstrována na příkladu navrženého sublimačního zdroje atomů uhlíku. Atomy uhlíku jsou sublimovány z HOPG vlákna žhaveného průchodem elektrického proudu. Druhá alternativní konstrukce ohřevu vysokoteplotního zdroje atomů využívá dopadu urychlených termoemisních elektronů fokusovaných do středu HOPG terče, čímž dochází k jeho lokálnímu ohřevu.

Do speciální čtvrté skupiny uváděných zdrojů atomů jsou zařazeny disociační zdroje užívající k disociaci molekul pyrolýzu, nebo vysokofrekvenční plazmatický výboj. V práci je popsána konstrukce vysokoteplotního disociačního zdroje atomů vodíku, kdy vodíkové molekuly H_2 jsou disociovány uvnitř wolframové kapiláry žhavené na teplotu 2 000 °C. Na příkladu vysoko-frekvenčního zdroje atomů vodíku, kyslíku a dusíku je demonstrována úspěšnost unikátní konstrukce disociačních atomárních zdrojů z plazmatu.

Do samostatné skupiny hybridních zdrojů užívaných při PVD depozicích je zařazen iontově-atomární zdroj navržený pro studium růstu GaN. Jedná se o unikátní autorem tohoto textu patentovanou konstrukci kombinující efuzní zdroj atomů Ga a elektronově srážkový zdroj iontů dusíku. Detaily konstrukce byly zveřejněny ve dvou uvedených publikacích, kde autor provedl konstrukční návrh zdroje a realizoval související experimenty vedoucí k nízkoteplotní syntéze polovodičového materiálu GaN.

Užitím kombinace iontových a atomárních svazků je umožněno realizovat růst ultratenkých GaN vrstev a nanostruktur za teploty $T < 200$ °C. Využívání iontově atomárního zdroje je demonstrováno v přiložené publikaci na růstu GaN ultratenkých vrstev a selektivně připravených nanokrystalů GaN, které vykazují silnou fotoluminiscenci. Autor prováděl experimenty s růstem Ga a GaN na křemíkových površích a studoval jejich optické vlastnosti. Toto podrobné porozumění růstovému chování Ga a GaN vede k dalším možným aplikacím zmíněných materiálů (senzory, elektronové trysky, …).

V poslední části práce je diskutována konstrukce iontových zdrojů preferenčně užívaných k modifikaci povrchů (vznik pórů, dopování,…) nebo k jejich odprašování. V této části je jako příklad uvedena konstrukce sedlového iontového zdroje se žhavenou katodou. Návrh byl realizován zejména pro aplikace v prostředí elektronových mikroskopů. Autor se podílel na celkovém vývoji iontového zdroje, navrhl užití žhavené katody a realizoval její uložení. Navíc provedl testování a jeho následnou optimalizaci, až bylo dosaženo konkurenceschopných parametrů.

Pro přehlednost uvádím i souhrnnou přehledovou tabulku všech zde popsaných zařízení určených pro růst ultratenkých vrstev a nanostrukturních materiálů v podmínkách vakua. V souvislosti s těmito zařízeními bylo pod autorovým vedením provedeno 49 závěrečných prací.

V budoucnu se autor chce nadále věnovat ve své vědecké i pedagogické činnosti oblasti vakuových technologií a vývoji specializovaných vakuových zařízeních pro tvorbu nanostruktur. Bude dále rozvíjet aplikační potenciál představených zařízeních s ohledem na jejich využití v praxi. Jako příklad lze uvést syntézu GaN nanokrystalů jako součást polovodičových svítivých diod nebo autoemisních elektronových trysek. V současné době se také jeví jako velmi perspektivní kombinace struktur GaN a grafenu nacházející uplatnění pro vývoj UV senzorů.

Název zařízení	Metoda	Materiál	Provozní teplota, parametry	Strana
Vysokoteplotní reaktor CVD	CVD	Grafen	1000 °C	obr. 3
Efuzní zdroj pro napařování organických polovodičů	PVD	PTCDI-C8	< 300 °C	obr. 10
Efuzní zdroj atomů zinku	PVD	Zn	< 500 °C	obr. 11
Zdroj atomů s radiačním ohřevem	PVD	Au, Ag, Ge, ...	300 °C až 950 °C	obr. 12
Zdroj atomů s ohřevem pomocí dopadu elektronů	PVD	Ga, Ge, Ag, Au, Fe, CaF	300 °C až 950 °C	obr. 13
Sublimační zdroj svazků atomů uhlíku	PVD	C	2300 °C	obr. 14
Zdroj atomů uhlíku s ohřevem pomoci fokusovaného elektronového svazku	PVD	C	2300 °C	obr. 15
Disociační termální zdroj atomů	PVD	H	1800 °C	obr. 17
Vysokofrekvenční disociační zdroj	PVD	H, O, N	VF plasma (13,56 MHz, 500 W)	obr. 18
Iontově-atomární zdroj	PVD	Ga, GaN, N_2^+	950 °C, 30 - 200 eV	obr. 20
Elektron-srážkový iontový zdroj se sedlovým polem	PVD	Ar^+,N_2^+	300-2000 eV	obr. 24

Tabulka: Přehledová tabulka unikátních zařízení zhotovených pro růst nanostrukturních materiálů v podmínkách vakua.

Literatura:

[1] GEIM, A. K. a K. S. NOVOSELOV. The rise of graphene. *Nature Materials*. 2007, **6**, 183–191.

[2] ROSSI, Alessandro, Tuomo TANTTU, Kuan Yen TAN, Ilkka IISAKKA, Ruichen ZHAO, Kok Wai CHAN, Giuseppe C TETTAMANZI, Sven ROGGE, Andrew S DZURAK a Mikko MO. An Accurate Single-Electron Pump Based on a Highly Tunable Silicon Quantum Dot. *Nano Letters*. 2014, **14**, 3405–3411.

[3] BOLES, Michael A, Daishun LING, Taeghwan HYEON a Dmitri V TALAPIN. The surface science of nanocrystals. *Nature Materials* [online]. 2016, **15**, 141–154. Dostupné z: doi:10.1038/nmat4578

[4] BAHAMONDE, Janire Peña, Hang N NGUYEN, Sofia K FANOURAKIS a Debora F RODRIGUES. Recent advances in graphene ‑ based biosensor technology with applications in life sciences. *Journal of Nanobiotechnology* [online]. 2018, **16**(75), 1–18. ISSN 1477-3155. Dostupné z: doi:10.1186/s12951-018-0400-z

[5] CHHOWALLA, Manish, Debdeep JENA a Hua ZHANG. Two-dimensional semiconductors for transistors. *NATURE REVIEWS | MATERIALS* [online]. 2016, **1**(16052), 1–15. Dostupné z: doi:10.1038/natrevmats.2016.52

[6] LI, Xinming, Hongwei ZHU, Kunlin WANG, Anyuan CAO, Jinquan WEI, Chunyan LI, Yi JIA, Zhen LI, Xiao LI a Dehai WU. Graphene-on-silicon Schottky junction solar cells. *Advanced materials (Deerfield Beach, Fla.)* [online]. 2010, **22**(25), 2743–8 [vid. 2013-10-22]. ISSN 1521-4095. Dostupné z: doi:10.1002/adma.200904383

[7] WANG, Faxing, Xiongwei WU, Chunyang LI, Yusong ZHU, Lijun FU, Yuping WU a Xiang LIU. Environmental Science post-lithium ion batteries. *Energy Environ. Sci.* [online]. 2016, **9**, 3570–3611. Dostupné z: doi:10.1039/c6ee02070d

[8] MICHAEL M. THACKERAY, CHRISTOPHER WOLVERTON, Eric D. Isaacs. Environmental Science going beyond , lithium-ion batteries. *Energy Environ. Sci.* [online]. 2012, **5**, 7854–7863. Dostupné z: doi:10.1039/c2ee21892e

[9] XU, Dikai, Xuegong YU, Lijian ZUO a Deren YANG. Interface engineering and efficiency improvement of monolayer graphene–silicon solar cells by inserting an ultra-thin LiF interlayer. *RSC Advances* [online]. 2015, **5**, 46480–46484. Dostupné z: doi:10.1039/c5ra05619e

[10] HAMMEROVÁ, Veronika. *Depozice Ga a GaN nanostruktur na grafenový substrát*. Brno, 2017. Diplomová práce. VUT v Brně, FSI, ÚFI. Vedoucí práce: Ing. MACH Jindřich PhD.

[11] SEVERA, Jiří. *Příprava grafenových membrán vhodných pro depozici Ga*. Brno, 2019. Bakalářská práce. VUT v Brně, FSI, ÚFI. Vedoucí práce: Ing. MACH Jindřich PhD.

[12] KURFÜRSTOVÁ, Markéta. *Vodíkem modifikované grafenové struktury pro polem řízené tranzistory*. Brno, 2016. Diplomová práce. VUT v Brně, FSI, ÚFI. Vedoucí práce: Ing. MACH Jindřich PhD.

[13] MOHELSKÝ, Ivan. *GaN modifikované Schottkyho solární články s rozhraním grafen/Si*. Brno, 2018. Bakalářská práce. VUT v Brně, FSI, ÚFI. Vedoucí práce: Ing. MACH Jindřich PhD.

[14] PROCHÁZKA, Pavel. *Příprava grafenu metodou CVD*. Brno, 2012. Diplomová práce. VUT v Brně, FSI, ÚFI. Vedoucí práce: Ing. MACH Jindřich PhD.

[15] ZAHRADNÍČEK, Radim. *Schottkyho solární články na rozhraní grafen/křemík.* Brno, 2014. Diplomová práce. VUT v Brně, FSI, ÚFI. Vedoucí práce: Ing. MACH Jindřich PhD.

[16] HLAVIČKA, Ivo. *Ga modifikované Schottkyho solární články s rozhraním grafen/Si*. Brno, 2015. Bakalářská práce. VUT v Brně, FSI, ÚFI. Vedoucí práce: Ing. MACH Jindřich PhD.

[17] KURFÜRSTOVÁ, Markéta. *Grafenové struktury vhodné pro polem řízené tranzistory*. Brno, 2014. Bakalářská práce. VUT v Brně, FSI, ÚFI, BRNO. Vedoucí práce: Ing. MACH Jindřich

PhD.
[18] HAMMEROVÁ, Veronika. *Studium rozhraní grafén/křemík užitím metody EBIC*. Brno, 2014. Bakalářská práce. VUT v Brně, FSI, ÚFI. Vedoucí práce: Ing. MACH Jindřich PhD.
[19] HULVA, J. *Preparation and characterisation of electrical properties of graphene CVD single crystals*. Brno, 2014. Diplomová práce. VUT v Brně, FSI, ÚFI. Vedoucí práce: Ing. MACH Jindřich PhD.
[20] BONACCORSO, F, Z SUN, T HASAN a A C FERRARI. Graphene photonics and optoelectronics. *Nature Photonics* [online]. 2010, **4**, 611–622. Dostupné z: doi:10.1038/nphoton.2010.186
[21] LOSURDO, Maria, Maria Michela GIANGREGORIO, Pio CAPEZZUTO a Giovanni BRUNO. Graphene CVD growth on copper and nickel : role of hydrogen in kinetics and structure [online]. 2011, (i), 20836–20843. Dostupné z: doi:10.1039/c1cp22347j
[22] LIU, Nan, Lei FU, Boya DAI, Kai YAN, Xun LIU, Ruiqi ZHAO, Yanfeng ZHANG a Zhongfan LIU. Wafer-Size Graphene from Non-Noble Metals [online]. 2011, 297–303. Dostupné z: doi:10.1021/nl103962a
[23] LEE, Youngbin, Sukang BAE, Houk JANG, Sukjae JANG, Shou-en ZHU, Sung Hyun SIM, Young Il SONG, Byung Hee HONG a Jong-hyun AHN. Wafer-Scale Synthesis and Transfer of Graphene Films [online]. 2010, 490–493. Dostupné z: doi:10.1021/nl903272n
[24] REINA, Alfonso, Xiaoting JIA, John HO, Daniel NEZICH, Hyungbin SON, Vladimir BULOVIC, Mildred S DRESSELHAUS a Jing KONG. Large Area , Few-Layer Graphene Films on Arbitrary Substrates by Chemical Vapor Deposition 2009. 2009, 1–6.
[25] WANG, Jianwei, Budhi SINGH, Sunglyul MAENG, Han-Ik JOH a Gil-Ho KIM. Assembly of thermally reduced graphene oxide nanostructures by alternating current dielectrophoresis as hydrogen-gas sensors. *Applied Physics Letters* [online]. 2013, **103**(8), 083112 [vid. 2013-12-13]. ISSN 00036951. Dostupné z: doi:10.1063/1.4819378
[26] MILTON OHRING. *Materials Science of Thin Films* [online]. United Kingdom: Elsevier, 1992. ISBN 9780125249751. Dostupné z: doi:10.1016/B978-0-12-524975-1.X5000-9
[27] BELLO, Igor. *Vacuum and Ultravacuum* [online]. United Kingdom: CRC Press, 2017. ISBN 9781315155364. Dostupné z: doi:10.1201/9781315155364
[28] FLATAU, Pioter J, Robert L. WALKO a William R. COTTON. Polynomial Fits to Saturation Vapor Pressure. *J. Appl. Meteorol.* 1992, **31(12)**, 1507–1513.
[29] RASMUSSEN, L. A. On the Approximation of Saturation Vapor Pressure. *J. Appl. Meteorol.* 1978, **17**, 1564–1565.
[30] VÁLYI, László. *Atom and Ion Sources*. 1977. ISBN 9780471994633.
[31] MA, Y., B. Y. H. LIU, H. S. LEE, K. MAUERSBERGER a J. MORTON. Focusing glass capillary array molecular beam inlet for a high sensitivity mass spectrometer system. *Journal of Vacuum Science & Technology A: Vacuum, Surfaces, and Films* [online]. 1996, **14**(4), 2414–2417. ISSN 0734-2101. Dostupné z: doi:10.1116/1.580029
[32] MANIŠ, J. *Studium molekulárních svazků organických materiálů*. Brno, 2014. Bakalářská práce. VUT v Brně, FSI, ÚFI. Vedoucí práce: Ing. MACH Jindřich PhD.
[33] HORÁK, Stanislav. *Návrh efuzní cely pro depozici ultratenkých vrstev Sn a Zn*. Brno, 2016. Bakalářská práce. VUT v Brně, FSI, ÚFI. Vedoucí práce: Ing. MACH Jindřich PhD.
[34] KOLÍBAL, Miroslav, Tomáš VYSTAVĚL, Libor NOVÁK, Jindřich MACH a Tomáš ŠIKOLA. In-situ observation of 〈 110 〉 oriented Ge nanowire growth and associated collector droplet behavior. *Applied Physics Letters* [online]. 2012, **143113**(October 2011), 1–4. Dostupné z: doi:10.1063/1.3647774
[35] KOLÍBAL, Miroslav, Radek KALOUSEK, Tomáš VYSTAVĚL, Libor NOVÁK a Tomáš ŠIKOLA. Controlled faceting in 〈 110 〉 germanium nanowire growth by switching between growth. 2012, **203102**.
[36] KOLÍBAL, Miroslav, Tomáš PEJCHAL, Tomáš VYSTAVĚL a Tomáš ŠIKOLA. The

Synergic E ff ect of Atomic Hydrogen Adsorption and Catalyst Spreading on Ge Nanowire Growth Orientation and Kinking. *Nano Letters* [online]. 2016, **16**, 48804886. Dostupné z: doi:10.1021/acs.nanolett.6b01352

[37] PRŮŠA, Stanislav, Pavel BÁBÍK, Jindřich MACH, Tomáš STRAPKO, Tomáš ŠIKOLA a Hidde H. BRONGERSMA. Calcium and fluorine signals in HS-LEIS for CaF 2 (111) and powder — Quantification of atomic surface concentrations using LiF (001), Ca , and Cu references Calcium and fluorine signals in HS-LEIS for CaF 2 (111) and powder — Quantification of atomi. *Surf. Sci. Spectra* [online]. 2020, **27**, 024201–13. Dostupné z: doi:10.1116/6.0000325

[38] BARTOSÍK, Miroslav, Miroslav KOLÍBAL, Jan CECHAL, Jindrich MACH a Tomás SIKOLA. Selective growth of metallic nanostructures on surfaces patterned by AFM local anodic oxidation. *Journal of nanoscience and nanotechnology* [online]. 2009, **9**(10), 5887–90. ISSN 1533-4880. Dostupné z: doi:10.1166/jnn.2009.1251

[39] PIASTEK, Jakub. *Příprava grafenových vrstev pokrytých Ga atomy a charakterizace jejich elektrických vlastností*. Brno, 2015. Diplomová práce. VUT v Brně, FSI, ÚFI. Vedoucí práce: Ing. MACH Jindřich PhD.

[40] ROSS, K. J. a B. SONNTAG. High temperature metal atom beam sources. *Review of Scientific Instruments* [online]. 1995, **66**(9), 4409–4433. ISSN 00346748. Dostupné z: doi:10.1063/1.1145337

[41] CHEN, S., L. L. FAN, J. WANG, Y. PAN, F. H. CHEN, P. S. XU, C. W. ZOU a Z. Y. WU. The optimization of a self-focusing e-beam evaporator for carbon evaporation and the application for graphene growth. *Surface and Coatings Technology* [online]. 2014, **258**, 1196–1201. ISSN 02578972. Dostupné z: doi:10.1016/j.surfcoat.2014.07.009

[42] HORÁČEK, Matěj. *Návrh atomárního zdroje uhlíku pro přípravu grafenových vrstev v podmínkách UHV*. Brno, 2013. Bakalářská práce. VUT v Brně, FSI, ÚFI. Vedoucí práce: Ing. MACH Jindřich PhD.

[43] ČALKOVSKÝ, Martin. *Příprava grafenových vrstev metodou MBE*. Brno, 2015. Bakalářská práce. VUT v Brně, FSI, ÚFI. Vedoucí práce: Ing. MACH Jindřich PhD.

[44] ČALKOVSKÝ, Vojtěch. *Návrh zdroje atomů uhlíku pro přípravu grafenových vrstev v UHV*. Brno, 2016. Bakalářská práce. VUT v Brně, FSI, ÚFI. Vedoucí práce: Ing. MACH Jindřich PhD.

[45] LIŠKA, Petr. *Optimalizace zdroje atomů uhlíku pro růst grafenových vrstev metodou MBE*. 2019.

[46] SHEBARO, Lina, Sameer R BHALOTRA a Dudley HERSCHBACH. Molecular Beam Chemistry : Formation of Benzene and Other Higher Hydrocarbons from Small Alkanes and Alkenes in a Catalytic Supersonic Nozzle. 1997, **5639**(97), 6775–6780.

[47] FISSEL, A., H. J. OSTEN a E. BUGIEL. Towards understanding epitaxial growth of alternative high-K dielectrics on Si(001): Application to praseodymium oxide. *Journal of Vacuum Science & Technology B: Microelectronics and Nanometer Structures* [online]. 2003, **21**(4), 1765. ISSN 0734211X. Dostupné z: doi:10.1116/1.1589516

[48] SUGAYA, Takeyoshi a Mitsuo KAWABE. Low-temperature cleaning of gaas substrate by atomic hydrogen irradiation. *Japanese Journal of Applied Physics* [online]. 1991, **30**(3A), 402–404. ISSN 13474065. Dostupné z: doi:10.1143/JJAP.30.L402

[49] MELICHÁREK, Václav. *Optimalizace termálního disociačního zdroje atomů vodíku pro SEM*. Brno, 2018. Bakalářská práce. VUT v Brně, FSI, ÚFI. Vedoucí práce: Ing. MACH Jindřich PhD.

[50] KERN, Michal. *Optimalizace vysokofrekvenčního atomárního disociačního zdroje pro depozici GaN*. Brno, 2013. Bakalářská práce. VUT v Brně, FSI, ÚFI. Vedoucí práce: Ing. MACH Jindřich PhD.

[51] MARES, Petr. *Selektivní růst GaN na modifikovaný substrát metodou FIB*. Brno, 2012.

Bakalářská práce. VUT v Brně, FSI, ÚFI. Vedoucí práce: Ing. MACH Jindřich PhD.
[52] MARES, Petr. *Deposition of Ga and GaN nanostructures on silicon and graphene substrates*. Brno, 2014. Diplomová práce. VUT v Brně, FSI, ÚFI. Vedoucí práce: Ing. MACH Jindřich PhD.
[53] DAMKOVA, J. *Sekvenční růst GaN nanokrystalů na substrátu SiO2 modifikovaný metodou FIB*. Brno, 2013. Bakalářská práce. VUT v Brně, FSI, ÚFI. Vedoucí práce: Ing. MACH Jindřich PhD.
[54] BÁRDY, Stanislav. *Deposition of Ga and GaN Nanostructures on Graphene Substrate Treated by Atomic Hydrogen*. Brno, 2016. Diplomová práce. VUT v Brně, FSI, ÚFI. Vedoucí práce: Ing. MACH Jindřich PhD.
[55] ČALKOVSKÝ, Martin. *The deposition of Ga and GaN nanostructures with metal core*. Brno, 2017. Diplomová práce. VUT v Brně, FSI, ÚFI. Vedoucí práce: Ing. MACH Jindřich PhD.
[56] LENCOVÁ, Bohumila a Jakub ZLÁMAL. A new program for the design of electron microscopes. *Physics Procedia* [online]. 2008, **1**(1), 315–324. ISSN 1875-3892. Dostupné z: doi:10.1016/j.phpro.2008.07.111